8-8-2014

POLYMER NANO-DIELECTRICS FOR HIGH DENSITY ENERGY STORAGE

Sayful Islam Md
University of South Carolina - Columbia

POLYMER NANO-DIELECTRICS FOR HIGH DENSITY ENERGY STORAGE

by

Md. Sayful Islam

Bachelor of Science
Bangladesh University of Engineering and Technology, 2008

Submitted in Partial Fulfillment of the Requirements

For the Degree of Doctor of Philosophy in

Chemical Engineering

College of Engineering and Computing

University of South Carolina

2014

Accepted by:

Harry J. Ploehn, Major Professor

James A. Ritter, Committee Member

Chuanbing Tang, Committee Member

Jason Hattrick-Simpers, Committee Member

John W. Weidner, Committee Member

Lacy Ford, Vice Provost and Dean of Graduate Studies

DEDICATION

To my family. In particular, to my elder brothers who inspired me in science and technology since my childhood.

ACKNOWLEDGEMENTS

I am forever indebted to my adviser, Dr. Harry J. Ploehn for his contributions to my personal and academic developments as well as many achievements during my graduate career. His insightful thoughts and friendly discussions on my research made the working environment so exquisite to solve many challenging problem without pressure. I will always remember his outstanding teaching skills and the excellent mentoring provided to me.

I would like to thank my Ph.D. committee members Prof. James A. Ritter, Prof. Chuanbing Tang, and Prof. Jason Hattrick-Simpers for their advice and discussions to develop me as a critical thinker. I am grateful to our collaborators, Dr. Chuanbing Tang for giving me the opportunity to explore all-polymer dielectric materials, and Dr. Hans Conrad zur Loye for facilitating my work on organic/inorganic dielectric materials. I appreciate the polymer synthesis efforts by Dr. Yali Qiao and Dr. Christopher Hardy, and inorganic filler synthesis by Dr. W. Michael Chance.

I am extremely thankful to my colleague Dr. Shiva Balasubramanian for helping me in several experiments on dielectric material research at the beginning of my graduate studies. I am thankful to Ploehn research group members, Dr. Xiaoming Chen, Shailesh Shori, and Yating Mao for their help and valuable discussions.

I am also grateful to the research staff, and my colleagues at Horizon-1. I will always remember the jolly minded people around Horizon-1 especially Warren, Toney, Mike, Anand, Perry, Mitra and others. I am thankful to the Chemical Engineering Departmental administrative and research staff for their help during my graduate studies.

It is my pleasure to appreciate Dr. Shubhra Jyoti Bhadra, Dr. Iftekhar Hossain, Dr. Md. Safaruddin Opu, Dr. Mayukhee Das, Shariar Salim. Jadid Samad, Dr. Shamaita Shithi, and Sabih Uddin Omor-for course work discussions during my graduate studies, and Dr. Jahid Ferdous, Dr. Fazzle Rabbi, and Dr. Md. Rassel Raihan-for COMSOL modeling help. I also thank Rishad Hossain, Dr. Nazmul Alam, Md. Moinul Islam, and Chamok Hasan for helping me in rationalizing circuit elements using MATLAB. I appreciate all my friends and colleagues for their support to make an enjoyable graduate life for me.

Finally, I am grateful to my loving family who has instilled eagerness in science studies and maintain an unwavering support to me since my childhood. I recognized my parent's vision to excel in education. I could remember how hard my elder brothers, Iqbal Hossain, Md. Monirul Islam tried to teach me math and science. I appreciate every bit of extra care from my siblings Riazur Rahman, Iman Hasan, and my only sister Neelima Rahman. I deeply appreciate all the efforts you all put forward to make me successful.

ABSTRACT

Military and commercial users require next-generation polymer dielectric materials for pulse power and power conditioning applications with rise times less than 1 ms and AC power at frequencies ranging from kHz to MHz. These power density and rate capability requirements necessitate the use of dielectric capacitors that store energy via polarization of electrons in molecular scale dipoles. Multiphase polymer composites and all-polymer dielectrics could be new kinds of materials to meet this acute need for capacitors with compact size and high rate capability.

The polymer nanocomposite (PNC) approach to achieve high energy density employed a "colossal" dielectric constant material, calcium copper titanate, $CaCu_3Ti_4O_{12}$ (CCTO) as filler, and high dielectric breakdown strength and low loss polycarbonate (PC) as the polymer matrix. This work systematically analyzes CCTO/PC composites, starting with low field dielectric properties (dielectric constant, dielectric loss) and extending to (for the first time) high field D-E polarization behavior. Our findings suggest that CCTO/PC composites are promising for applications requiring high dielectric constant at low field strength, but not as dielectrics for high density, pulse power energy storage.

"Multiphase all-polymer dielectric" materials is a novel approach to meet the high rate capability demand in dielectric capacitors. Our chemistry collaborators

synthesized variety of new homopolymers and copolymers that are hypothesized to form phase-separated, interfacially-dominated structures capable of storing energy through electronic conduction and interfacial polarization. The polymer architecture features a combination of conducting and insulating segments hypothesized to form phase-segregated domains with high electronic conductivity, surrounded by insulating domains that prevent percolation and inter-domain conduction. It is hoped that this method will circumvent shortcomings in existing polymeric dielectric materials for high density energy storage applications. The main result is a terthiophene-containing (PTTEMA) polymer that can store energy density up to 1.54 J/cm^3, higher than commercially available biaxially oriented polypropylene (BOPP) at 200 MV/m applied electric field. In addition, different approaches, such as PTTEMA grafted onto barium titanate/PTTEMA composites and PTTEMA/PS polymer blends, have been employed to optimize PTTEMA polymers to make them suitable for pulse power applications. Finally, COMSOL^{TM} simulations were used to understand how polymer composites microstructure affects material polarization.

TABLE OF CONTENTS

LIST OF TABLES

LIST OF FIGURES

LIST OF SYMBOLS

C	Capacitance, F
C_o	Vacuum capacitance, F
q	Electric charge, C
V	Applied voltage, V
d	Dielectric film thickness
D	Electric displacement, $\mu C/cm^2$
P	Polarization, $\mu C/cm^2$
E	Applied electric field, V/m
E_{bd}	Dielectric breakdown strength, V/μm
Z	Impedance, ohms
$\hat{W}$	Stored energy density, J/cm^3
ε_o	Vacuum permittivity, 8.854×10^{-12} F/m
ε^*	Complex relative permittivity
ε_r (ε_r')	Relative permittivity of dielectric (real part of complex permittivity), dimensionless
ε_r'	Imaginary part of complex relative permittivity, dimensionless
tanδ	Dielectric loss tangent
$h\omega_p$	Plasmon energy, eV

Eg	Band gap, eV
t	Crystal size
λ	X-ray wave length, A°
B	Full width at half Maximum of the main diffraction peaks (obtained from JADE software)

List of Abbreviations

PNC.....Polymer nano-composite

PC ..... Polycarbonate

PS..... Polystyrene

BT ..... Barium titanate, $BaTiO_3$

CCTO..... Calcium copper titanate, $CaCu_3Ti_4O_{12}$

sgCCTO .....Calcium copper titanate prepared from sol-gel method

ssCCTO.....Calcium copper titanate prepared from solid state method

CDC..... Colossal dielectric constant

PEG ..... Polyethylene glycol

OANI .....Oligoaniline containing polymer

PAMPSA .....Poly-(2-acrylamido-2-methyl-1-propanesulfonic acid)

PMA..... Poly (methylacrylate)

PTTEMA.....Methacrylate polymers containing terthiophene side groups

RAFT ..... Reversible addition fragmentation transfer

CHAPTER 1

INTRODUCTION

1.1 MOTIVATION

High performance dielectric materials are needed for both commercial and military purposes [1-4]. All applications need energy storage devices with high energy and power density, low dissipation, and very high rate capability ("pulse power"). It is expected that power conditioning systems for the Navy's Integrated Electric Power System will require power pulses with rise times less than 1 ms and AC power at frequency ranging from kHz to MHz. The power density and rate capabilities necessitate the use of dielectric capacitors that store energy through various polarization mechanisms [5]. The best practical dielectric capacitor material available today, based on metalized, biaxially-oriented polypropylene (BOPP), has low volumetric energy density. It is about 1.7 J/ cm^3 (under packaged condition) with a further 20% increase envisioned upon improve package design [6]. This magnitude of energy density, although promising, does not solve the volume occupancy issue of large electric systems for pulse power and power conditioning operations. Thus, volumetric energy density

must be increased for future shipboard power systems as well as for commercial power electronics.

The Navy has established benchmarks for the next generation of dielectric capacitor materials including intrinsic energy density more than 20 J/cm^3, dielectric loss less than 0.1%, and operation stability up to 150°C. All of these requirements must be achieved in polymer materials that can be processed easily, at low cost, to manufacture reliable large capacitors (C > 1F). Fundamental considerations and practical limitations make it difficult to satisfy all these requirements simultaneously. Thus synthesizing polymer-based dielectric materials with stored energy density more than an order of magnitude larger than today's materials is a very challenging problem.

1.2 BACKGROUND

High energy density in a material can be achieved if it possesses a high number density of polarizable domains, which will create large induce dipole moment (μ_{ind}) under applied electric field. The polarization of a dielectric P is given by

$$P=N\,\mu_{ind}=N\alpha E=NE\,(\alpha_0+\mu^2/3kT) \qquad (1.1)$$

and represents the average dipole moment per volume. The electric displacement D is related to polarization density P by

$$D=\varepsilon_0 E+P \qquad (1.2)$$

Consider a parallel plate capacitor with electrode area A, and distance between electrodes d. Under applied voltage V (Figure 1.1a), an electric field will be established and charge q will accumulate on the electrodes. Substituting these values of charge q and applied electric field E in

$$C = \frac{q}{V} = \frac{q}{Ed} \qquad (1.3)$$

gives the capacitance C of the material. Now, suppose we insert insulating materials between the electrodes with dielectric constant ε_r (Figure 1.1b). Under applied voltage V (Figure 1.1c), an electric field will be established and the molecules of dielectric material will be polarized, creating many dipoles. These dipoles induce an electric field opposite to the applied field and, the net electric field will be reduced (Figure 1.1d). Substituting this reduced electric field E' for the same number of charges q gives a higher capacitance in equation (1.3). The main idea of dielectric capacitor is to create a large number of these dipoles. However, they should not touch each other: inter-dipoles contact creates conduction path ways for dielectric breakdown and dielectric loss.

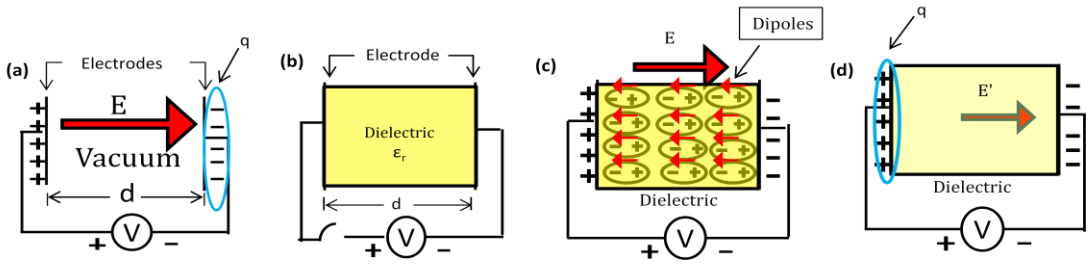

Figure 1.1. Working principle of dielectric capacitor.

This results in volumetric stored energy density given by $\hat{W}$

$$\hat{W} = \frac{W}{Ad} = \frac{1}{Ad}\int Vdq \; = \int EdD \qquad (1.4)$$

where q is the free surface charge related to electric displacement by D=q/A. For the ideal case of a linear dielectric [e.g., biaxially oriented polypropylene (BOPP), polyethylene (PE), polystyrene (PS)] the polarization is

$$P = \varepsilon_0 E (\varepsilon_r - 1) \qquad (1.5)$$

leading to electric displacement

$$D = \varepsilon_0 \varepsilon_r E \qquad (1.6)$$

For linear dielectric materials the polarization and depolarization follow the same linear line , resulting in the same stored and recovered energy density (area ABDA in Figure 1.2) [7]. Substituting D from equation (1.6) into equation (1.4) leads to

$$\hat{W} = \frac{1}{2}\varepsilon_0 \varepsilon_r E^2 \qquad (1.7)$$

Therefore, to increase energy density $\hat{W}$, one may try to maximize both the magnitude of the applied field E (as close as possible to the breakdown field strength E_b) and ε_r.

In practice, most dielectric materials (e.g., polar polymers, polymers with impurity ions, and immiscible polymer blends with poor interfaces) show nonlinear response to an external applied electric field. This nonlinearity is manifested as a

hysteresis loop (area ABCA in Figure 1.2), where the polarization and depolarization curves follow different paths. Consequently, the stored energy density (area ABDA in Figure 1.2) for such dielectric materials, calculated from equation (1.4) [8] is different from the recovered energy density (area CBDC in Figure 1.2). Thus simply maximizing ε_r will not maximize $\hat{W}$. Instead it is necessary to optimize D as function of E to obtain highest stored and recovered energy density.

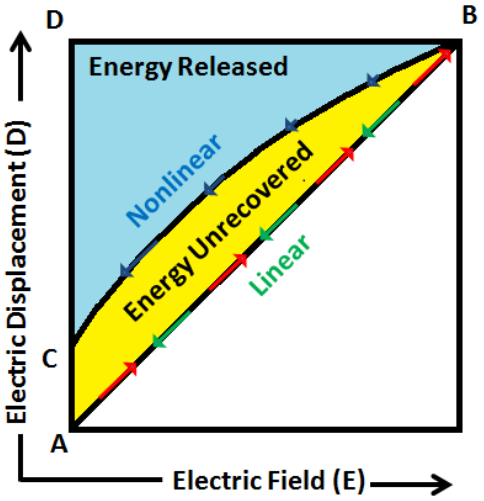

Figure 1.2. Representation of unipolar D–E hysteresis loops under high-field switching for calculation of energy stored, energy released, and (%) energy loss in linear and nonlinear dielectric materials.

1.3 Single Phase Polymer Dielectrics

For bulk polymer, an order-of-magnitude increase in stored energy density ($\hat{W}$) can be possible through a three to four-fold increase in breakdown field strength (E_b). However, most of the polymers used for dielectric capacitors are already optimized. For example, biaxially oriented polypropylene (BOPP) is inexpensive, has high breakdown field strength E_b = 640 MV/m and low loss (tan δ ~ 0.0002 at 1 kHz), but the low

dielectric constant ($\varepsilon_r \sim 2.2$) results in low $\hat{W}$ (<1.2 J/cm^3) [6, 9-11]. On the other hand, poly(vinylidene fluoride) (PVDF) and CoPVDF both have high breakdown strength (500~700 MV/m) like many other organic polymers and high dielectric constant (ε_r = 10-20). Therefore, effort has been made to explore PVDF and CoPVDF polymers for maximizing energy density [1]. Recently, the Penn State group modified the chemical structure of PVDF with chlorinated/fluorinated co-monomer to prepare poly((vinylidene fluoride)-r-(chlorotrifluoroethylene)) (P(VDF-CTFE)), and a terpolymer of vinylidene fluride, chlorotrifluoroethylene (CTFE), and trifluroethylene (TrFE),P(VDF-CTFE-TrFE) [7, 12-15]. These copolymers have high $\hat{W}$ (12-17 J/cm^3) but manifest excessive dielectric loss owing to large remnant polarization [15]. Moreover, the thermal stabilities of these copolymers were not reported. Thus, the lossy nature of PVDF-based copolymers and terpolymers make them less desirable for next generation polymer dielectric materials.

The problem with PVDF-based polymer dielectrics can be explained in terms of the "Moss Rule", a tradeoff between permittivity and band gap E_g [16, 17] for all homogenous and bulk materials:

$$\varepsilon = \varepsilon_0 \varepsilon_r = 1 + (\frac{\hbar\omega p}{E_g})^2 \qquad (1.8)$$

where the plasmon energy is $\hbar\omega_p = \hbar (4\pi ne^2/m)^2$, n is valence electron count, and m and e are electron mass and charge. The number of effective valence electrons for polymers and many semiconductors is roughly constant, and so the plasmon energy is approximately constant (15 eV - 20 eV) [16, 18]. From equation (1.7), it is evident that increasing dielectric constant is possible as the value of the band gap E_g decreases.

Decreasing E_g consequently increases the concentration of thermally generated free charge carriers which gives rise to leakage current and dielectric loss. In addition, it favors avalanche breakdown, thus reducing dielectric strength. These compromises between permittivity, loss and breakdown strength make it very difficult for single-phase polymer dielectrics to achieve high $\hat{W}$ with high E_b and minimal dielectric loss.

1.4 MULTIPHASE POLYMER COMPOSITE DIELECTRICS

Multiphase materials may be able to avoid the limitations of the Moss rule. Polymer composites might achieve high energy density by combining the high relative permittivity ε_r values of inorganic ceramics with the high breakdown field strength values and processability of polymers. In general, the energy density of a biphasic-composite is a weighted sum of the energy density of each constituent. Therefore, to achieve a high energy density in a composite, each constituent must make a significant contribution from toward the total energy density. Polymers currently used as matrices in dielectric nanocomposites (including polyethylene, poly (methylmethacrylate), polycarbonate, polystyrene, epoxy resins, polyimides, polyether ether ketone) usually have dielectric permittivities significantly lower than those of the inorganic filler. Various single- and mixed-metal titanates and zirconates have received much attention, including $BaTiO_3$ (BT) [19-23], $Pb(Zr,Ti)O_3$ (PZT), $CaCu_3Ti_4O_{12}$ (CCTO) [24-35] and numerous others.

Several comprehensive reviews describe previous research on polymer composites for dielectric energy storage [1, 36-39]. Significant gains in composite

effective permittivity ε_{eff} generally require high volume loadings of micron-sized ceramic particles, which reduce the polymer's breakdown field strength and mechanical integrity. Consequently any advantage gain from the high ε_r filler is lost due to the decrease in breakdown field strength, which results poor dielectric performance. Both of these issues involve polymer-filler interfaces, so many research groups are seeking to learn more about polymer-filler interfacial chemistry and structure, and how they are related. Considerable effort has gone into dispersing nano-sized ceramic particles into polymers, which often improves the polymer's E_b value, but not necessarily ε_{eff}. Incompatibility between polymer and filler is the core issue and it poses a significant challenge to developing polymer composite materials for high density dielectric energy storage.

1.5 MULTIPHASE ALL-POLYMER DIELECTRICS

Multiphase polymers, includes polymer blends [40-47] and all-polymer percolative composites [48, 49], represent another approach to creating heterogeneous dielectric materials that avoid the trade off the Moss rule. The main idea of this work is to create blended materials that combine the best properties of each component of the mixture. Phase separated block copolymer dielectrics [50-54] go beyond this concept by taking advantage of the properties of the interfaces in copolymer materials, providing strong mechanical integrity among constituent blocks.

This approach focuses on developing interfacially–dominated block copolymers that will store energy through electronic conduction and interfacial polarization.

Material design utilizes alternative conductive and insulating blocks (Figure 1.3). One block (red) will form nanoscale phase-segregated domains with high electronic conductivity, while other block (blue) will insulate the conducting domains to prevent percolation and inter-domain conduction. Under an applied electric field, electronic conduction will induce "nanodipoles" at interfaces due to space charge accumulation along the phase boundaries. The nanoscale size dipoles will greatly amplify the number density of polarizable domains, resulting in dielectric materials with energy storage dominated by interfacial polarization. It is expected that this method will circumvent the limitations of existing polymer dielectrics to meet requirements for next-generation polymer dielectrics for pulse power and power conditioning applications.

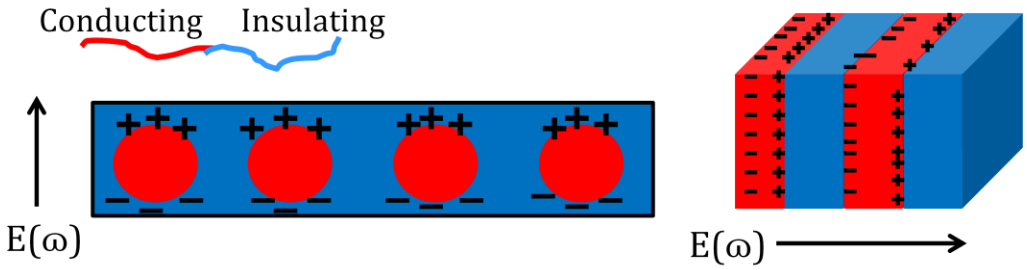

Figure 1.3. Interfacial polarization of micro-and nano-phase separated block copolymers.

1.6 Overview of Dissertation

Given the strong fundamental understanding of polarization mechanisms [5], rational material design based on this understanding offers opportunities to create next generation dielectric materials . This dissertation capitalizes on our fundamental

understanding to develop new, nano-domain high performance dielectric materials based on polymer nanocomposites and multiphase polymers.

Chapter 2 of this dissertation discusses the physical and dielectric characterization techniques used in this research. Chapter 3 discusses our work to develop a polymer nanocomposite dielectric material based on a colossal dielectric constant inorganic material dispersed in a high breakdown strength polymer. Polycarbonate is used as a host polymer matrix because it has low dielectric loss and high breakdown field strength. Calcium copper titanate, $CaCu_3Ti_4O_{12}$ (CCTO), has a giant dielectric constant but low breakdown strength. CCTO was synthesized via a traditional solid-state method as well as a wet chemical sol-gel route by our chemistry collaborators. These different kinds of CCTO were used as fillers to explore the impact of CCTO particle size and interfacial area on dielectric properties. Various kinds of physical characterization of CCTO filler materials as well as composite films are discussed. Finally, Chapter 3 concludes with a discussion of the prospects of CCTO/PC composites as high density energy storage materials.

Chapter 4 presents research on all-polymer dielectric material development approaches, including a novel phase separated block copolymer strategy to achieve high dielectric performance. The chapter introduces the limitations of organic-inorganic (polymer-composites) composites and suggests how multiphase polymers can circumvent the shortcomings of organic-inorganic polymer and the possible challenges to achieving optimal performance. Next, five subsections discuss various approaches to

develop phase separated block copolymers with different material architectures. Section 4.2 discusses our results for oligoaniline-containing supramolecular block copolymer nanodielectric materials and their merits as high performance dielectric materials. Section 4.3 presents simple strategy to develop dielectric materials based on polystyrene end-capped with oligoaniline groups. The synthesis and properties of π-conjugated oligothiophene-containing polymer (polymethacrylate with terthiophene side chains) is introduced in section 4.4. This material has exceptionally small crystalline domains (<2nm) leading to superior dielectric properties. Section 4.5 extends the discussion to other terthiophene-containing polymers, comparing block copolymers and polymer blends of terthiophene-containing polymer with polystyrene to better understand the energy storage mechanism. Section 4.6 employs a bimodal approach to improve dielectric properties of terthiophene-containing polymer to the next level. The bimodal strategy employs terthiophene-containing polymer with different shell thickness grafted onto barium titanate (BT) particles, and disperse those grafted particles in a matrix consisting of terthiophene-containing polymers. Using the same terthiophene containing polymer as a polymer matrix and as a shell on BT particles facilitates uniform dispersion and improved interfacial adhesion between BT particles and the polymer matrix, which in turn provides superior dielectric properties.

Chapter 5 discusses COMSOL^{TM} simulation used to better understand the importance of filler and polymer selection on overall composite performance. Chapter 6 provides possible recommendations for future work to develop materials with superior dielectric properties.

CHAPTER 2

MATERIALS CHARACTERIZATION TECHNIQUES

2.1 PHYSICAL CHARACTERIZATION METHODS

X-ray diffraction patterns were collected by our collaborator Dr. W. Michael Chance and others from Dr. Hans-Conrad zur Loye's research group in the Department of Chemistry and Biochemistry at the University of South Carolina. The instrument is Rigaku D/Max 2100 Powder X-Ray Diffractometer with Cu Kα radiation, λ = 1.5418 A°. The phase purity of final inorganic powder product was checked by PXRD, while wide angle X-ray diffraction (WXRD) for polymers were performed intended to estimate crystalline domain size. The crystalline domain sizes are estimated from Scherrer's formula [55, 56],

$$t = \frac{\lambda}{B\cos\theta} \qquad (2.1)$$

where t is the crystallite size, λ is the X-ray wave length, B is the full width at half Maximum of the main diffraction peaks (obtained from JADE software), and θ is diffraction angle. ^{1}H NMR (300 MHz) spectra were recored by Dr. Yali Qaio on a Varian Mercury 300 spectrometer with tetramethylsilane (TMS) as an internal reference.

^{1}H NMR was primarily used to determine the degree of polymerization (DP) and molecular weight. Additionally, ^{1}H NMR was used to indentify characteristic peaks of grafted polymer on inorganic particles. Differential scanning calorimetry (DSC) from TA Instruments (model Q2000) was used to investigate thermal transitions of the polymers over the temperature range from 0 to 200 ^{o}C at heating and cooling rates of 10 ^{o}C min^{-1} under constant nitrogen flow at a rate of 50 mL/ min. Samples (between 3-10 mg) were added to aluminum hermetic pans and sealed. To ensure accuracy, the data were collected during the second heating and cooling cycle. Thermogravimetric analysis (TGA) was carried out on a TA Instruments Q5000 with heating rate of 10 ^{o}C/ min from RT to 1000 ^{o}C under constant nitrogen flow intended to determine thermal stability and chemical formula of the materials. Field-Emission Scanning Electron Microscopy (FE-SEM, Zeiss UltraPlus) operating at different high voltage (typically in between 15KV-20KV) was used to analyze micro-domain and particle sizes.

2.2 DIELECTRIC CHARACTERIZATION

2.2.1 IMPEDANCE SPECTROSCOPY

The complex impedance of samples was measured using an impedance analyzer (Agilent model 4192A LF) (Figure 2.1). Measurements were carried out at fixed applied voltage (10 mV) and varying frequency (typically 10^{2} to 1.2 ×10^{7} Hz). Impedance spectra were collected for 4–6 specimens of each sample to ensure reproducibility; average values were reported. The real and complex parts of the impedance, expressed as impedance magnitude and phase angle, were analyzed using a parallel RC circuit model

describing a “leaky” capacitor [57-59], yielding values of relative permittivity (ε_{eff}) given in equation (2.5) and loss tangent (tan δ) in equation (2.7) as functions of frequency. The complex permittivity of a material is given by

$$\varepsilon^* = \varepsilon_r' - j\,\varepsilon_r'' \tag{2.2}$$

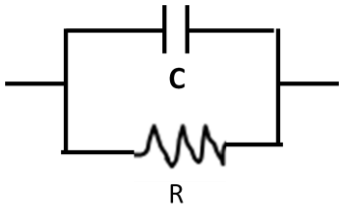

Scheme 2.1. Representation of parallel RC circuit.

$$|Z| = \frac{R\,X_C}{\sqrt{R^2 + {X_C}^2}} \tag{2.3}$$

$$\theta = \tan^{-1}\left(\frac{R}{X_C}\right) \tag{2.4}$$

here, $X_C = \frac{1}{\omega C}$, $\omega = 2\pi f$, ω is angular frequency $\left(\frac{rad}{s}\right)$, and f is frequency (Hz) .

Specifically, measured values of impedance magnitude |Z| in equation (2.2) and phase angle θ in equation (2.3) lead to the real and complex parts of the relative permittivity given by

$$\varepsilon_r^{'} = \frac{-\sin(\theta)}{2\pi f C_0 |Z|} \tag{2.5}$$

$$\varepsilon_r^{''} = \frac{\cos(\theta)}{2\pi f C_0 |Z|} \tag{2.6}$$

where f is frequency in Hz, $C_0 = \varepsilon_0 A/d$, and A and d are the film area and thickness. The loss tangent tan δ, also called the dielectric loss, is defined as

$$\tan\delta = \frac{\varepsilon_r''}{\varepsilon_r'} = \cot\theta \qquad (2.7)$$

The impedance analyzer was also used in "conductivity" mode to directly measure conductivity, which was multiplied by A/t to give specific conductivity values.

Figure 2.1. Impedance Analyzer (Agilent 4192A LF).

2.2.2 Polarization Measurements and Energy Storage Capability

Impedance spectroscopy provides low-voltage dielectric properties. Polarization testing, on the other hand, probes the behavior of dielectric materials under much higher applied electric fields. Polarization measurements at higher applied voltages employed a Precision Multiferroic polarization tester (Radiant, Inc.)(Figure 2.2). Polarization data (*D* versus *E*) were obtained for applied voltages up to 2000 V with a cycle frequency of 1.0 kHz. The maximum applied field strength depended on the sample film thickness and breakdown strength; typical maximum values of 30-50 kV/cm were achieved for CCTO/PC composites and over 1000 kV/cm for pure PC. Stored energy density $\left(\widehat{W}_s\right)$ was determined by numerical integration of *E* (Equation 1.3) from *D*=0 to the maximum value of *D* (D_{max}) achieved in the hysteresis loop. Recovered energy density $\left(\widehat{W}_r\right)$ was determined by numerically integrating *E* from D_{max} to the value of *D* where *E*=0. Percentage energy loss is computed as $100 \times \left(\widehat{W}_s - \widehat{W}_r\right)/\widehat{W}_s$.

Figure 2.2. From bottom to top; radiant ferroelectric tester, high voltage interface, and high voltage amplifier in a stack.

CHAPTER 3

CCTO - POLYCARBONATE COMPOSITES[1]

[1]This chapter has been adapted from "Dielectric Properties and Energy Storage Performance of CCTO/Polycarbonate Composites: Influence of CCTO Synthesis Route" by Md. Sayful Islam, W. Michael Chance, Hans-Conrad zur Loye, and Harry J. Ploehn, submitted to Journal of Sol-Gel Science and Technology.

[2]CCTO synthesized and X-ray characterized by Dr. W. Michael Chance in the Department of Chemistry and Biochemistry at the University of South Carolina.

3.1 INTRODUCTION

Microelectronics and various new compact capacitive devices require dielectric materials with exceptionally high dielectric constant. Often, these are ferroelectric and relaxor ferroelectric–based perovskites. The discovery of calcium copper titanate, $CaCu_3Ti_4O_{12}$ (CCTO), a perovskite-like (ABO_3) body-centered cubic oxide (Figure 3.1), has opened up a new avenue for dielectric material research. CCTO has received considerable attention as a possible dielectric material because of its so-called "giant" or "colossal" dielectric constant (CDC), which can range from $<10^2$ to more than 10^5 depending on temperature and applied field frequency.

Since the first reports of CDCs for CCTO [60-64], hundreds of papers have been published on this material. Several models have been proposed to explain the CDC of CCTO and continue to be debated. Onodera *et al.* [65] reported CCTO exhibits a cubic structure with the eight TiO_6 octahedra placed in the unit cell in a distorted configuration, which results in significant polarization under applied electric fields. Sinclair *et al.* [60, 63] carried out impedance spectroscopy measurements and demonstrated CCTO ceramics are electrically heterogeneous and consists of semiconducting grains with insulating grain boundaries (Figure 3.2). They asserted that the CDC phenomenon is attributed to a grain boundary (internal) barrier layer capacitance (IBLC) rather than an intrinsic property associated with crystal structure.

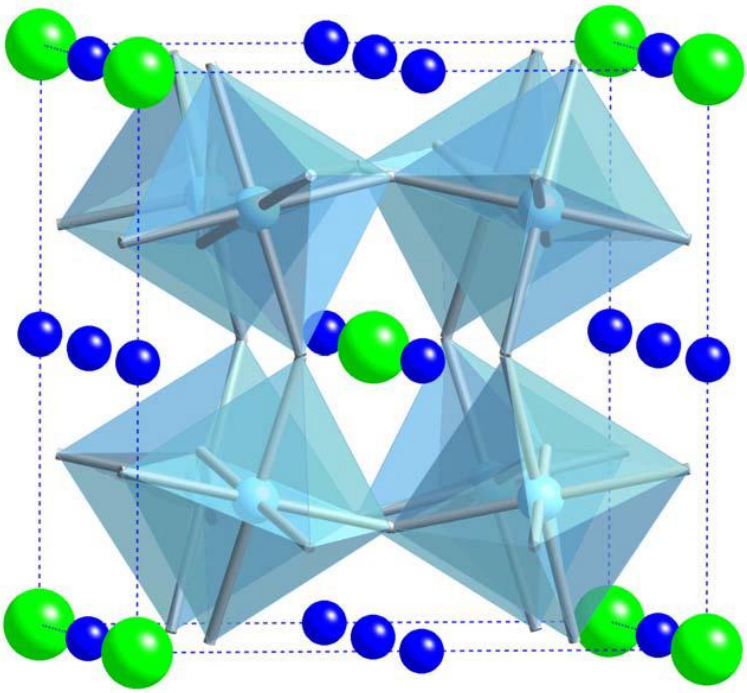

Figure 3.1. The unit cell structure of CCTO, with calcium ions in green, copper ions in blue, and TiO_6 octahedra in teal [1].

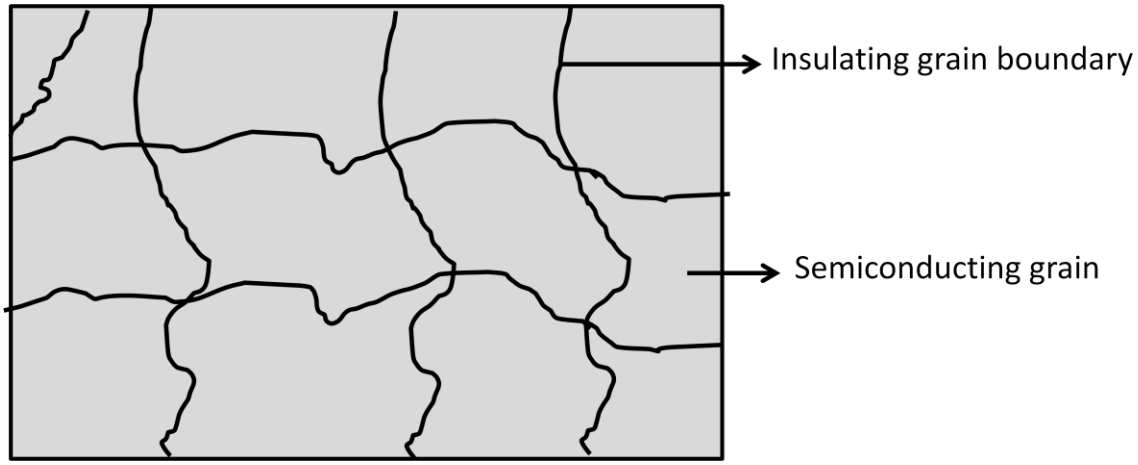

Figure 3.2. General schematic of the IBLC theory associated with CCTO's giant dielectric constant. Schematic redrawn based on a similar figure in reference [26] .

Lunkenheimer *et al.* [66] reviews this work, which focused mainly on establishing the polarization mechanisms responsible for CCTO's dielectric properties. Lunkenheimer

et al. conclude that although the cause of CDC behavior in CCTO cannot be unequivocally answered, internal and surface barrier layer capacitance (IBLC and SBLC) mechanisms certainly play a central role. The dielectric properties of CCTO thus depend on the grain size and grain boundary composition within CCTO particles, and the electronic properties of the phase interface between CCTO particles and neighboring materials.

Since pure CCTO possesses quite low breakdown strength, no more than 7 KV/cm [67], thin films of pure CCTO [67, 68] are not practical to achieve high dielectric energy density. To circumvent this issue and take advantage of simple processing methods and better mechanical properties afforded by polymers as well as CCTO's high ε_r values, several studies have explored CCTO-based polymer composites [24-35] . A majority of previously published work employed CCTO prepared from solid -state synthesis routes [24-26, 28, 31, 35]. One of the first studies [25] reports composite effective permittivity (ε_{eff}) values reaching 610 (at 100Hz, 25°C) for hot-pressed multilayers of 50 vol% solid state CCTO dispersed in P(VDF-TrFE) copolymer. This same group later showed [35] that only ball-milling the CCTO to produce nanoscale particles reduced the ε_{ff} values to 62. Modest ε_{eff} values (70-100) were reported for 50-55 vol% loading (and similar measurement conditions) for hot-pressed plaques of solid-state CCTO dispersed in PVDF homopolymer [30]. Studies of solid-state CCTO dispersed in other kinds of polymers also give ε_{eff} values in the range 30-80. The loss tangent values ($\tan\delta$) generally ranged from 0.05 to 0.20 at 100Hz. These values increase significantly

with field frequencies for PVDF and P (VDF-TrFE), but decreases for epoxy [28], polyethersulfone [31], and polyimide [26].

Several routes have been developed for sol-gel synthesis of CCTO [69-85], leading to recent studies of polymer composites based on sol-gel CCTO [27, 29, 32-34]. Thomas *et al.* [29] and Yang *et al.* [33] both used an oxalate precursor route to sol-gel CCTO and prepared PVDF composites. Thomas *et al.* [29] reported ε_{eff} values up to 90 and tanδ values of 0.14-0.16 (30 vol% CCTO, 100Hz, room temperature); ε_{eff} increases with CCTO loading and decreases as frequency increases. Yang et al. [33] report ε_{eff} values as high as 2.49×10^{6} with tanδ = 48 (40 vol% CCTO, 100Hz, room temperature). The composites of Yang et al. are more like semiconductors than dielectric materials. CCTO/PVDF composites incorporating citrate-based sol-gel CCTO have been prepared and characterized [32]; reported ε_{eff} and tanδ values are comparable to those of Thomas et al. [29] . Oxalate–based sol-gel CCTO blended with polyimide [34] exhibits dielectric properties like those of percolative composites [1, 86]. Clearly, the dielectric properties of polymer composites based on sol-gel CCTO are sensitive to the details of CCTO synthesis, particle-polymer blending, and film preparation.

CCTO-polymer composites could serve as dielectric energy storage materials if they manifest high energy density and high breakdown strength. All the work published to date on CCTO-based composites has focused on relative permittivity and loss tangent. Only one study [29] reported results on breakdown strength. To the best of our

knowledge, no studies of CCTO composites have reported high field polarization results, including D-E loops, stored and recovered energy densities, and percentage energy loss.

This chapter discusses the dielectric properties and energy storage performance of CCTO-polycarbonate composites. Special attention is given to the effect of CCTO particle size on microstructure, low-field dielectric properties (ε_{ff} and $\tan\delta$), and polarization behavior. To explore the impact of CCTO particle size and interfacial area, CCTO was prepared via the traditional solid state method as well as a wet chemical sol-gel method. Polycarbonate was chosen as polymer matrix due to its high break breakdown field strength and low loss. Our objective is to produce CCTO-polycarbonate composites with not only high ε_{eff} values, but also low loss and high stored energy density.

3.2 Materials and Experimental Method

3.2.1 CCTO Synthesis❷

Two methods were used to synthesize CCTO. "Solid-state" CCTO (ssCCTO) was synthesized following established procedures [60, 62-64]. Stoichiometric amounts of $CaCO_3$ (Alfa Aesar, 99.95%), CuO (Cerac, 99.999%), and TiO_2 (Alfa Aesar, 99.9%) were ground together in a mortar and pestle and heated at 1000˚C for 12 hours. This grinding/heating sequence was performed a total of three times with 100˚C increases in heating temperature for the second and third calcinations.

"Sol-gel" CCTO (sgCCTO) was synthesized using procedures similar to those reported previously [73, 79]. First, a Ti solution was made using 16 mmol of

titanium isopropoxide (Acros, 98+%) and 24 mmol of glacial acetic acid. The solution was prepared in a glove bag under the flow of nitrogen gas and allowed to mix for 30 min. While the first solution was mixing, a second Cu/Ca solution was prepared by mixing 12.0 mmol of $Cu(Ac)_2 \bullet H_2O$, 4 mmol $Ca(NO_3)_2$, and 4 mmol of glacial acetic acid in a beaker, followed by dilution with 250 mL absolute ethanol under constant stirring and low heat to achieve complete dissolution. Next, the Ti solution was poured into the Cu/Ca solution, producing a green sol that is stable against hydrolysis by atmospheric moisture for extended periods. Polyethylene glycol (PEG, either 8.0 or 100.0 g) was added to the solution as a dispersant; these samples are denoted as sg_8CCTO and sg_{100}CCTO, respectively. To initiate hydrolysis and form the gel, nitric acid (3.0 M) was added drop wise until the pH reached ~1.4. The mixture was stirred continuously and gently heated. A pale blue gel formed within 2 h and then was aged for 6 h. Solvent was evaporated from the gel in an oven at 200°C. The dried solids were then calcined in air an oven at 600°C for 6 h.

3.2.2 Preparation of CCTO/Polycarbonate Composites

Polycarbonate pellets (MAKROLON 3108, Bayer Material Science LLC) were dissolved in dichloromethane (CH_2Cl_2 99.5+%, Alfa Aesar) via continuous stirring for at least 4 h to prepare solutions with concentrations of 33-35 mg/mL. Then CCTO powder was dispersed in the solution and stirred for an additional 4 h. The slurry was spin-coated onto a silicon wafer rotating at 350 rpm. The CH_2Cl_2 solvent was removed by evaporating in a vacuum oven at 45˚C and at reduced pressure (635 mmHg absolute) for 24 hours. Gentle peeling from the wafer gave freestanding CCTO/PC films of uniform

thickness (typically 40-65 μm) and minimal defects. Circular Au electrodes were deposited on both sides of the films by sputter coating through a shadow mask in an Ar atmosphere.

3.2.3 Characterization Methods

The microstructure and size of the CCTO particles were characterized via SEM images (Zeiss Ultraplus Thermal FE-SEM). FE-SEM was also used to image composite surfaces, including exterior and internal fracture surfaces. The surface areas of CCTO particles were obtained from N_2 gas absorption with BET analysis (Micromeritics, model ASAP 2020). ❷Powder X-ray diffraction (PXRD) patterns for CCTO samples were collected (instrument specifications are given in section 2.1) over the 2θ range of 2-80° with a step size of 0.04° and a scan speed of 0.25°/min. Diffraction peaks were matched to the JCPDF patterns of $CaCu_3Ti_4O_{12}$, $CaTiO_3$, and CuO for identification. Phase fractions were quantified using the PDXL software program from Rigaku via the relative intensity ratios (RIR) method. Particle size analysis was performed using the Scherrer equation with LaB_6 (NIST SRM 660a) serving as the standard for instrumental broadening [55, 56].

The complex impedance of CCTO/PC film samples was measured using an impedance analyzer, and polarization measurements employed a polarization tester, as described in Chapter 2.

3.3 Results and Discussion

3.3.1 CCTO Particle Characterization

The phase purity of the CCTO particles synthesized via solid state and sol-gel methods have been analyzed by X-ray diffraction (Figure 3.3). The ssCCTO material contains a small (~3%) impurity of CuO with no other observed peaks. The sg_8CCTO powder contains small impurities of both $CaTiO_3$ (~1.5%) and CuO (~4.3%). The similarity of the two XRD patterns indicates that the sol-gel CCTO has the same crystalline structure as CCTO prepared through the traditional solid state method.

FESEM images (Figure 3.4) of CCTO particles obtained from two different synthesis routes show remarkable differences in morphology. Figure 2a shows that ssCCTO has particles sizes in the 2-8 µm range with an average size nearly 4 µm. Figures 2b and 2c show well defined primary particles with characteristic sizes in the 100-200 nm range, with apparent agglomeration or sintering producing ramified aggregates. Comparing Figures 2b and 2c, the particles size of sg_8CCTO appears to be somewhat smaller than sg_{100}CCTO. However, it is difficult to extract qualitative results and draw conclusions from these images. PXRD and the Scherrer equation (equation 2.1) yield estimates of 145±28 and 77±28 nm for the average particle sizes of sg_8CCTO and sg_{100}CCTO, respectively.

Nitrogen gas adsorption with BET analysis gives a surface area of $\hat{S}$=0.35±0.05 m^2/g for ssCCTO powder. Assuming spherical particles ($\hat{S} = 6/\rho d$) and $\rho = 4.8\ g/cm^3$ for CCTO [78] gives an equivalent sphere diameter of 3.6 µm. For the same assumptions,

sg_8 CCTO's surface area $\hat{S}$=6.81±0.08 m^2/g gives an equivalent diameter of 184 nm. Both measurements show that sgCCTO particles are 20 to 40 times smaller than ssCCTO particles.

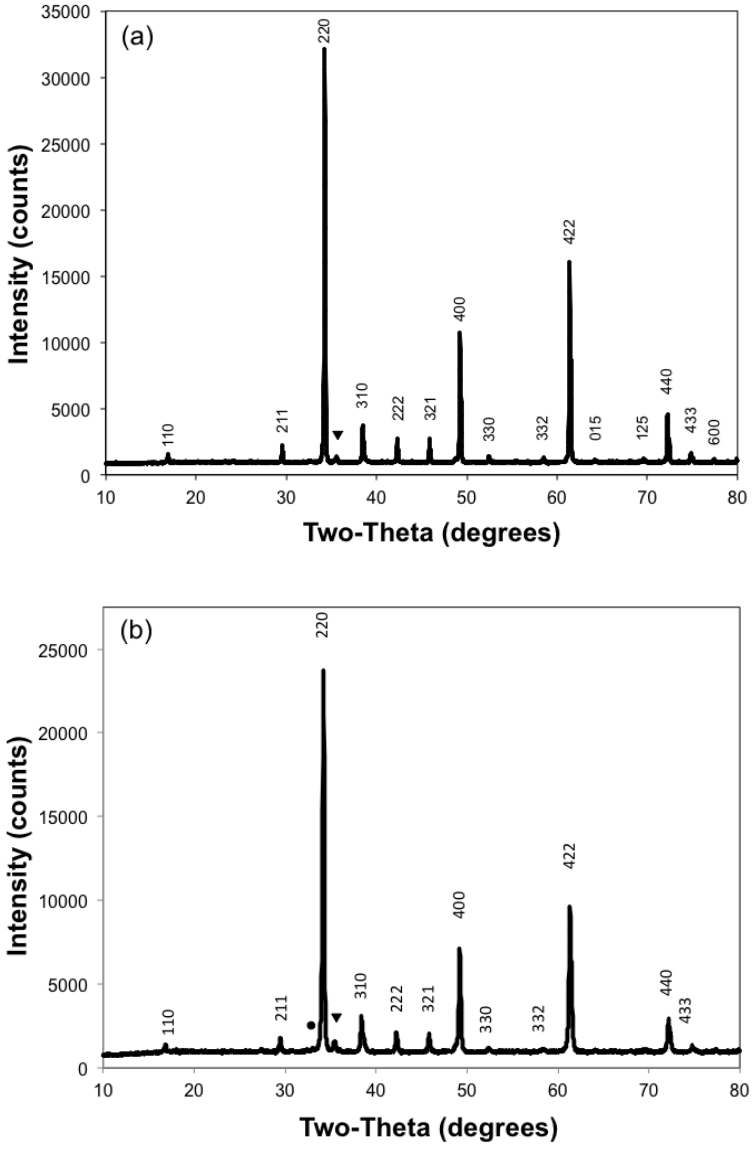

Figure 3.3. Powder X-ray diffraction patterns of (a) ssCCTO and (b) sg_8CCTO. The triangles represent 100% peaks from CuO; the circle (b) represents the 100% peak from $CaTiO_3$.

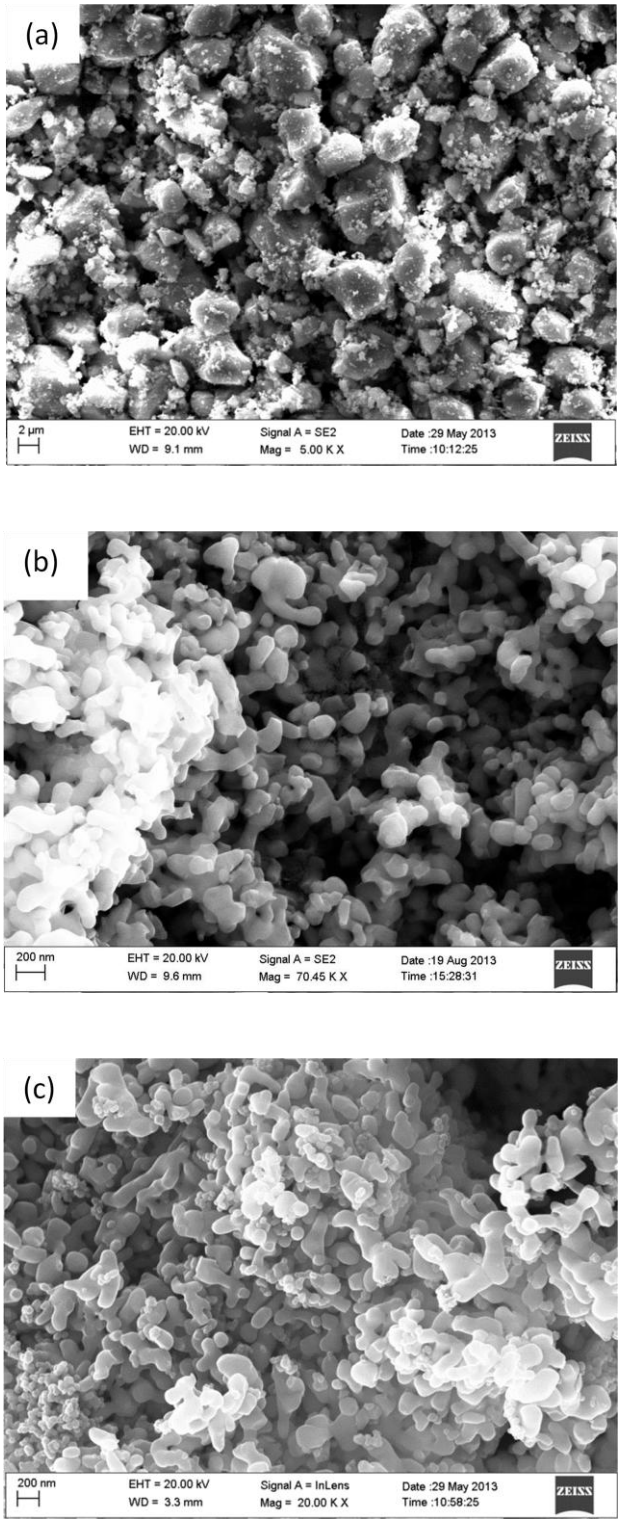

Figure 3.4. FESEM images of CCTO particles: (a) ssCCTO, 2 µm scale; (b) sg_8CCTO, 200 nm scale; and (c) sg_{100}CCTO, 200 nm scale.

3.3.2 CCTO/PC COMPOSITE MICROSTRUCTURE

Solution blended CCTO/PC slurry was spin coated on Si wafers, and solvent evaporation yielded CCTO/PC composite films with uniform thickness. The films are carefully peeled from the wafers to give free-standing films. Figure 3.5 shows FESEM images of the wafer sides of various 10 vol% CCTO/PC composites. Some agglomeration of CCTO particles is observed, but in all cases the particles appear to be uniformly dispersed in the PC matrix. Comparing Figures 3b and 3c, the different amounts of PEG in the sgCCTO samples do not appear to have a significant effect on the degree of sgCCTO dispersion in the PC matrix.

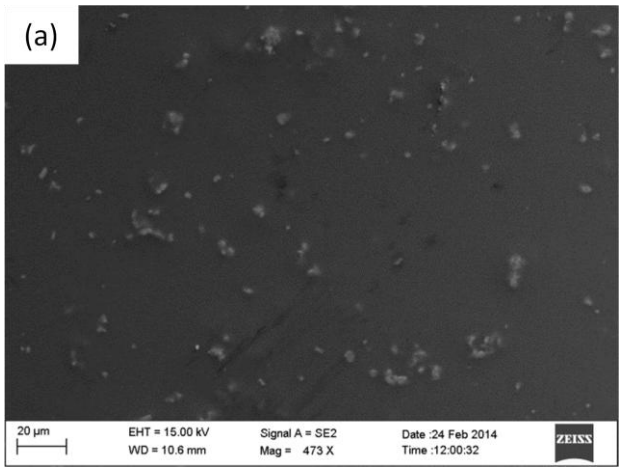

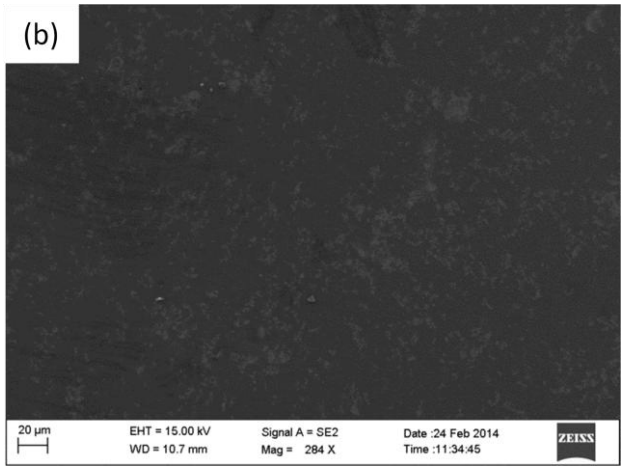

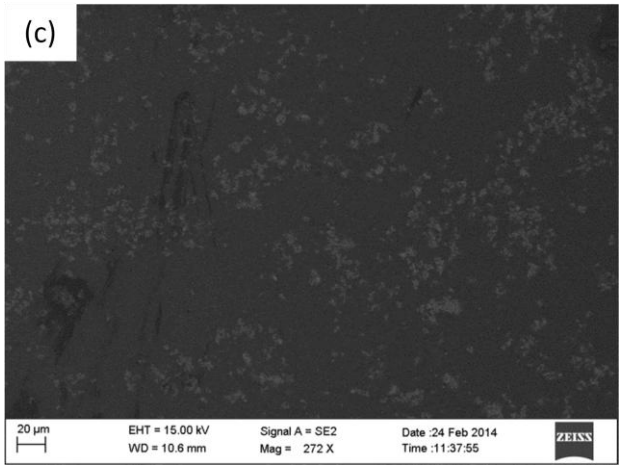

Figure 3.5. FESEM images of 10 vol% CCTO/PC composite film surfaces (wafer side): (a) ssCCTO/PC, (b) sg_8CCTO/PC, and (c) sg_{100}CCTO/PC. Scale bars are 20 µm in all images.

3.3.3 CCTO/PC Composite Dielectric Properties

Figure 3.6a shows the frequency-dependent relative permittivity of PC and CCTO/PC composites prepared with ssCCTO and sg_8CCTO. For pure PC, ε_{eff} = 3.1 and is nearly independent of frequency. For CCTO/PC composites, ε_{eff} is 4 to 12 times higher than that of PC and increases with CCTO vol%, as expected. The composites' ε_{eff} values decrease gradually with increasing frequency; the trend is most pronounced for 20 vol% sg_8CCTO/PC. For both 10 and 20 vol% loadings, ε_{eff} for sg_8CCTO/PC is larger than that for ssCCTO/PC, especially at the low end of the frequency range. For example, at 1 kHz, ε_{eff} is about 20% larger for sg_8CCTO/PC compared to ssCCTO/PC at both 10 and 20 vol%.

Considering the fact that the sg_8CCTO particles are at least 20 times smaller than ssCCTO particles, the magnitude of the permittivity enhancement in sg_8CCTO/PC relative to ssCCTO/PC is surprisingly modest. The apparent size of the CCTO particles seems to have only a small effect on the composites' relative permittivity. Instead, the presence of PEG in the sol-gel CCTO may play a more prominent role by enhancing the

conductivity of the grain boundaries. The loss tangent (Figure 3.6b) and specific conductivity data (Figure 3.6c) support this explanation. Clearly both ssCCTO/PC and sg_8CCTO/PC composites have significantly higher values of loss tangent and specific conductivity than pure PC. Moreover, loss tangent and conductivity both increase with CCTO vol%. Figure 3.6b shows that the loss tangent values for sg_8CCTO/PC composites are generally 100 to 300% higher than those for ssCCTO/PC composites at the same frequency and vol% CCTO loading. The specific conductivity (Figure 3.6c) shows a similar trend, with higher values for sg_8CCTO/PC composites compared to ssCCTO/PC composites at the same frequency and vol% CCTO loading.

One might expect that the much smaller particle size of sg_8CCTO would lead to smaller grain sizes and thus much higher composite permittivity values. It is possible that higher grain boundary conductivity mitigates the enhancement produced by smaller sg_8CCTO grain size. In effect, more conductive grain boundaries might produce polarizable domains consisting of multiple sg_8CCTO grains. This is consistent with previous work [83] in which addition of poly(vinyl alcohol) to sgCCTO increased Cu ion segregation at grain boundaries, thus increasing grain boundary conductivity and decreasing breakdown field strength.

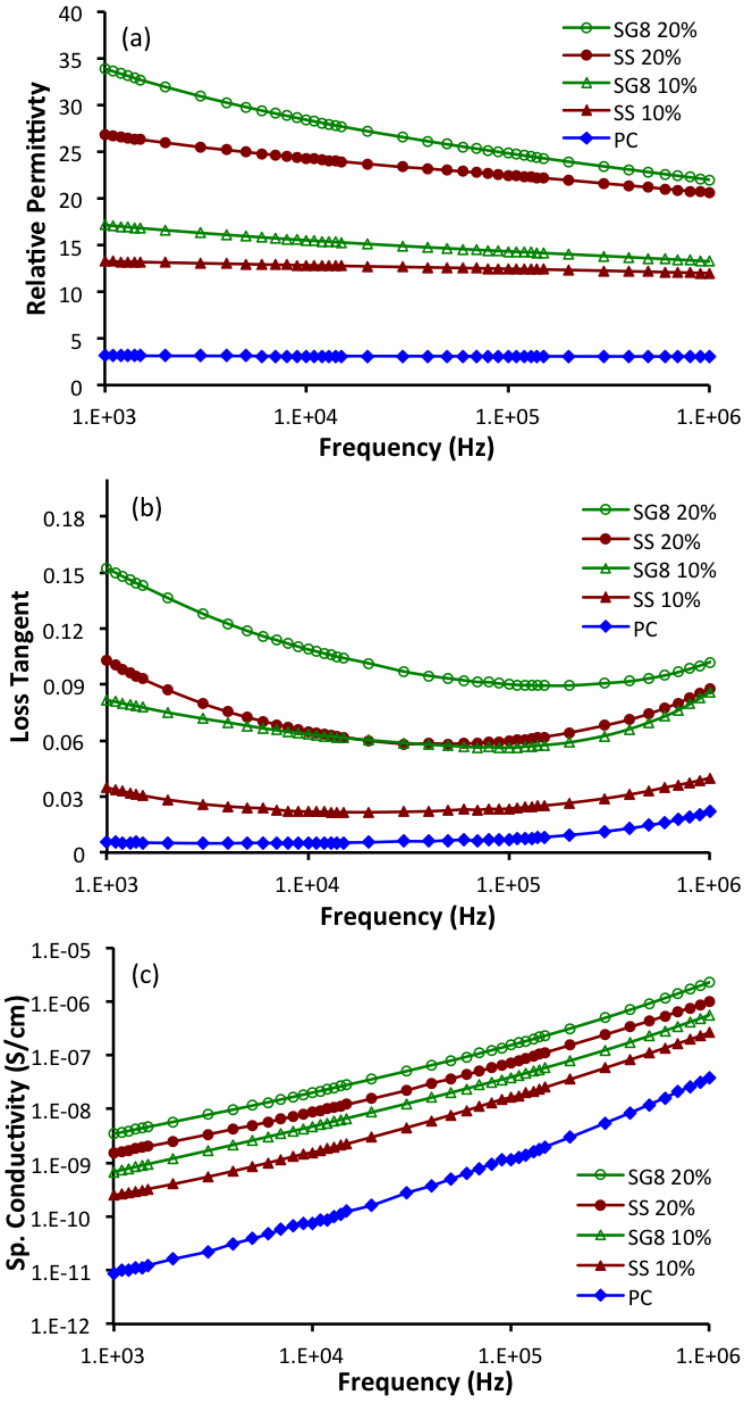

Figure 3.6. Effect of CCTO synthesis method on frequency-dependent relative permittivity (a), loss tangent (b), and specific conductivity (c) of CCTO/PC composites: ssCCTO (filled red symbols) or sg_8CCTO (open green symbols); triangles and circles denote 10 and 20 vol%, respectively. Blue diamonds denote data for pure PC.

Sol-gel CCTO was prepared with excess PEG (sg_{100}CCTO) in an attempt to reduce grain size and increase permittivity. Figure 3.7 compares the dielectric properties of sg_8CCTO/PC and sg_{100}CCTO/PC composites. Results for ε_{eff} (Figure 3.7a) show that the amount of added PEG in sgCCTO does not have a significant effect on relative permittivity. Although PXRD results suggest a smaller grain size (77±28 nm) for sg_{100}CCTO (compared to 145±28 nm grain size for sg_8CCTO), particle sizes seen in FESEM images (Figure 3.4) do not appear to differ significantly. Figure 3.7b shows that sg_{100}CCTO/PC composites have much larger loss tangent values at frequencies below 20 kHz. This may be rationalized by higher Cu ion conductivity in grain boundaries due to the presence of excess PEG in sg_{100}CCTO.

As an additional test of PEG as a dispersant, 20 g of PEG was dissolved with 2.5 g of ssCCTO in excess ethanol, dried, and then solution-blended with PC to prepare composites. Figure 3.8 shows the dielectric properties of this ss_{20}CCTO/PC composite. Adding PEG to ssCCTO results in significant decreases in ε_{eff} for both 10 and 20 vol% loadings and at all frequencies. The added PEG produces a relatively small increase in loss tangent values at low frequency (Figure 3.8b), with no clear effect on specific conductivity (Figure 3.8c). We speculate that PEG, adsorbed on the CCTO particles, may bind Cu ions that otherwise might contribute to dielectric polarization. More work will be needed to test this hypothesis.

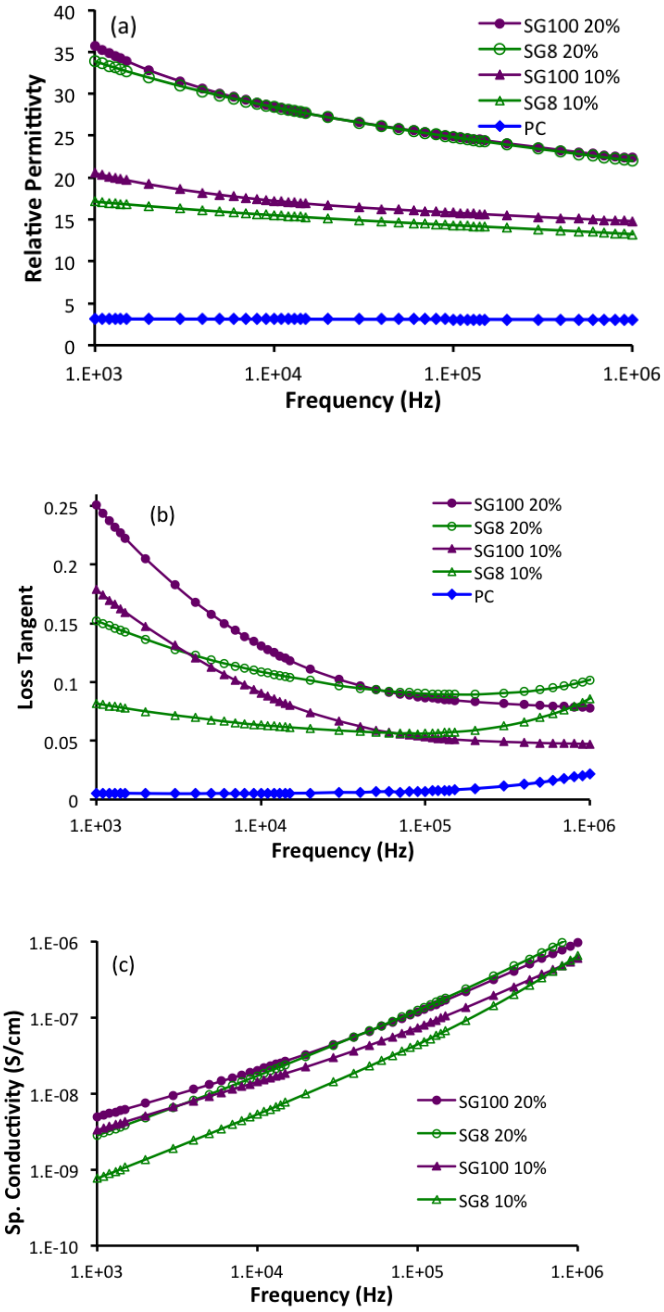

Figure 3.7. Effect of added PEG amount in sgCCTO synthesis on frequency-dependent relative permittivity (a), loss tangent (b), and specific conductivity (c) of CCTO/PC composites: sg_8CCTO (open green symbols) or sg_{100}CCTO (filled purple symbols); triangles and circles denote 10 and 20 vol%, respectively. Blue diamonds denote data for pure PC [omitted from (c)].

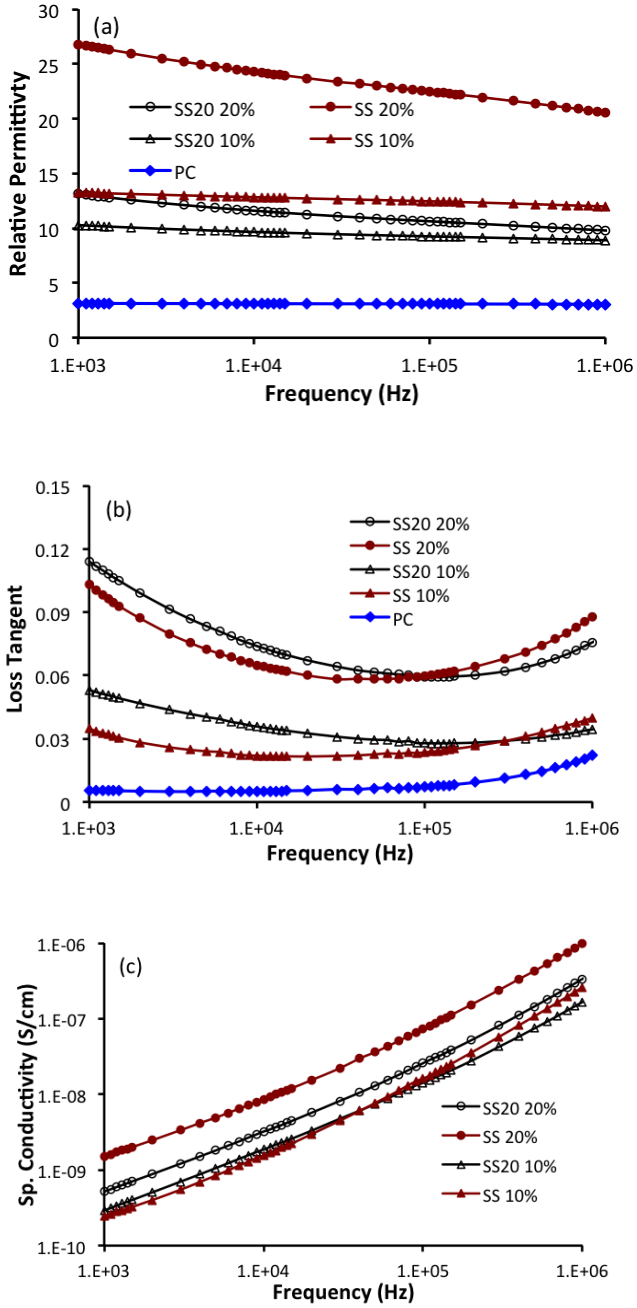

Figure 3.8. Effect of added PEG on frequency-dependent relative permittivity (a), loss tangent (b), and specific conductivity (c) of ssCCTO/PC composites: ssCCTO (no added PEG, filled red symbols) or ss_{20}CCTO (20 g added PEG, open black symbols); triangles and circles denote 10 and 20 vol%, respectively. Blue diamonds denote data for pure PC [omitted from (c)].

3.3.4 Polarization and Energy Storage

Impedance spectroscopy provides low-voltage dielectric properties. Polarization testing, on the other hand, probes the behavior of dielectric materials under much higher applied electric fields. Figure 3.9 shows typical polarization (*D*-*E*) loops for PC and CCTO/PC composites. Pure PC displays nearly linear polarization behavior. Upon polarization to similar maximum field strengths, CCTO/PC composites show considerable nonlinearity, remanent polarization, and hysteresis. The apparent ferroelectric behavior is clearly due to the added CCTO. sgCCTO/PC composites generally exhibit greater *D* values than ssCCTO/PC composites at the same CCTO loading and applied field strength *E*. Trends in the hysteresis magnitude (i.e., the size of the loop) are not obvious from the *D*-*E* curves, however.

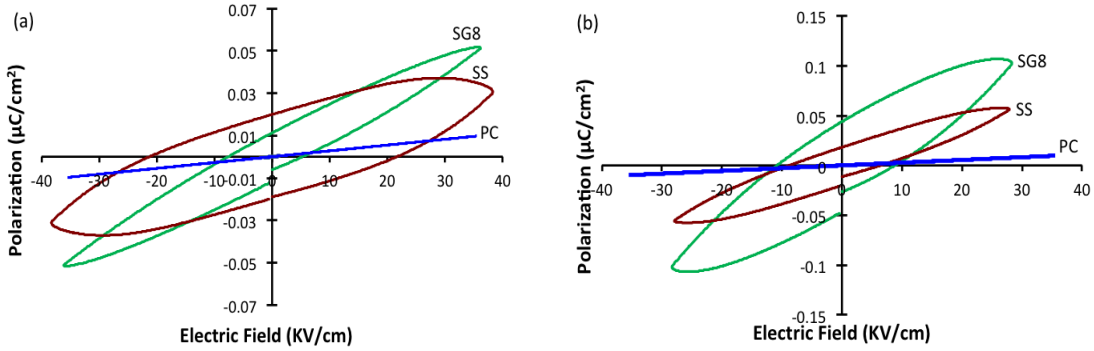

Figure 3.9. Polarization as a function of applied electric field for PC and CCTO/PC composites: (a) 10 vol% and (b) 20 vol% ssCCTO or sg_8CCTO (SS and SG8, respectively). Cycle frequency was 1 kHz.

Integration of the *D-E* data using Eqn. 1.3 gives the stored and recovered energy densities $(\widehat{W}_s, \widehat{W}_r)$ as well as the percentage energy loss (Figure 3.10). Typically, we find that pure PC films can be subjected to applied field strengths in excess of 1000 kV/cm (100 MV/m) before breaking down; this is somewhat less the value of 252 MV/m reported elsewhere for PC [5] . The maximum stored and recovered energy densities for pure PC are 154 and 145 mJ/cm^3, respectively, with energy loss values below 5% except near the breakdown field strength.

The results for CCTO/PC composites are quite different. The addition of CCTO (either solid-state or sol-gel) significantly reduces the composites' breakdown field strength relative to pure PC (Figures 3.10 a and b). Among the composites, 10 vol% sg_8CCTO/PC films fail at fields about 80 kV/cm. Higher sg_8CCTO loading or incorporation of ssCCTO further reduces the breakdown field strength. Consequently, the maximum values of $\widehat{W}_s$ and $\widehat{W}_r$ are about 20 and 5.5 mJ/cm^3 (respectively) for 10 vol% sg_8CCTO/PC, with significantly lower values for the other CCTO/PC composite films. All of the CCTO/PC composites manifest significant percentage energy losses, with values exceeding 60% at field strengths greater than 30 kV/cm (Figure 3.10c). These results are attributed to the conductivity and ferroelectric behavior of the added CCTO particles. Smaller sgCCTO particles appear to allow us to reach higher polarization levels compared to composites with much larger ssCCTO particles, but the advantage is not great compared to the polarization levels and maximum $\widehat{W}_r$ values achieved in pure PC.

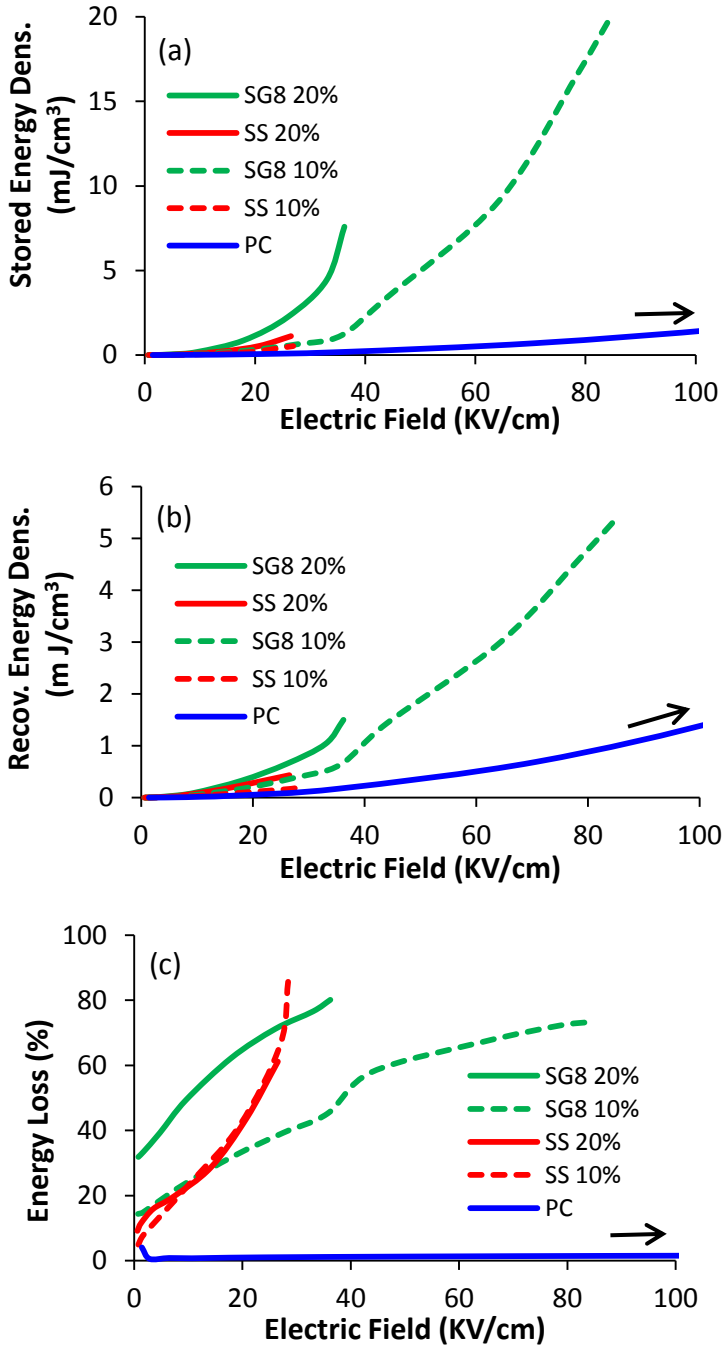

Figure 3.10. Stored energy density (a), recovered energy density (b), and percentage energy loss (c) for PC and CCTO/PC composites as functions of applied electric field. ssCCTO/PC and sg_8CCTO/PC composites are denoted as SS and SG8 with indicated values of vol% CCTO. The arrows indicate that the data for pure PC extend beyond the plots' range of applied electric field.

Nonetheless, comparisons at low applied electric field values are still informative. For sg_8CCTO/PC films, $\widehat{W}_s$ and $\widehat{W}_r$ values are many times higher than those of pure PC, and the values increase with sgCCTO loading. However, the percentage energy losses are high and scale with sgCCTO loading. Stored and recovered energy densities are higher in sgCCTO/PC composites compared to ssCCTO/PC. In terms of percentage energy loss, sgCCTO does not provide any significant improvement. In general, the primary advantage of sgCCTO/PC is that it can be polarized to somewhat higher applied fields, and thus reach higher $\widehat{W}_r$ values, compared to ssCCTO/PC.

3.4. CONCLUSIONS

The colossal dielectric constant of CCTO has motivated the exploration of its use as a high-ε_r filler in polymer composites. Several studies [25, 29, 30, 32, 33, 35] have blended either solid-state or sol-gel CCTO with PVDF or its copolymers, attempting to maximize the composites' effective permittivity, ε_{eff}. These studies report relatively high loss tangent values with little comment as to the underlying explanation. PVDF is well known to exhibit significant dielectric loss, so perhaps the polymer tacitly gets the blame. No studies have reported values of stored and recovered energy densities for CCTO/polymer composites.

To explore this topic, we blended CCTO with PC, a polymer known to have high breakdown field strength and low dielectric loss. We employed CCTO synthesized by both the solid-state and sol-gel routes. Results from impedance spectroscopy (and low applied electric fields) reveal the expected, significant enhancement of ε_{eff} relative to

the permittivity of pure PC. Despite the 20-fold smaller size (and 20-fold higher surface area) of sol-gel CCTO particles, the ε_{eff} values for sgCCTO/PC composites were only moderately higher relative to the values for ssCCTO/PC. The loss tangent values for all CCTO/PC composites were much higher than for pure PC. Loss tangent values for sgCCTO/PC composites were significantly higher than those for ssCCTO/PC. Increasing quantity of PEG in the sgCCTO synthesis exacerbated the increase in loss tangent. While this implicates PEG as a contributor to dielectric loss, clearly the CCTO is primarily responsible.

Considering the impedance results, the significant hysteretic losses in CCTO/PC composites polarized at higher electric fields should not be a surprise. Addition of CCTO to PC dramatically reduces the breakdown field strength and maximum stored and recovered energy densities. Although sgCCTO offers some advantage, possibly due to its smaller particle size, these composites manifest relatively high percentage energy losses. sgCCTO/PC composites may have value in applications requiring high dielectric permittivity at low field strengths. However, CCTO/PC composites are not good candidates as dielectrics for high density, pulse power energy storage.

CHAPTER 4

ALL-POLYMER MULTIPHASE DIELECTRIC MATERIALS

❸ Adapted from "Oligoaniline-Containing Supramolecular Block Copolymer Nanodielectric Materials" by Christopher G. Hardy, Md. Sayful Islam, Dioni Gonzalez-Delozier, Harry J. Ploehn, and Chuanbing Tang , published in Macromolecular Rapid Communications, 33, 791−797,2012

❹Adapted from "Converting an Electrical Insulator into a Dielectric Capacitor: End-Capping Polystyrene with Oligoaniline" by Christopher G. Hardy, Md. Sayful Islam, Dioni Gonzalez-Delozier, Joel E. Morgan,Brandon Cash, Brian C. Benicewicz, Harry J. Ploehn, and Chuanbing Tang, published in Chemistry of Material , 25, 799−807, 2013.

❺SAXS measurements were performed by Joel E Morgan, the Department of Material Science and Engineering at the Pennsylvania State University.

❻Adapted from "Polymers Containing Highly Polarizable Conjugated Side Chains as High-Performance All-Organic Nanodielectric Materials" by Yali Qiao , Mohammed Sayful Islam , Kuo Han , Eric Leonhardt , Jiuyang Zhang ,Qing Wang , Harry J. Ploehn , and Chuanbing Tang, published in Adv. Funct. Mater., 23, 5638−5646, 2013.

❼Adapted from "Oligothiophene-Containing Polymer@BaTiO3 Hybrid Nanoparticles: A Binary Dipole Strategy toward High-Performance Nanodielectric Nanocomposite Systems" by Yali Qiao, Md. Sayful Islam, Lei Wang, Yi Yan, Jiuyang Zhang, Brian C. Benicewicz, Harry J. Ploehn, Chuanbing Tang, submitted to Advanced Energy Material , 2014.

4.1 INTRODUCTION

Poor compatibility between the organic polymer matrix and inorganic fillers leads to aggregation and defects, ultimately resulting in leakage and high dielectric loss [87], high leakage currents, and reduced breakdown strength of the organic-inorganic composites. To address these issues, “all-polymer” multiphase dielectric materials have been developed. Compared with organic-inorganic composites, all-organic dielectric composite materials have several advantages including facile processability, light weight and possibly low cost. Generally, all-organic composite approaches involve the use of high dielectric organic particulates embedded in the polymer matrix [88-94]. Similar to the organic-inorganic composite approach, a potential problem facing organic particulates dispersed in a polymer matrix is the tendency of undesirable macro-phase separation. In our approach, highly polarizable, conducting particulates (nano-domains) are embedded within an insulating matrix through appropriate polymer design, which hopefully gives chemical integrity to circumvent macro-phase separation.

The goal of this approach is to design micro-and nano-phase separated block copolymers that store energy via electronic conduction and interfacial polarization. These materials are constructed by spontaneous phase separation to form dispersed and conductive nanoscale domains embedded in an insulating polymer matrix, and are expected to achieve full interfacial compatibility and high interfacial areas. One block (red) forms nanodomains with high electronic conductivity, while the other block (blue) insulates the conductive domains to prevent percolation and to minimize inter-domain

conduction (Figure 4.1). Under an external applied field, electronic conduction will induce “nanodipoles” along the phase boundary due to space charge accumulation at the domain interfaces.

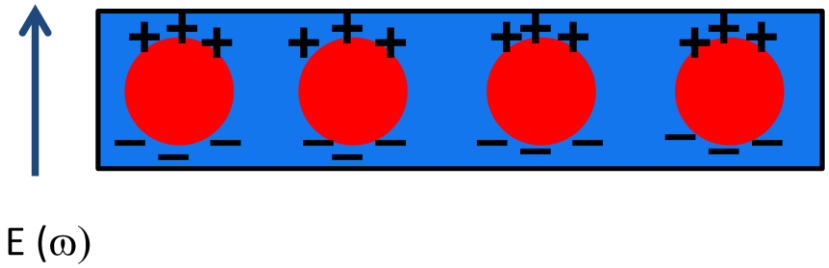

Figure 4.1. Controllable nanoscale morphology of multiphase all-polymer composites.

The nanoscale size of the phase separated domains greatly amplifies the interfacial area per unit volume, resulting in dielectric materials with energy storage dominated by interfacial polarization. Dielectric properties can be tailored by manipulation of chemical structures and molecular compositions of the block copolymers. This chapter describes polymer containing oligoaniline (OANI), π-conjugated oligothiophene blocks and explores their potential applications in advanced dielectric energy storage device. Specifically, the following candidate materials were investigated:

1) **Oligoaniline (OANI)-containing polymers**

    A) Oligoaniline-containing supramolecular block copolymers.

    B) Polystyrene (PS) end-capped with oligoaniline blocks.

2) **Oligothiophene-containing polymers**

A) Methacrylate polymers containing terthiophene side groups (PTTEMA).

B) Comparison of PTTEMA-b-PS block copolymers with PTTEMA+PS homopolymers blends.

C) Oligothiophene-containing polymer grafted on $BaTiO_3$ nanoparticles.

4.2 OLIGOANILINE (OANI)-CONTAINING SUPRAMOLECULAR BLOCK COPOLYMERS❸

4.2.1 POLYMER ARCHITECTURE

This section describes our initial findings of the first nanodielectric materials based on oligoaniline-containing supramolecular block copolymers. To utilize the high conductivity of aniline segments along with easy processability and tunability of block copolymers, block copolymers with an insulating segment, poly(methylacrylate), and a segment containing a strong acidic dopant moiety, poly-(2-acrylamido-2-methyl-1-propanesulfonic acid) (PAMPSA) that actively interacts with OANI, were prepared (Figure 4.2). The interaction of PAMPSA and OANI forms a dopant-conjugated complex. The block copolymers were prepared by reversible addition fragmentation transfer (RAFT) polymerization method. Details of the synthesis and polymer physical characterization are described in our publication [50]. These OANI-containing block copolymers are expected to produce phase-separated microdomains in which highly polarizable and conductive OANI+PAMPSA domains are dispersed in an insulating PMA matrix. Thus, under applied electric field, electronic polarization is expected to occur at the PMA-PAMPSA interface. The high interfacial area of micro-phase separated domains

amplifies the polarization, leading to high dielectric permittivity (Figure 4.3). In order to target various morphologies, a series of PAMPSA-b-PMA diblock copolymers (Table 4.1) were prepared by changing molecular weight of PMA block while keeping molecular weight of PAMPSA macroinitiator the same. All OANI-doped PMA-b-PAMPSA copolymers were synthesized and characterized (^{1}H-NMR, GPC, and UV-vis spectra) by Dr. Christopher Hardy [50, 95].

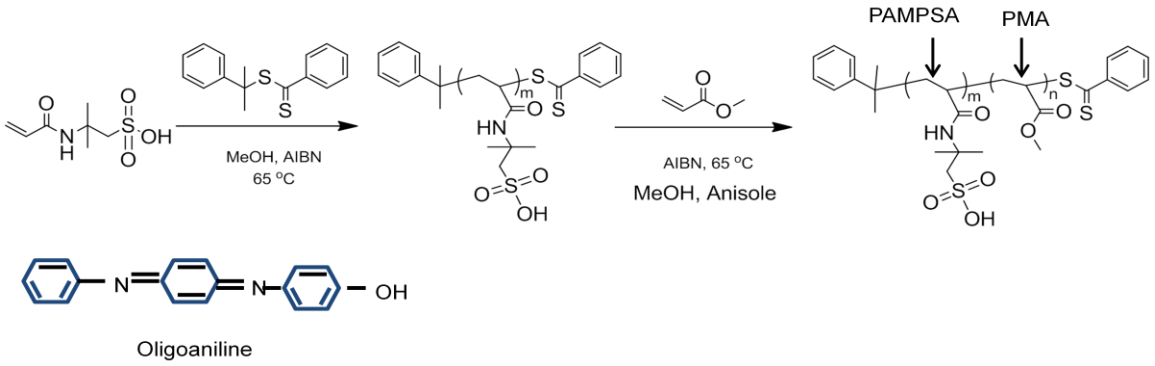

Figure 4.2. Synthesis of block copolymer PAMPSA-b-PMA by RAFT [50].

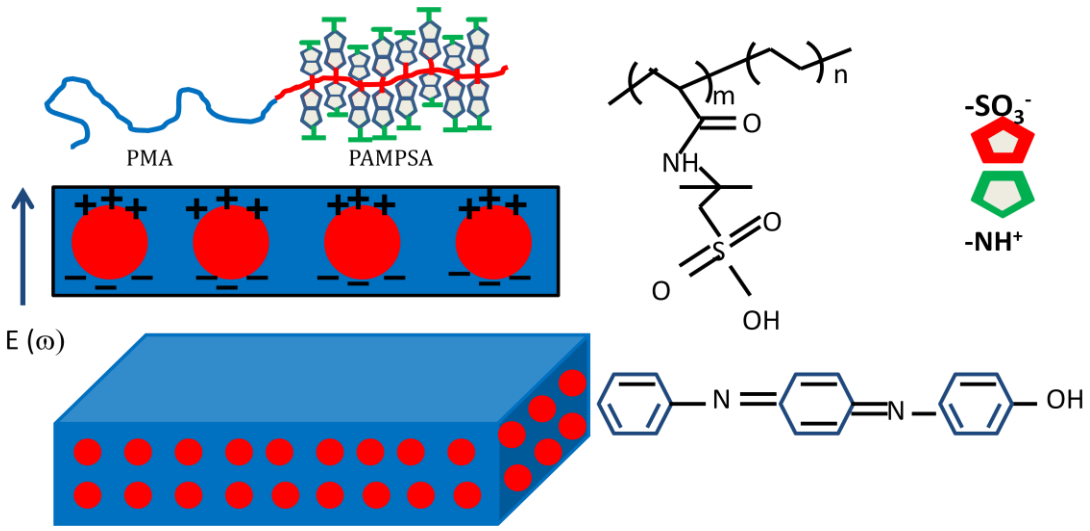

Figure 4.3. Nanodielectric materials using microphase-separated block copolymers consisting of an insulating poly(methyl acrylate) matrix, and dispersed and conductive

domains formed via ionic interactions between poly(2-acrylamido-2-methyl-1-propanesulfonic acid) segment and oligoaniline. Adapted from reference [50].

Table 4.1. Characterization of poly-(2-acrylamido-2-methyl-1-propanesulfonic acid)–b-Poly (methyl acrylate) (PAMPSA-b-PMA) polymers, NMR and GPC characterization performed by Dr. Christopher Hardy. Table is adapted from reference [50].

Materials	DP_{PAMPSA} (NMR)	DP_{PMA} (NMR)	(g/ mol, NMR)	(wt%) PAMPSA	PDI (GPC)
0	48	--	9900	100	1.18
1	48	392	43,600	23	1.21
2	48	785	77,400	13	1.30
3	48	1927	175,600	6	1.42

4.2.2. Film Preparation and Dielectric Characterization

Polymer samples were dissolved in dimethylformamide (DMF) at concentrations of 0.168 g/mL (undoped copolymers) or 0.034 g/mL (doped, washed copolymers) and poured into heavy- gauge aluminum pans. The solvent was removed by evaporation at 70°C under reduced pressure (125 mm Hg absolute) for 24 h. This temperature and pressure accelerated the evaporation of DMF (153°C normal boiling point) without producing solvent bubbles. After solvent evaporation, all films were annealed at 120°C in air for 24 h and then cooled for another 24 h. For copolymers 1-3 (listed in Table 4.1), these procedures resulted in films with uniform thickness and free of bubbles, cracks, or other defects. Film thicknesses were measured at multiple positions with a micrometer;

measured thicknesses ranged from 4 to 30 µm. Strips of aluminum pan bearing copolymer films were cut using scissors. The aluminum pan served as the bottom electrode for dielectric measurements. Circular gold electrodes (area 1.13 cm^2) were deposited on the films' top surfaces by sputter coating in an argon atmosphere through a shadow mask.

Impedance spectroscopy was used to measure the low-field dielectric properties (complex permittivity and conductivity). The details of these measurements and the analysis of the data are described in chapter 2 (section 2.2.1).

4.2.3. Dielectric Properties: Results and Discussion

The dielectric properties of the undoped PAMPSA-b-PMA block copolymers, as well as the copolymers doped with OANI and oxidized with ammonium persulfate, are compared in Figure 4.4. The relative permittivities of undoped block copolymers with varying PAMPSA weight percent are shown in Figure 4.4A. Undoped copolymer 1 (23 wt% PAMPSA) has a high relative permittivity at low frequencies, but the permittivity falls sharply with increasing frequency. This curve shows significant polarization relaxation (permittivity decrease) at intermediate frequencies, indicating relaxation of Maxwell-Wagner interfacial polarization [5] associated with buildup of space charge at domain interfaces. The high polarization at low frequencies could be due to the high concentration of sulfonic acid protons from the PAMPSA block, which migrate and accumulate at internal domain boundaries. As the frequency of the applied field

increases, charge migration can't keep up with the oscillating electric field. For this reason relative permittivity (ε_r) decreases as frequency increases.

Copolymer 2 (13 wt% PAMPSA) and 3 (6 wt% of PAMPSA) show different behavior compared to copolymer 1. The relative permittivities of copolymers 2 and 3 are much lower than that of copolymer 1 at low frequency. The permittivities of copolymers 2 and 3 are nearly frequency independent below 200 kHz and 10 MHz, respectively. The results show the permittivity values decrease with PAMPSA content due to reduced numbers of proton available for polarization. However, the differing frequency dependence could be due to differences in copolymer polarizable domain size and morphology. With the decrease of PAMPSA content from 13 wt% to 6 wt%, PAMPSA domain sizes are anticipated to decrease accordingly. For smaller and isolated domains, one might expect polarization to be saturated across a wide frequency range, and thus relaxation of interfacial polarization is expected to move to higher frequency.

Figure 4.4B shows the frequency-dependent relative permittivity of PAMPSA-b-PMA copolymers doped with OANI, oxidized with ammonium persulfate, and then dialyzed to remove salts. Among all the copolymers, copolymer 1 containing highest PAMPSA content (23 wt %) shows the greatest impact of OANI doping. The relative permittivity below 200 kHz for OANI-doped copolymer 1 (Figure 4.4B) is much lower than that of undoped copolymer 1, which is likely to be due to absence of sulfonic acid protons in the former. However, the impact of OANI doping on copolymer 2 and 3 is significantly different. Below 200 kHz, OANI doping decreases the permittivity of

copolymer 2 by 10-20% compared to the undoped state, while it increases the permittivity of copolymer 3 by 10-20%. These differences in results between undoped and OANI-doped copolymers could be combination of different factors, including the effects of sulfonic acid protons, conjugation, etc. All of the OANI-doped copolymers show higher relative permittivities than the corresponding undoped copolymers at frequencies above 500 kHz. This suggests that the OANI-doped PAMPSA domains are primarily responsible for the higher permittivity values at high frequencies.

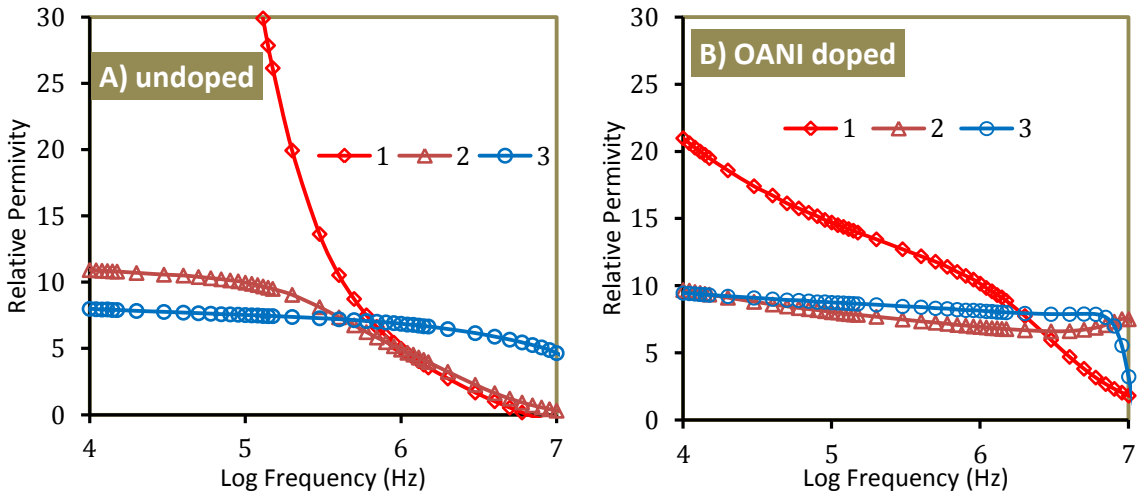

Figure 4.4. Relative permittivity versus frequency for (A) undoped PAMPSA-*b*-PMA block copolymers and (B) OANI-doped PAMPSA-b-PMA block copolymers after the removal of salts. Label 1, 2, 3 denote PAMPSA-b-PMA copolymers containing 23, 13, and 6 wt % PAMPSA, respectively (Table 4.1).

The loss tangent values of undoped PAMPSA-*b*-PMA block copolymers (Figure 4.5A) increase significantly with increasing PAMPSA wt%. Copolymer 1 (containing 23 wt % PAMPSA) has loss tangent above 0.5 and increases with frequency, suggesting that this copolymer behaves more like a conductor than capacitor. This is more apparent in conductivity measurement of these materials shown in Figure 4.6A. In contrast, copolymer 2 has loss tangent below 0.2 up to 100 kHz, while copolymer 3 has loss

tangent below 0.2 up to 1.5 MHz. These materials behave more like capacitors at low frequencies, despite the polarization produced by ionic migration results in significant dielectric loss. The high dielectric losses at high frequencies may be due to the interaction of the PAMPSA anion with the applied electric field, which activates a molecular relaxation process resulting in increased loss tangent. The increase in loss tangent with increased PAMPSA content supports this hyposthesis.

The dielectric loss behavior of the OANI-doped copolymers (Figure 4.5B) is much different than that of the undoped copolymers. The loss tangent of OANI-doped copolymer 1 decreases significantly compared to that of the undoped copolymer 1 at all frequencies. Similarly, Above 100 kHz, OANI-doped copolymer 2 shows a dramatic decrease in loss tangent compared to undoped copolymer 2. Unlike the undoped materials, all OANI-doped copolymers behave like capacitors at frequencies up to 1 MHz. These results are likely explained by the absence of sulfonic acid protons in the OANI-doped materials. The conductivity data of the OANI-doped copolymers (Figure 4.6B) provide additional support to this explanation. OANI-doping significantly reduces the conductivities of copolymers 1 and 2 compared to the respective undoped copolymers for frequencies greater than 100 kHz. The difference in the loss tangents for undoped and OANI-doped copolymer 3 is negligible, probably due to low content of PAMPSA (6 wt%) and OANI. Overall, the significant changes in permittivity and loss behavior between undoped and OANI-doped copolymers 1 and 2 suggest presence of isolated, conjugated domains in the OANI-doped copolymers. These domains may result in different polarization and loss mechanisms that dominate at high frequencies.

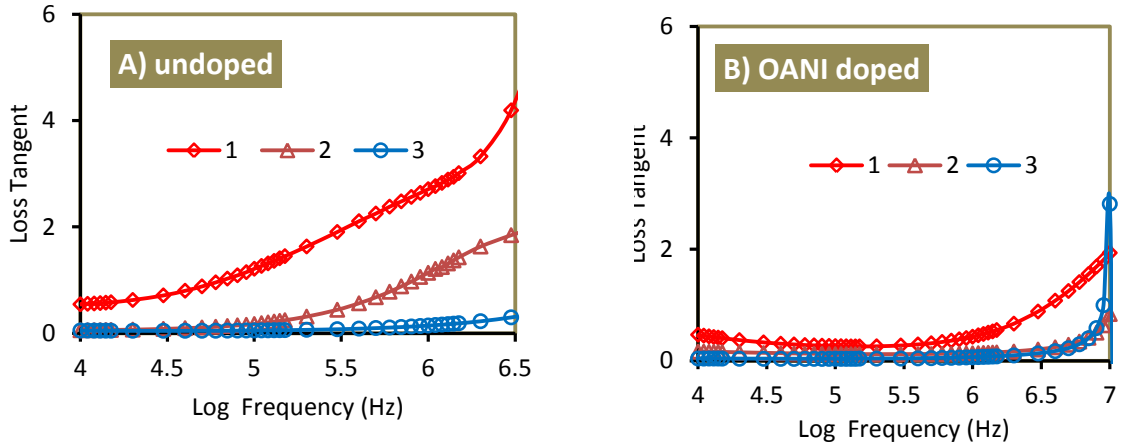

Figure 4.5. Loss tangent (dielectric loss) versus frequency for (A) undoped PAMPSA-*b*-PMA block copolymers and (B) OANI-doped PAMPSA-*b*-PMA block copolymers after the removal of salts. Labels as in Figure 4.4

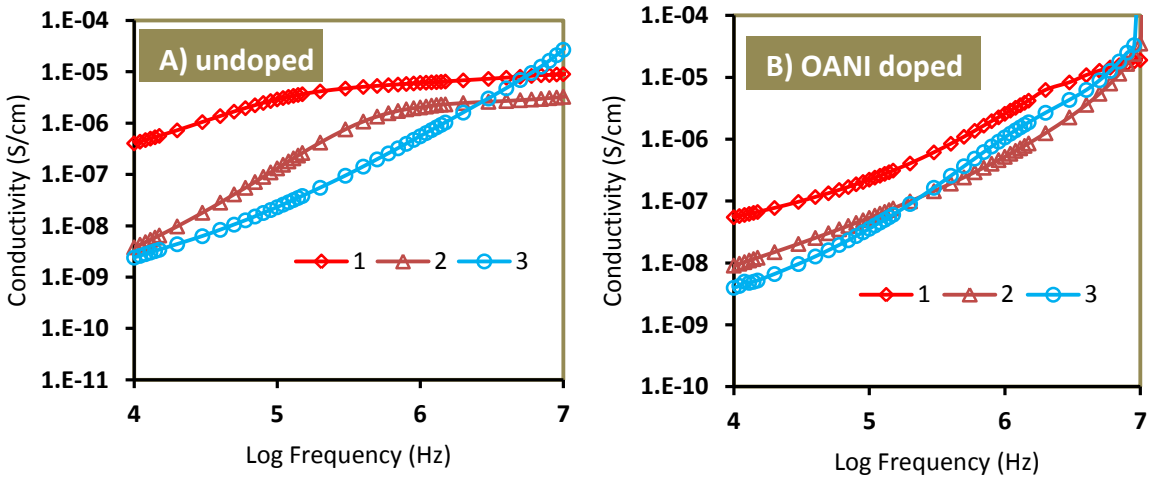

Figure 4.6. Conductivity versus frequency for (A) undoped PAMPSA-*b*-PMA block copolymers and (B) OANI-doped PAMPSA-*b*-PMA block copolymers after the removal of salts. Labels as in Figure 4.4

4.2.4. Conclusions

Oligoaniline-doped supramolecular block copolymers exhibited higher permittivity and much lower dielectric loss compared to undoped block copolymers, suggesting dominant polarization of the microphase domains. However, this approach is limited, as the sulfonic acid on the side chain of the block copolymer is the only possible

dopant for the oligoaniline. Unfortunately, these all the block copolymers manifest dielectric loss (loss tangent) greater than 5%, which is unacceptable for dielectric energy storage applications.

4.3. POLYSTYRENE END-CAPPED WITH OLIGOANILINE BLOCKS[4]

4.3.1. POLYMER ARCHITECTURE

This may be a low cost approach to enhance the dielectric permittivity of commodity polymers, which has not previously been considered as a way to produce high performance dielectric capacitor materials. In this approach, the ends of polystyrene chains are capped with oligoaniline through the click reaction between azide-terminated polystyrene and alkyne-containing aniline trimer (Figure 4.7). The oligoaniline is then doped with various acids, including hydrochloric acid (HCl) and large organic acids such as dodecylbenzenesulfonic acid (DBSA) and camphorsulfonic acid (CSA). Because of chemical incompatibility, we expect that highly polar oligoaniline (OANI) will self-assemble into nanoscale domains dispersed in a nonpolar polystyrene matrix (Figure 4.8). Polystyrene (PS), in this system, serves as an insulating block, whereas OANI serves as a conducting block. In principle, delocalization of electrons across the π-network of OANI can produce high interfacial polarization upon charge displacement, resulting in large dielectric response. By controlling the molecular weight of PS, the end-capped polymers can be induced to form nanoscale OANI-rich domains embedded in an insulating matrix. Details of synthesis and polymer characterization are

described in our published work [51]. All OANI end-capped PS materials were synthesis and characterized (GPC, ^{1}HNMR,FT-IR, UV/vis) by Dr. Christopher Hardy [51, 95].

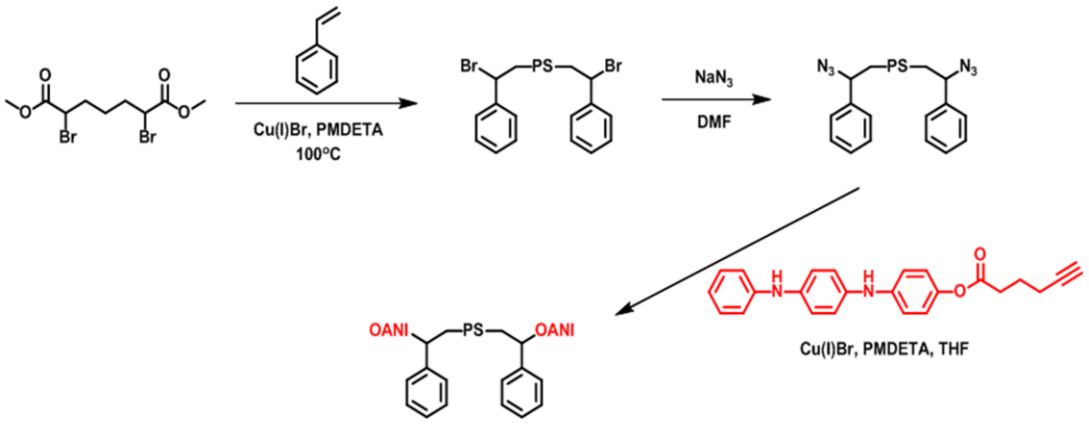

Molecular Weight of PS: 6,000 g/mol, and 30,000 g/mol

Figure 4.7. Synthesis of oligoaniline capped polystyrene through the click reaction [51].

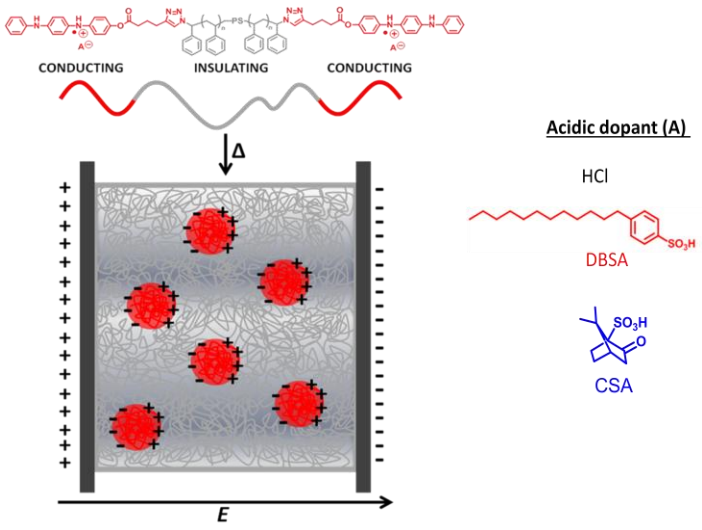

Figure 4.8. Microphase separation of oligoaniline end-functionalized polystyrene and its contribution to increasing dielectric permittivity. Image courtesy of Dr. Christopher Hardy [51].

Table 4.2. OANI weight (%) in different acid doped OANI-ended polystyrene (PS) for two different PS molecular weight (MW) [51].

Materials	Wt (%) OANI/acid in PS MW 30,000 (g/mol)	Wt (%) OANI/acid in PS MW 6,000 (g/mol)
Br-PS-Br	0	0
OANI-PS-OANI	1.81	7.94
OANI-PS-OANI doped HCl	1.93	8.41
OANI-PS-OANI doped DBSA	2.84	12.02
OANI-PS-OANI doped CSA	2.56	10.91

4.3.2. Film Preparation and Dielectric Characterization

Films for dielectric characterization and hysteresis measurements were prepared by dissolving polymer samples in toluene (67 mg/mL) and casting in heavy-gauge aluminum pans. The solvent was removed by evaporation at 65 °C under slightly reduced pressure (635 mmHg absolute) for 24 h, producing films with uniform thickness without solvent bubbles, cracks, or other defects. Film thicknesses were measured at multiple positions with a micrometer; measured thicknesses ranged from 2 to 25 μm. Strips of aluminum pan bearing copolymer films were cut using scissors; the aluminum pan served as the bottom electrode for dielectric measurements. Circular gold electrodes (area 1.13 cm^2) were deposited on the films top surfaces by sputter coating in an argon atmosphere through a shadow mask.

Impedance spectroscopy was used to measure the low-field dielectric properties (complex permittivity and conductivity). Polarization testing was used to measure displacement-field (D-E) loops. The details of these measurements and the analysis of the data are described in Chapter 2 (Section 2.2).

4.3.3. Dielectric Properties: Results and Discussion

Figure 4.9 shows the frequency-dependent dielectric properties of bromine terminated polystyrene, polystyrene end functionalized with oligoaniline, and oligoaniline doped with various acids. For bromine terminated polystyrene (molecular weight 30,000 g/mol), relative permittivity is 2.7 (Figure 4.9A) and is nearly independent of frequency. Upon converting the end group from Br to OANI, the permittivity increases to 3.5. HCl doping with OANI shows slight permittivity enhancement: the ε_r value is 4.1 and constant all over measured the frequency range. Permittivity enhancement is significant with BDSA and CSA doping. BDSA doped polymer shows highest ε_r value of 9 at 1 kHz, which decreases over the measured frequency to 6 at 1 MHz. CSA doped polymer shows permittivity values decreasing from 12 to 8.8 over the same frequency range.

Similar trends are also observed for lower molecular weight (6,000 g/mol) oligoaniline capped PS polymers, but permittivity enhancement is larger (Figure 4.9A'). Oligoaniline doping with various acids has significant impact on relative permittivity. The HCl-doped polymer shows a permittivity value around 8 independent of frequency. The Permittivity value for DBSA doped polymers is 20 at 1 KHz, decreasing as frequency

increases to 13.3 at 1 MHz. The highest enhancement of permittivity is observed for CSA-doped polymer: the ε_r values vary from 24.2 to 22.6. This greater enhancement of permittivity in lower molecular weight OANI-PS-OANI is due to their higher fraction of aniline content (Table 4.2) amplified by the high concentration of protons from the acidic dopant that migrate and accumulate at internal domain boundaries.

The loss tangents of all the polymers are shown in Figure 4.9 B and B'; the tan δ values remain below 0.6 over the frequency range 1 KHz – 1 MHz. Higher molecular weight (Figure 4.9B) PS-OANI doped with CSA and DBSA show loss tangent values of 0.6 and 0.38, respectively at 1 KHz. The loss tangent decreases significantly as frequencies increases. The high loss tangents at low frequencies and the frequency dependence indicate ionic species migration to the interface is the dominant polarization mechanism. For lower molecular weight polymers (Figure 4.9B'), except for PS-OANI doped with CSA at lower frequency, all polymers show loss tangent well below 0.1. These values of loss tangents are substantially lower than previously reported oligoaniline-containing ferroelectric copolymers [96-99].

Yang *et al.* suggests that organic acids produce more charge transfer between the dopant and the oligoaniline [100], allowing more electron transfer, and ultimately enhanced conductivity. Figure 4.9 C and C' show that polymers containing oligoaniline unit doped with large acids (DBSA and CSA) manifest higher levels of conductivity than the OANI-PS-OANI doped with the small acid HCl.

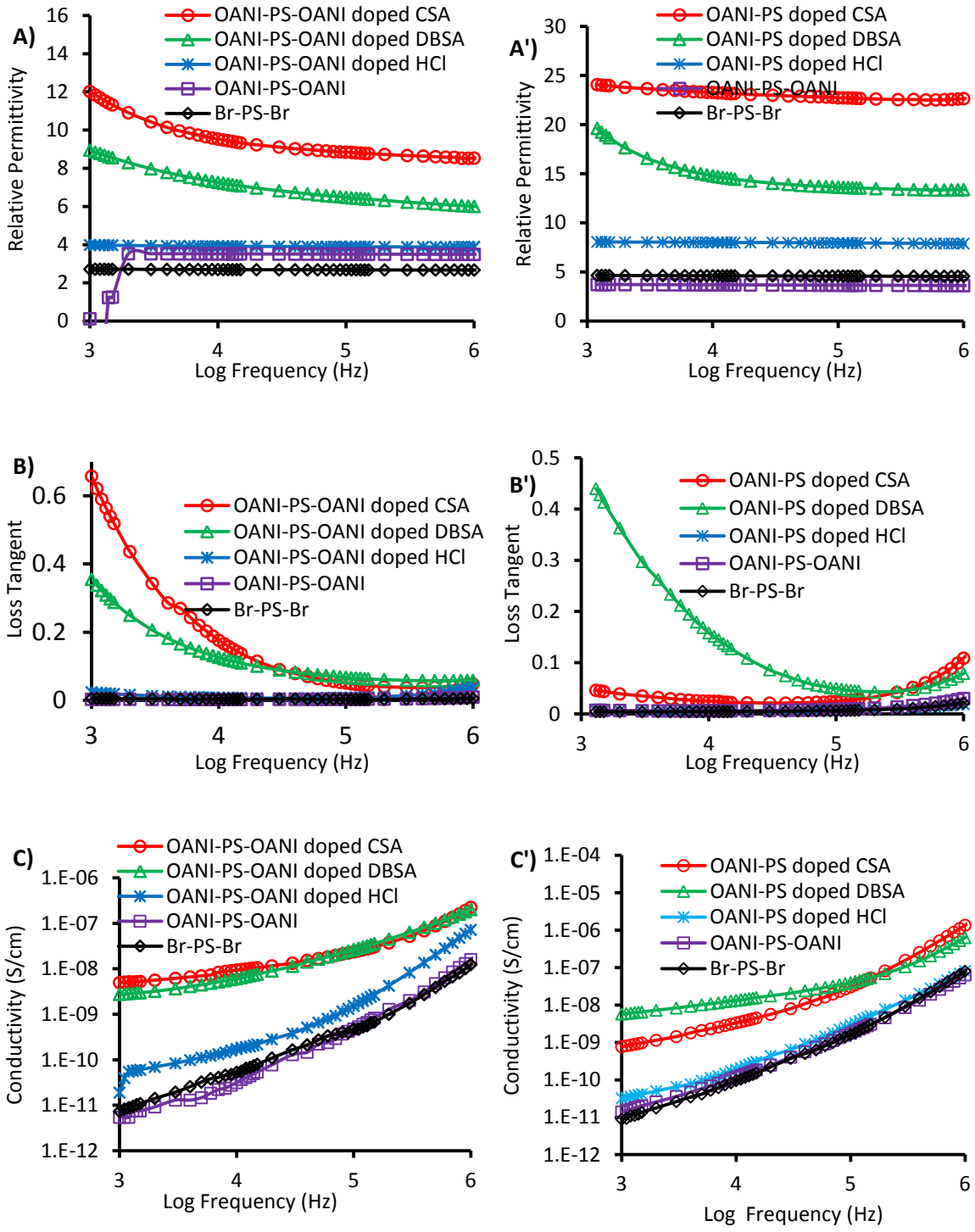

Figure 4.9. Effect of acid doping on frequency dependent relative permitivity A) and A'), loss tangent B) and B') and conductivity C)and C') for 30,000 (g/mol) and 6,000 (g/mol) molecular weights, respectively.

Polarization measurements at low to moderate field are shown in Figure 4.10. PS homopolymer shows linear polarization behavior, as expected. All of the acid doped OANI-capped PS polymers show significantly higher polarization than PS homopolymer.

From the polarization (D-E) loops in Figure 4.10, we may calculate stored energy densities values according to equation (1.3). The stored energy density of acid-doped OANI-capped PS, relative to that of pure PS homopolymer measured at the same electrical field, is shown in Figure 4.11. The higher molecular weight polymers (Table 4.2) containing 2-3% OANI have stored energy densities 4-8 times higher than that of pure PS homopolymer. For lower molecular weight polymers doped with CSA and DBSA, and having 11-12% OANI, the relative energy density increased up to 10-12 times that of PS. However, lower molecular weight polymer doped with HCl has different characteristics. It shows decreased stored energy density relative to higher molecular weight PS, although its energy density is still twice as large as the energy density stored in pure PS homopolymer at the same applied field. This trend is apparent in Figure 4.10A.

The significant enhancement of permittivity of OANI-capped PS could be explained by the presence of OANI-rich domains dispersed in the PS matrix. The formation of these nanoscale domains would significantly enhance the interfacial area of highly polarizable nanodipoles. This hypothesis could be further supported by the higher permittivity of low molecular weight PS than that of higher molecular weight PS when doped with same reagents, as the weight fraction of OANI plus dopant in the

lower molecular weight PS is in the range of 8-12 wt%, which is sufficient to have nanoscale phase-separation between chain ends and PS matrix. However, this phase-separation would be much less prominent in high molecular weight PS as the weight fraction of OANI plus dopant is only around 2 wt%, which would lead to total disorganized systems. To support this hypothesis, [5]SAXS was performed on various acid-doped OANI-capped PS polymers with two different molecular weight of PS. For the high molecular weight polymers, no ordered peaks were observed, as shown in Figure 4.12 A. Given that higher molecular weight polymers (30,000 g/mol) have only 2 wt% oligoaniline/acid dopant, these polymers probably formed highly homogeneous systems. However, for the low molecular weight polymers (6,000 g/mol), a weak correlation peak at the 5 nm length scale ($d = 2\pi/q$) was observed (Figure 4.12B). Since there were no additional higher order peaks present, these polymers did not form well-ordered nanodomains of oligoaniline/acid dopant complex, but rather disordered domains with rough interfaces between them and polystyrene matrix. Nevertheless, these highly polarizable nanodomains led to significant enhancements in dielectric permittivity.

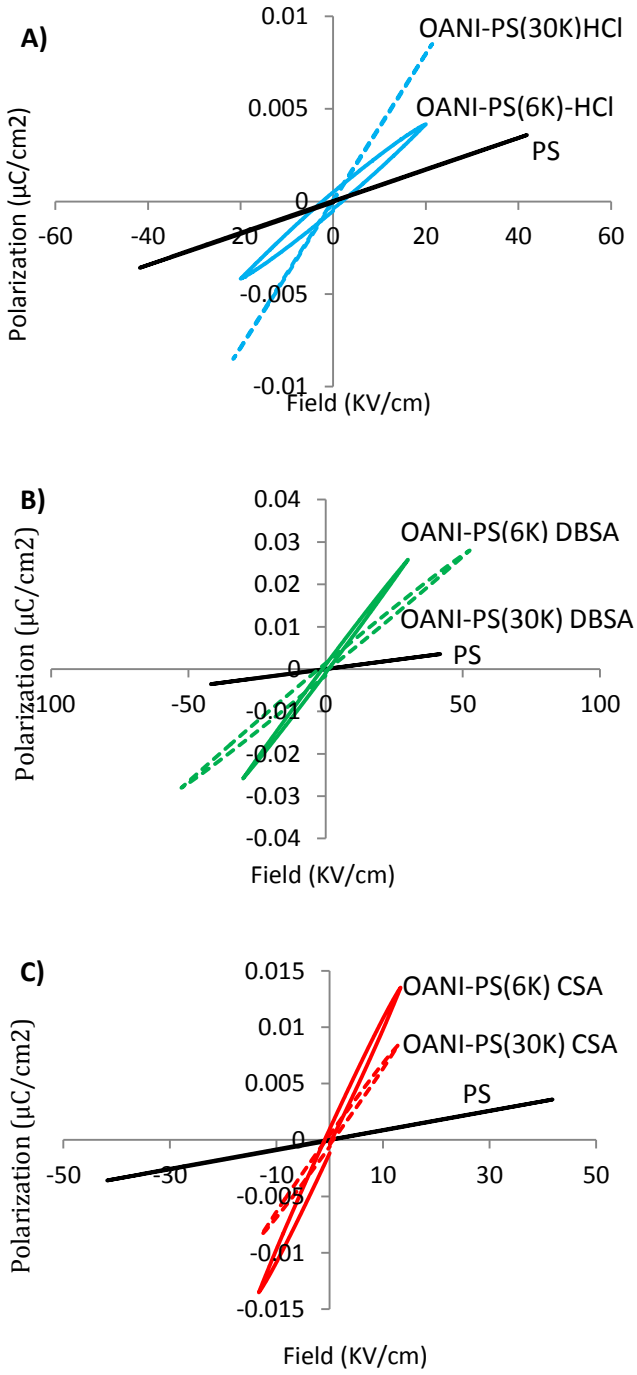

Figure 4.10. Polarization versus applied electric field for PS and OANI-capped PS dopped with (A) HCl, (B) DBSA, and (C) CSA. Measurments are carried out at 100 Hz cycle frequency. Solid line denotes PS molecular weight 6,000 g/mol; dotted line denotes PS molecular weight 30,000 g/mol.

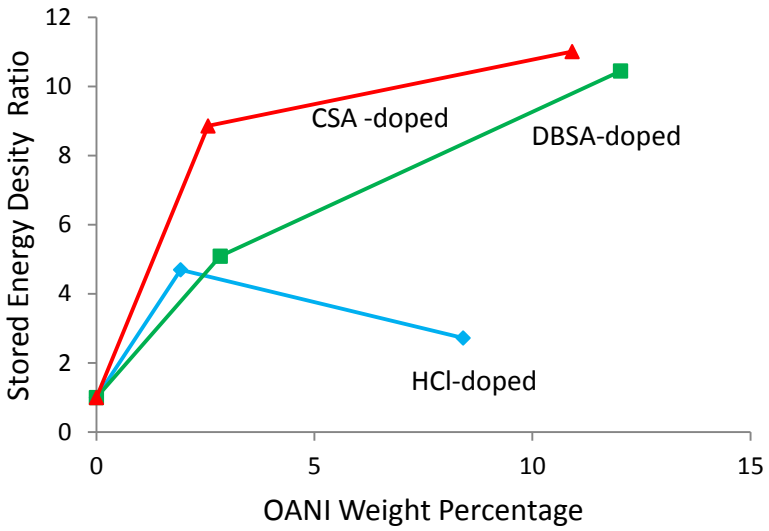

Figure 4.11. Stored energy density ratio $(\widehat{W}_{OANI-PS}/\widehat{W}_{ps})$ measured at the same applied field strength and frequency. All the measurements were carried out at 100 Hz frequency, and energy density was determined at 12.9 kV/cm field strength.

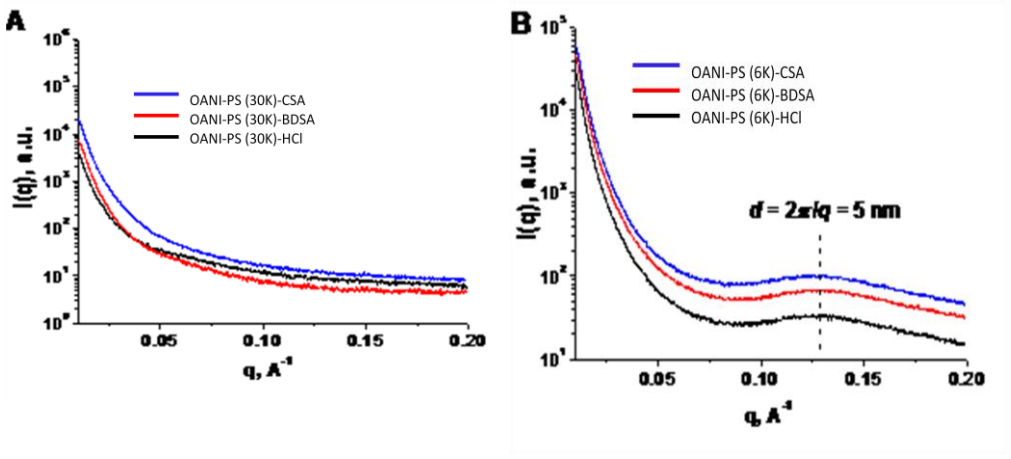

Figure 4.12. SAXS plots for PS and OANI-capped PS dopped with HCl, DBSA, and CSA A) for PS molecular weight 30,000 g/mol, B) for PS molecular weight 6,000 g/mol [51].

4.3.4. CONCLUSIONS

The formation of nano-scale domains leading to significant enhancement of interfacial area gives the dielectric properties of OANI-capped PS doped with large

organic acids an order of magnitude increase in permittivity and energy storage capacity relative to pure polystyrene, while maintaining a relatively low dielectric loss, especially in the high frequency range. This simple and novel strategy could be utilized to improve dielectric properties of many other commodity polymers.

4.4. TERTHIOPHENE-CONTAINING METHACRYLATE POLYMERS[6]

4.4.1. POLYMER ARCHITECTURE

This section describes the investigation of terthiophene-containing polymers as high performance nanodielectric materials with high permittivity and low dielectric loss across wide frequency range (100 Hz-4 MHz). Specifically, methacrylate polymers carrying terthiophene oligomers as side chains have been designed. The first step (Figure 4.13) is the synthesis of the monomer terthiophene ethyl methacrylate (TTEMA). RAFT polymerization of this monomer produces poly (terthiophene ethyl methacrylate), abbreviated henceforth as PTTEMA.

The hypothesis of this work is that we expect the terthiophene side chain to self-organize to form nanoscale, conjugated, electrically conductive domains dispersed in an insulating polymer matrix consisting of the methacrylate polymer main chain (Figure 4.14). Although we do not yet have full information on nanostructures in these polymers, the dielectric properties are consistent with what one might expect for nanodielectric materials with high energy storage dominated by electronic conduction and interfacial polarization. Two different molecular weight homopolymers (Table 4.3)

were synthesized and their dielectric properties and energy storage performance were characterized and compared. Details of the synthesis and characterization of this these polymers are described in our published work [54]. All synthesis and polymer characterization measurements were performed by Dr. Yali Qiao [54].

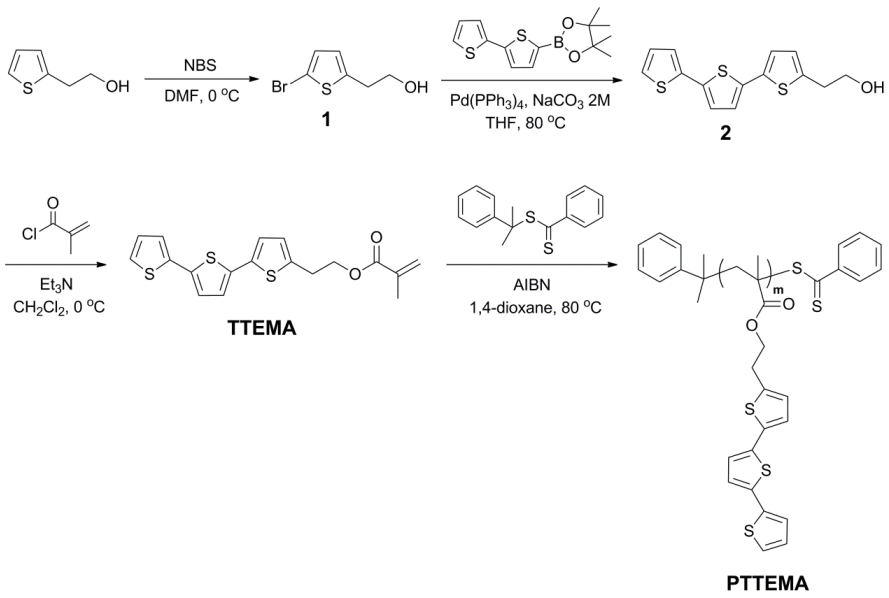

Figure 4.13. Synthesis of terthiophene ethyl methacrylate (TTEMA) and its polymer (PTTEMA) by RAFT [54].

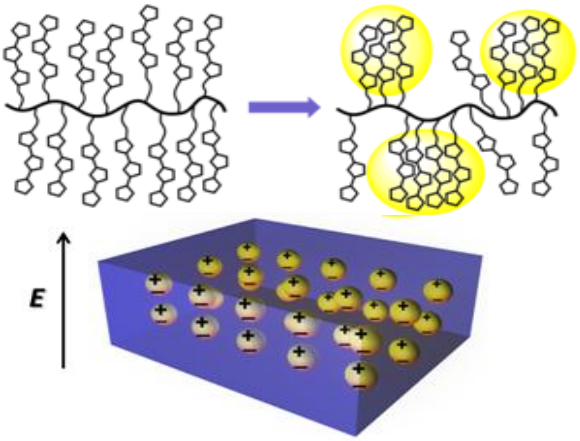

Figure 4.14. Illustration of the hyposthetical nonoscale structure of PTTEMA and its polarization under an applied eletric field. Image courtesy Dr. Yali Qiao [54].

Table 4.3. Molecular weight information and thermal properties for two PTTEMA homopolymers [54].

Polymer	DP	M_n (g/mol)	M_n (g/ mol)	PDI	$T_{recryst}$ (^oC)	$-\Delta H_c$ (J/g)	$T_{m.p.}$ (^oC)	$-\Delta H_m$ (J/g)
$PTTEMA_{61}$	61	22,300	10,300	1.28	111.2	17.6	137.3	15.0
$PTTEMA_{180}$	80	64,900	27,100	1.29	117.7	18.0	142.5	18.6

4.4.2. Film Preparation and Dielectric Characterization

Films for dielectric characterization were prepared by dissolving polymer samples in chloroform (34 mg/mL) and casting in heavy-gauge aluminum pans. The solvent was removed by evaporation at 70°C under reduced pressure (635 mm Hg absolute) for 24 h without any post-treatment (thermal annealing). Such procedures resulted in films with uniform thickness and free of bubbles, cracks, or other defects. Film thicknesses were measured at multiple positions with a micrometer, in the range of 3-20 µm. Strips of aluminum pan bearing homopolymer films were cut using scissors; the aluminum pan served as the bottom electrode for dielectric measurements. Gold was sputter-coated under argon atmosphere through a shadow mask to deposit circular gold electrodes (area 1.13 cm^2) on the films' surfaces. The films' complex impedance was measured at varying frequency (typically 100 Hz to 1.2 MHz) using an impedance analyzer as described in chapter (section 2.2.1). Measurements were carried out on 3-5 specimens of each sample to ensure reproducibility. Polarization testing was used to

measure displacement-field (D-E) loops. The details of these measurements and data analysis are described in Chapter 2 (Section 2.2.2)

4.4.3. Results and Discussion

4.4.3.1. Polymer Physical Characterization

Some key characterization experiments were performed by our chemistry collaborators that will provide evidence of nanoscale domain formation in PTTEMA homopolymers. Differential scanning calorimetry (DSC) and wide angle X-ray diffraction (WXRD) measurements were performed to acquire information about microstructure in PTTEMA polymers.

These experiments were carried out primarily by Dr. Yali Qiao. Experimental details may be found in our publication [54]. DSC curves (Figure 4.15) show clear melting and crystallization processes for both PTTEMA homopolymers. The crystallization temperature of PTTEMA increased with molecular weight, from 111.2°C for $PTTEMA_{61}$ to 117.7°C for $PTTEMA_{180}$ (Table 4.3). Melting temperatures showed a similar trend with varying molecular weight. These results suggest that terthiophene side chains might interact to form crystalline domains in presence of amorphous methacrylate polymer backbones. The ΔH_m value of $PTTEMA_{180}$ (18.58 J/g) is larger than that of $PTTEMA_{61}$ (15.04 J/g), which indicates the degree of crystallinity of PTTEMA with higher molecuar weight should be higher than that with lower molecuar weight.

WXRD profiles (Figure 4.16) show similar patterns for both the homopolymers: a relatively strong peak at 19° (2θ) with two higher order peaks located at 26° and 41°.

The asymmetry and rather sharp main peak suggests it is not a solely an amorphous halo, but rather diffraction from a mixture of amorphous and crystalline structures. Further deconvolution of WXRD profiles [54] indicates four peaks: the sharpest peak probably originates from crystalline domains, and other three peaks are associated with amorphous polymethacrylate. The crystalline domain sizes are estimated from Scherrer's formula equation (2.1) [55, 56]. The calculated crystal sizes are 1.82 nm and 1.46 nm for $PTTEMA_{61}$ and $PTTEMA_{180,}$ respectively. Such small crystalline domains are in sharp contrast with conventional semi-crystalline polymers. The reason for the formation of such remarkably small crystalline domains could be due to partial crystal formation from terthiophene segments in amorphous PMA matrix. Because the pendant terthiophene groups were attached separately onto the polymer backbone, the size of the crystallites was suppressed by the limited accessibility of the adjacent terthiophene segments [101].

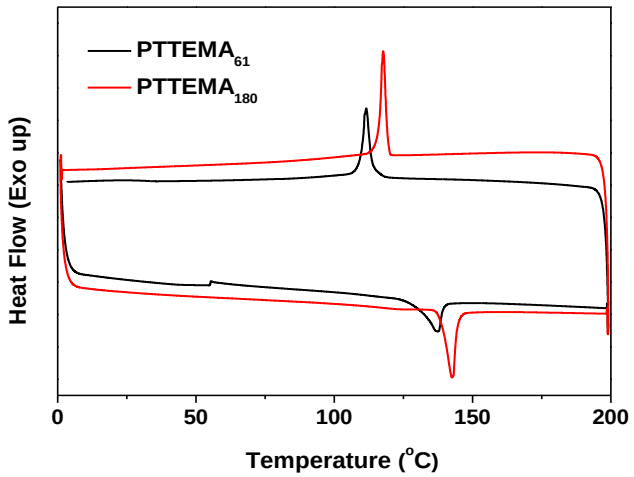

Figure 4.15. DSC profiles of terthiophene-containing PTTEMA polymers (second heating and cooling cycle).

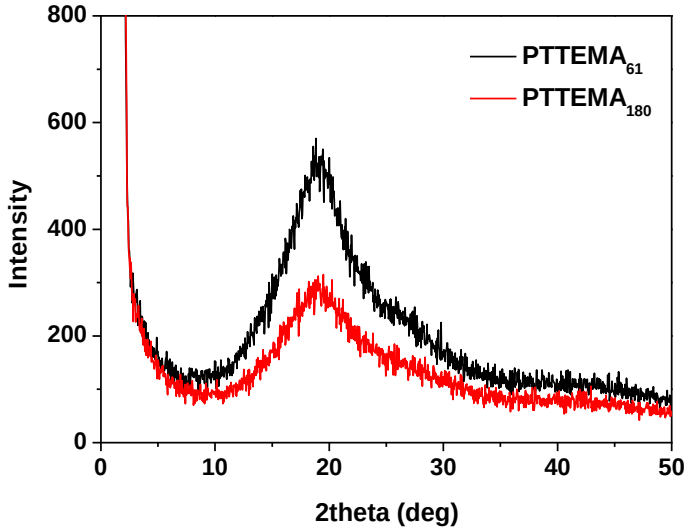

Figure 4.16. WXRD patterns of terthiophene-containing PTTEMA polymers.

4.4.3.2. DIELECTRIC PROPERTY CHARACTERIZATION

Figure 4.17A shows the frequency-dependent relative permittivity of PTTEMA homopolymers. The relative permittivity of the lower molecular weight $PTTEMA_{61}$ was higher than that of $PTTEMA_{180}$. $PTTEMA_{61}$ has relative permittivity ranging from 11.4 to 10.2 (as frequency decreases), while $PTTEMA_{180}$ has relative permittivity ranging from 9.3 to 8.2. Both polymers show ε_r values that are almost constant over a broad frequency range (1 kHz to 1 MHz), which is remarkable compared to widely used PVDF homopolymer and copolymers. One might expect the smaller crystal size and slightly higher degree of crystallinity ($-\Delta H_c$,Table 4.3) in $PTTEMA_{180}$ would result in higher relative permittivity. However, $PTTEMA_{61}$ has higher conductivity compared to $PTTEMA_{180}$ (Figure 4.17C). Consequently, despite small difference in the degree of

crystallinity and crystal size for the two polymers, the discrepancy in conductivity has an obvious effect on the dielectric response in terthiophene containing polymers.

The loss tangent curves for both PTTEMA homopolymers are shown in Figure 4.17B. For both polymers, the loss tangent values are below 0.02. Such a low dielectric loss over wide frequency range with this high relative permittivity is striking, suggesting very fast dipole relaxation in PTTEMA's small crystalline domains.

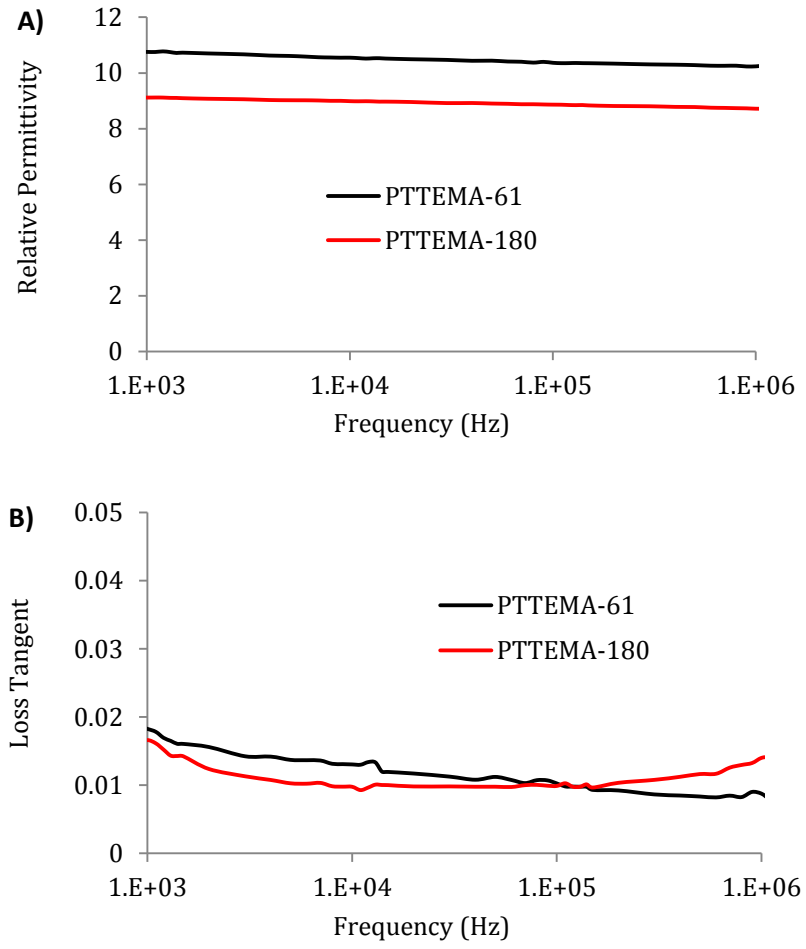

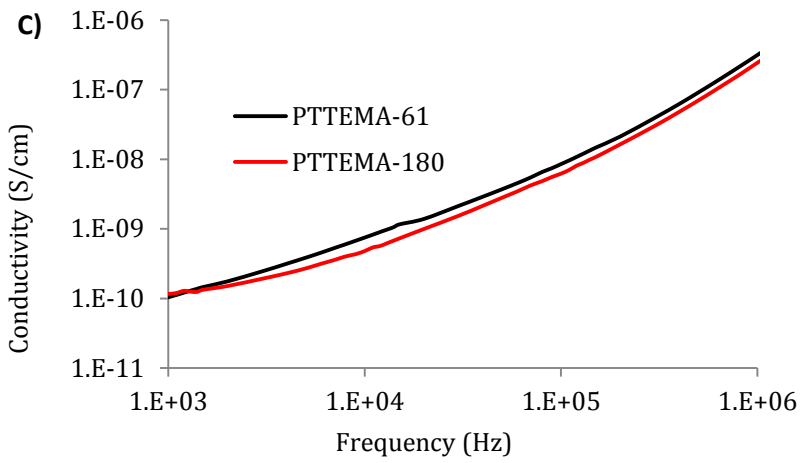

Figure 4.17. Frequency dependent relative permittivity A), loss tangent B), and conductivity C) for therthiophene–containing PTTEMA polymers.

Polarization response and energy storage performance were characterized by our Penn State collaborators and published in our paper [54]. Figure 4.18 shows typical D-E loops for terthiophene-containing PTTEMA homopolymers. Both homopolymers ($PTTEMA_{61}$ and $PTTEMA_{180}$) show nearly linear electric displacement with applied field, which resembles the response of polymers such as BOPP and PE [8, 11, 54]. Compared with $PTTEMA_{180}$, the lower molecular $PTTEMA_{61}$ shows higher displacement at the same applied field: displacement is 0.013 C/m^2 for $PTTEMA_{61}$ and 0.012C/m^2 for $PTTEMA_{180}$ at 150MV/m, which is consistent with relative permittivity results. The highest attainable electric displacement for $PTTEMA_{61}$ is 0.013 C/m^2 and 0.016 C/m^2 for $PTTEMA_{180}$ at 150MV/m. Both displacements are significantly higher than values for commercial BOPP capacitors under same applied field (less than 0.005C/m^2 at 200 MV/m) [8, 9].

Calculated stored energy densities from equation (1.3) are shown in Figure 4.19. Stored energy density shows the similar behavior: the lower molecular weight $PTTEMA_{61}$ homopolymer has larger energy density values compared to the higher molecular

weight $PTTEMA_{180}$ at the same applied field. However, higher molecular weight polymer is able to withstand higher applied fields. Thus $PTTEMA_{180}$ exhibits higher energy storage capacity compared to $PTTEMA_{61}$. $PTTEMA_{180}$, for example, reaches stored energy density of 1.56 J/cm^3, which is much higher than most homopolymers at the same applied field. Notably, this increase in stored energy density for $PTTEMA_{180}$ homopolymer is not accompanied by higher dielectric loss.

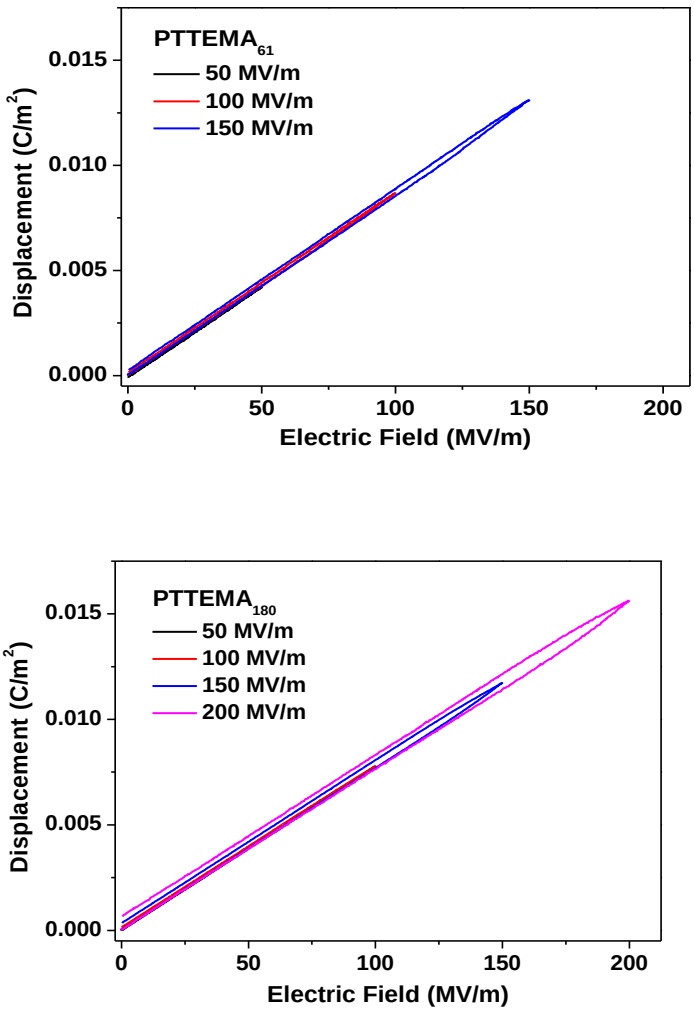

Figure 4.18. Unipolar electric displacement – electric field (D-E) loops for terthiophene-containing PTTEMA polymers as measured by Kuo Han, and Qing Wang at Pennsylvania State University; reproduced from reference [54].

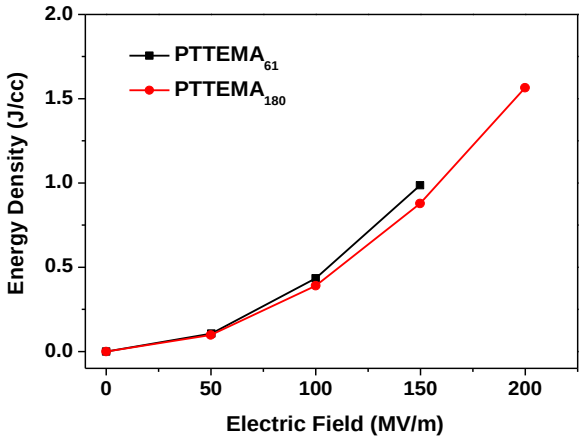

Figure 4.19. Stored energy density as a function of applied field for terthiophene-containing PTTEMA polymers. Values determined from integration of D-E data, calculated by Kuo Han, and Qing Wang at Pennsylvania State University; reproduced from reference [54].

4.4.4. CONCLUSIONS

Π-conjugated terthiphene-containing polymers exhibit high relative permittivity (comparable to PVDF) with very low dielectric loss. The nanoscale crystalline domains (<2nm) facilitate nearly linear charge and discharge cycles as seen in the measured D-E loops. Lower molecular weight homopolymer ($PTTEMA_{61}$) shows higher energy storage capacity compared to higher molecular weight polymer ($PTTEMA_{180}$) at the same applied field. However, because of its higher breakdown strength, $PTTEMA_{180}$ exhibits higher overall energy storage performance, 1.56 J/cm^3 at 200MV/m, higher than most homopolymers at the same applied field. This is a novel homopolymer is thus promising for energy storage applications; tuning crystal size, percentage crystallinity, and molecular weight might offer superior performance.

4.5 TERTHIOPHENE-CONTAINING COPOLYMERS AND HOMOPOLYMER BLENDS

4.5.1. INTRODUCTION

After discovering that PTTEMA homopolymer [54] can serve as a high performance dielectric material ($\varepsilon_r > 10$, and $\tan \delta < 0.02$), a significant effort has been made to decipher the polarization mechanisms responsible for these properties. Several critical questions should be answered before we carry out further material development. First, which aspect dominates dielectric performance: nanoscale crystalline domains (<2nm), or just the presence of terthiophene in the polymer architecture? Second, is there any advantage of the block copolymer architecture of PTTEMA-b-PS compared to simple blends of PTTEMA and PS homopolymers? To answer these questions, the dielectric properties of PTTEMA-b-PS and PTTEMA/PS blends with varying PTTEMA wt % have been prepared and characterized using low voltage impedance spectroscopy and high voltage polarization measurements.

PTTEMA homopolymer and block copolymers (PTTEMA-b-PS) were prepared by RAFT polymerization (Figure 4.20). The PTTEMA contents in these block copolymers were varied by changing PS block size (Table 4.4). All PTTEMA homopolymers and PTTEMA-b-PS copolymers were synthesis by Dr. Yali Qiao. Dr. Qiao also carried out polymer physical characterizations. PS homopolymer obtained from Sigma-Aldrich, USA. The PTTEMA/PS homopolymer (Table 4.5) blends were prepared by solution blending in THF as described below.

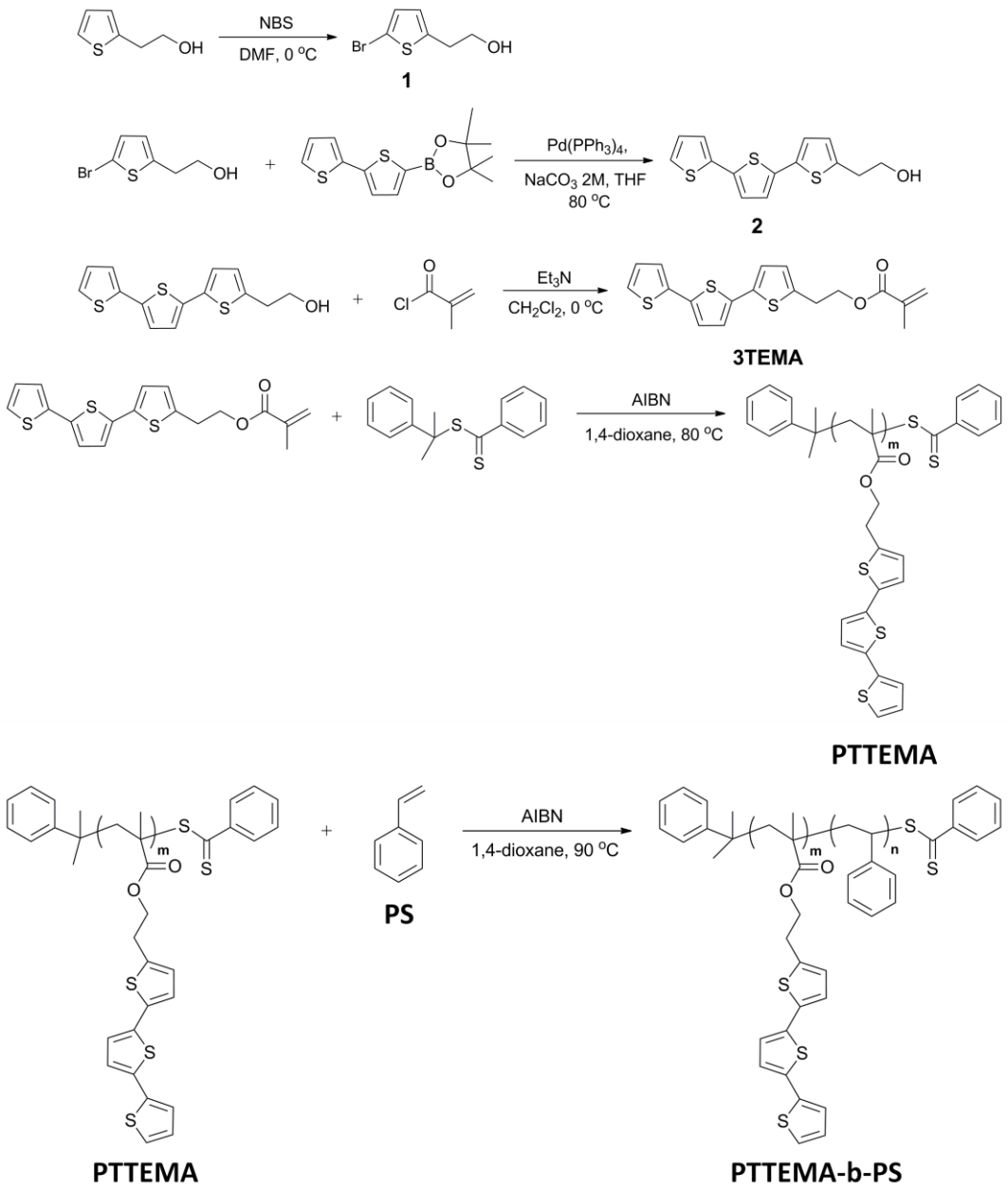

Figure 4.20. Synthesis of monomer TTEMA and its RAFT polymerization to produce block copolymer P3TEMA-*b*-PS (courtesy of Dr. Yali Qiao).

Table 4.4. Molecular weight information for PTTEMA-b-PS block copolymers.

Polymer	PTTEMA M_n, (DP) (g/mol)	PS M_n, (DP) (g/mol)	PDI (GPC)	TTEMA wt%
$PTTEMA_{58}$-PS_{901}	20,900 (58)	93,700 (901)	1.22	18
$PTTEMA_{58}$-PS_{304}	20,900 (58)	31,600 (304)	1.29	40
$PTTEMA_{58}$-PS_{136}	20,900 (58)	14,100 (136)	1.28	60

Table 4.5. Molecular weight information's of homopolymers for TTEMA wt % target in blends.

Polymer	PTTEMA M_n, (DP) (g/mol)	PDI (GPC)
$PTTEMA_{58}$	20900 (58)	1.18
PS	192,000 (**)	**

4.5.2. FILM PREPARATION

Films for dielectric property and polarization measurements were prepared by solution blending using THF. PTTEMA homopolymer and PTTEMA-b-PS copolymers were dissolved in THF (10 mg/ mL) and sonicated for 2-3 hours. Polymer blend samples were prepared in two steps. First, a measured amount of PS (depend on the wt % target) was added to THF (10 ml generally) and sonicated for 3-4 hours until completely dissolved. Second, a desire amount of PTTEMA homopolymer (again depending on wt % target)

was added to the solution and sonicated another 2-3 hours. For all the samples, the resultant solutions were poured into heavy-gauge aluminum pans. The THF was removed by evaporation at 44°C under reduced pressure (635 mm Hg absolute) for about 3 h without any post-treatment (thermal annealing). This resulted in films with uniform thickness and free of bubbles, cracks, or other defects. Film thicknesses were measured at multiple positions with a micrometer and had thickness in the range of 3-15 µm. Strips of aluminum pan bearing polymer or composite films were cut using scissors. The aluminum pan served as the bottom electrode for dielectric measurements. Gold was sputter-coated under argon atmosphere through a shadow mask to deposit circular gold electrodes (area 1.13 cm^2) on the films' top surfaces. Most of the polymer blend films spontaneously piled off the Al pan; in those cases gold electrodes were sputtered on both sides of the free standing films. We haven't observed significant variations in dielectric properties due to different electrodes.

The complex impedance of polymer and composite film samples was measured using an impedance analyzer. Polarization measurements at higher applied voltages employed a polarization tester. The details of the dielectric properties measurements and data analysis are described in chapter 2.

4.5.3. Results and Discussions

4.5.3.1 Physical Characterization

Differential scanning calorimetry (DSC) and wide angle X-ray diffraction (WXRD) measurements were performed to characterize the crystalline microstructure of the

block copolymers and polymer blends, aiming to understand the effect of PTTEMA wt (%) on the microstructure in both PTTEMA-b-PS copolymers and PTTEMA/PS blends.

Figure 4.21 shows DSC heating and cooling scan for PTTEMA homopolymer, PTTEMA-b-PS copolymers and PTTEMA/PS blends. For the copolymers (Figure 4.21a), the heating scans all show an exothermic peak at about 135 - 137°C due to crystallite melting. The T_{mc} values decrease slightly with decreasing PTTEMA wt%. Upon cooling, the PTTEMA homopolymer manifest a sharp exothermic peak at T_c =137.3°C due to crystallization of the terthiophene domains. The copolymers also have crystallization peaks at about the same T_c. This result suggests that the crystalline domains in PTTEMA-b-PS copolymers have similar single structure, independent of PTTEMA wt%. On the other hand, the enthalpy of crystallite melting ($-\Delta H_{cm}$) and crystallization (ΔH_c) clearly increase with PTTEMA content. This indicates that the amounts of crystalline domains in the copolymers are proportional to the PTTEMA wt % as seen Figure 4.22.

For the PTTEMA/PS blends (Figure 4.21b), the crystallite melting transitions in the blends occur earlier in heating scan (at lower temperatures) than that for PTTEMA homopolymer. Upon cooling, crystallization occurs later in the cooling scans (at lower temperatures) than in PTTEMA homopolymer. This may indicate that the size and structure of the crystallite domains in the blends vary with PTTEMA wt%. However, the enthalpies of crystallite melting and crystallization (Figure 4.22) are again proportional to wt% PTTEMA in the blends.

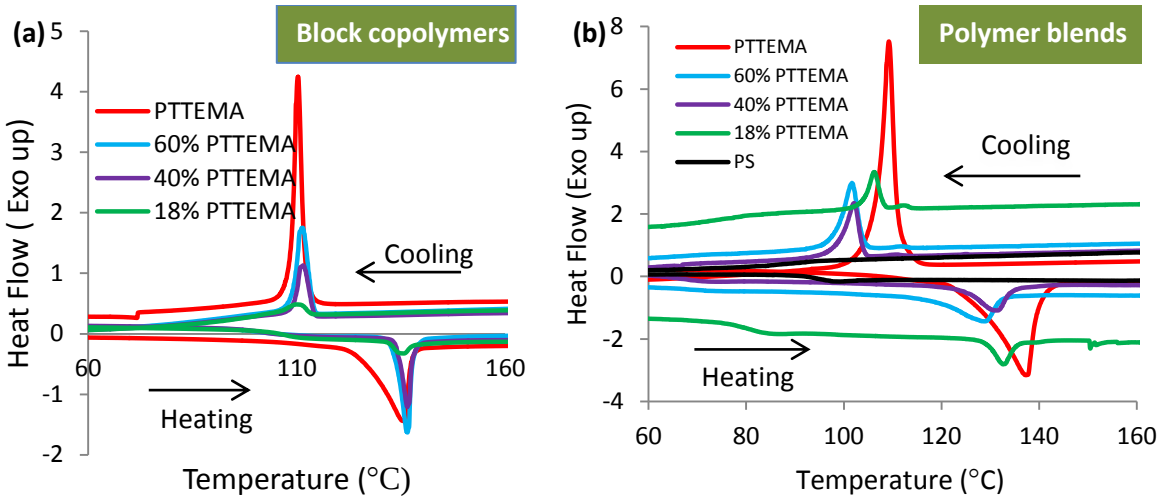

Figure 4.21. DSC curves for a) PTTEMA homopolymer and PTTEMA-b-PS block copolymers, and b) PTTEMA/PS polymer blends.

Table 4.6. Thermal properties of PTTEMA homopolymer, PTTEMA-b-PS copolymers, and PTTEMA/PS blends.

	Homo polymers and Block copolymers			
	T_m (°C)	$-\Delta H_m$ (J/g)	T_c (°C)	$-\Delta H_c$ (J/g)
PTTEMA	137.31	16.65	109.23	17.44
60% PTTEMA	136.53	7.91	111.4	7.996
40% PTTEMA	136.5	4.947	111.51	4.593
18% PTTEMA	135.28	1.276	109.6	1.952
	Polymer Blends			
60% PTTEMA	128.72	8.288	101.67	9.702
40% PTTEMA	131.17	4.34	102.11	5.204
18% PTTEMA	132.6	1.875	106.2	2.183
PS	98.02	N.a.	89.43	N.a.

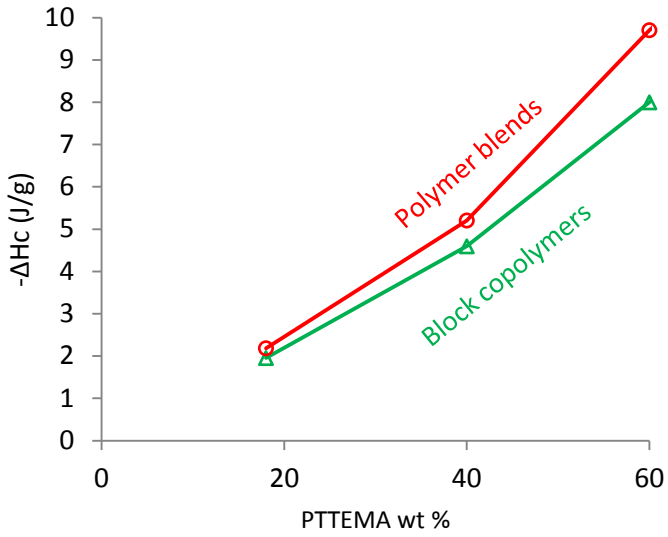

Figure 4.22. $-\Delta H_c$ vs. PTTEMA wt % for PTTEMA-b-PS block copolymers and PTTEMA/PS blends.

As shown in Figure 4.23, the characteristic diffractions peaks for both the pure polystyrene and PTTEMA homopolymers are apparent in the WXRD patterns for PTTEMA-b-PS block copolymers and PPTEMA/PS polymer blends. The main diffraction peak for PTTEMA homopolymer is located at about $2\theta = 19°$, as reported in our previous publication [54]. The crystalline domains in pure polystyrene show characteristic diffraction peaks at 2θ angles of about 8.44° and 19.08°, consistent with literature values for syndiotactic polystyrene [102-106]. For block copolymers, the intensity of the diffraction peaks associated with PTTEMA increased with increasing of PTTEMA content. Polymer blends show similar trends with the PTTEMA content change, except 60 wt (%) PTTEMA blend. The polymer blend containing 60 wt% PTTEMA shows higher intensity at about 7.74°, suggesting macro-phase separation of polystyrene and PTTEMA.

The crystalline domains size can be estimated from Scherrer's formula [55, 56] (equation 2.1), as reported by many other groups [107, 108]. Since the PS diffraction peak at 2θ = 19.08° overlaps with the PTTEMA peaks at 2θ =19°, it is difficult to get precise B values for calculation in the crystallite size of the PTTEMA/PS polymer blends and PTTEMA-b-PS block copolymers. However, for polymer blends, obvious decreases of B values are observed with increasing of PTTEMA wt%, indicating larger crystallite size at higher PTTEMA wt%. For example, crystallite size increases from 1.379 nm to 2.145 nm as PTTEMA content increases from 18 wt% to 60 wt% in PTTEMA/PS blends. PTTEMA-b-PS block copolymers show very small change ranging from 1.36 nm to 1.43 nm with no obvious trends. The formation of larger in crystallite size, domains in PTTEMA/PS polymer blends is believed to be related to PTTEMA homopolymer association in polymer blends.

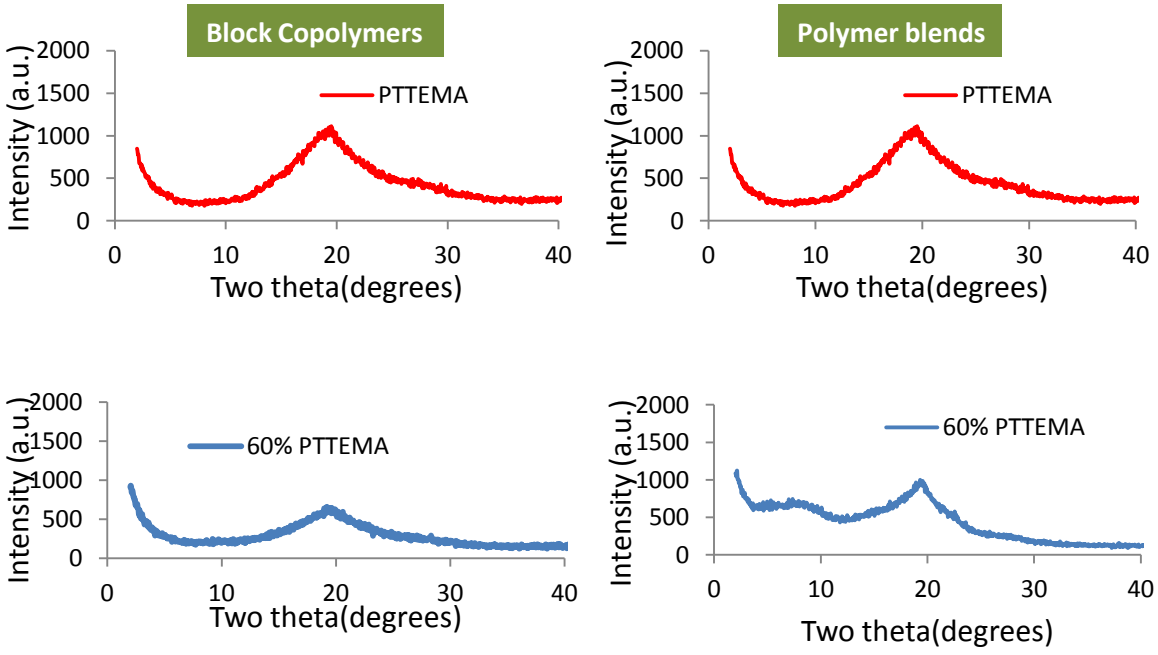

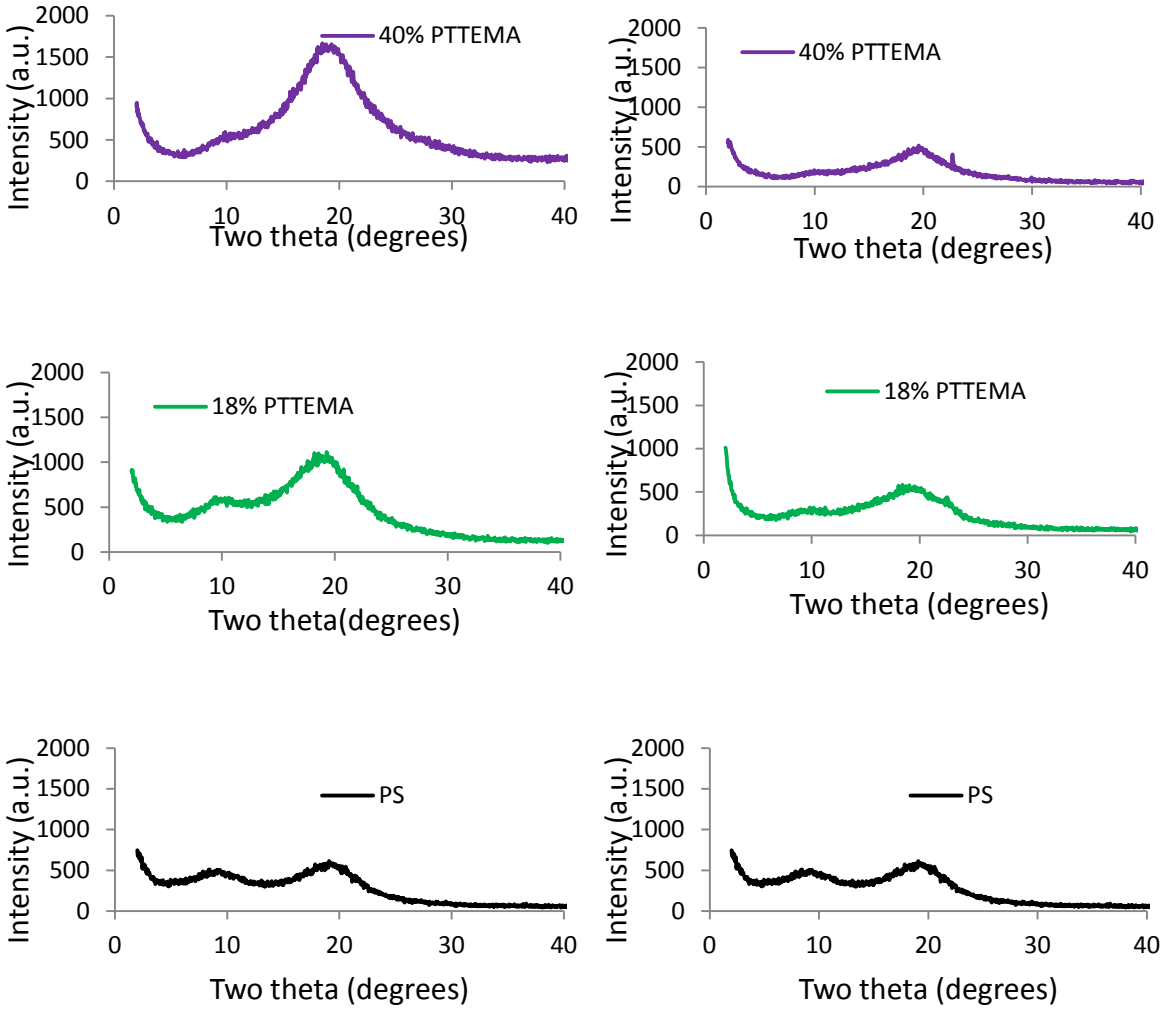

Figure 4.23. WXRD patterns of PTTEMA-b-PS block copolymers (left column) and PTTEMA/PS polymer blends (right column).

Table 4.7. Crystal size information from WXRD for PTTEMA-b-PS block copolymers and PTTEMA/PS polymer blends.

	Homo polymer and PTTEMA-b-PS block copolymers			
	PTTEMA	60% PTTEMA	40% PTTEMA	18% PTTEMA
t=Crystal size (nm)	1.29433	1.43617	1.17997	1.36604
	PTTEMA/PS Polymer blends			

	60% PTTEMA	40% PTTEMA	18% PTTEMA
t=Crystal size (nm)	2.14533	1.59204	1.37955

Figure 4.24a and 4.24a' show the frequency-dependent relative permittivities of block copolymers and polymer blends, respectively. For pure PS, relative permittivity is 2.5 and is nearly independent of frequency. For both the PTTEMA-b-PS block copolymers and PTTEMA/PS polymer blends, relative permittivity increases with PTTEMA wt%. Additionally, these relative permittivities are independent of frequency, which is remarkable compared to significant frequency dependence of PVDF-based materials [40, 41, 43, 46, 109, 110].

The variation of relative permittivity with PTTEMA wt% is more obvious in Figure 4.24b (measured at 1 KHz) and 4.24b' (measured at 1 MHz). At lower PTTEMA wt% (Figure 4.24b), the block copolymers have higher relative permittivities than the polymer blends at the same PTTEMA wt%. However, at higher PTTEMA wt%, we observed no significant relative permittivity difference between the block copolymers and polymer blends. There may be two reasons for these observations. First, at lower PTTEMA wt%, block copolymers with shorter PTTEMA blocks have smaller domains and more of them, while in polymer blends, association of PTTEMA chains in the blends may give fewer and larger domains (Figure 4.25). Thus, block copolymers with greater number of smaller domains produce higher density of polarization, resulting in higher relative permittivity. Likewise, polymer blends with fewer larger domains have lower

polarization density and thus lower relative permittivity. Second, at higher PTTEMA wt%, the advantage of relatively smaller domains in block copolymers are nullified by percolation of adjacent domains, resulting in similar relative permittivities for the PTTEMA-b-PS block copolymers and PTTEMA/PS polymer blends.

All of the block copolymers and polymer blends exhibit very low dielectric loss (expressed in terms of loss tangent, tanδ Figure 4.26a and a'); tanδ is less than 0.02 in all cases. Loss tangent increases with PTTEMA wt%, and reaches a maximum for PTTEMA homopolymers. This suggests that even though the loss tangent is quite low, PTTEMA introduces an additional loss mechanism in the block copolymers and polymer blends. Conductivity measurements are shown in Figures 4.26 b and b'. The conductivity of both the block copolymers and polymer blends are quite low, and no statistically significant trends are observed. This observation, and the nearly constant values of ε_r (Figure 4.24a and 4.24a'), imply that the additional loss mechanism due to PTTEMA is not associated with any ionic conduction.

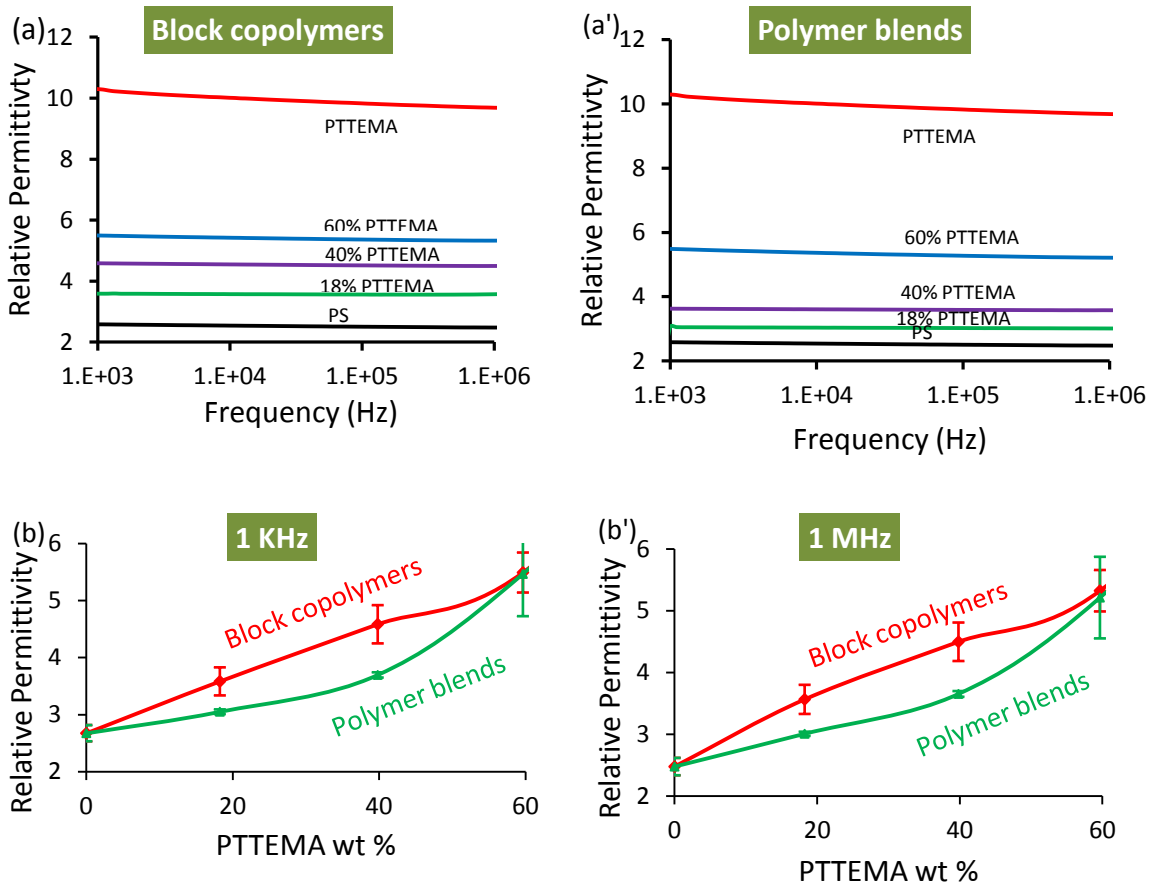

Figure 4.24. Frequency dependent relative permittivity a) PTTEMA-b-PS block copolymers, and a') PTTEMA/PS polymer blends. Relative permittivity change with PTTEMA wt% at applied field frequency b) 1KHz and b') 1MHz.

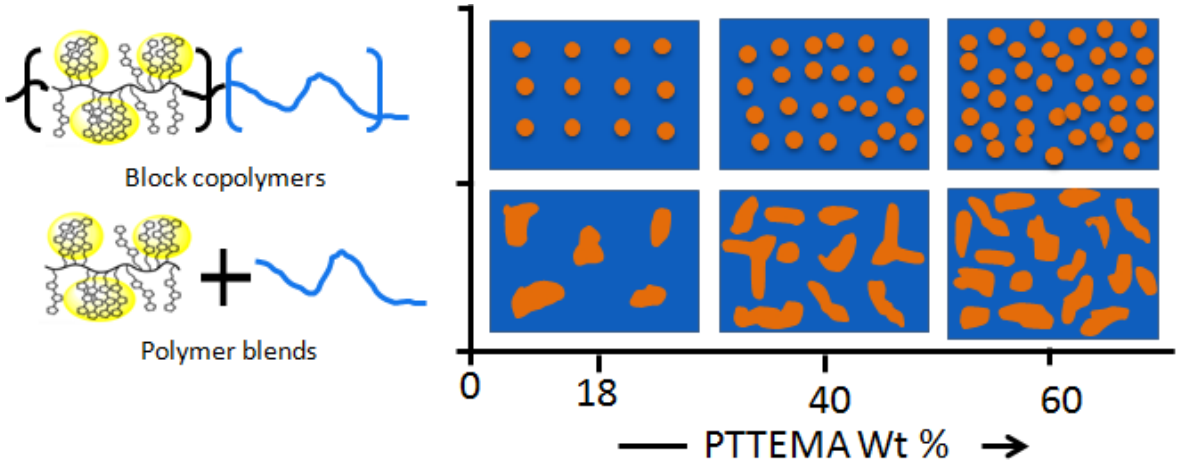

Figure 4.25. Schematic illustration of proposed Microstructure in PTTEMA-b-PS block copolymers and PTTEMA/PS polymer blends with varying PTEMA weight percent.

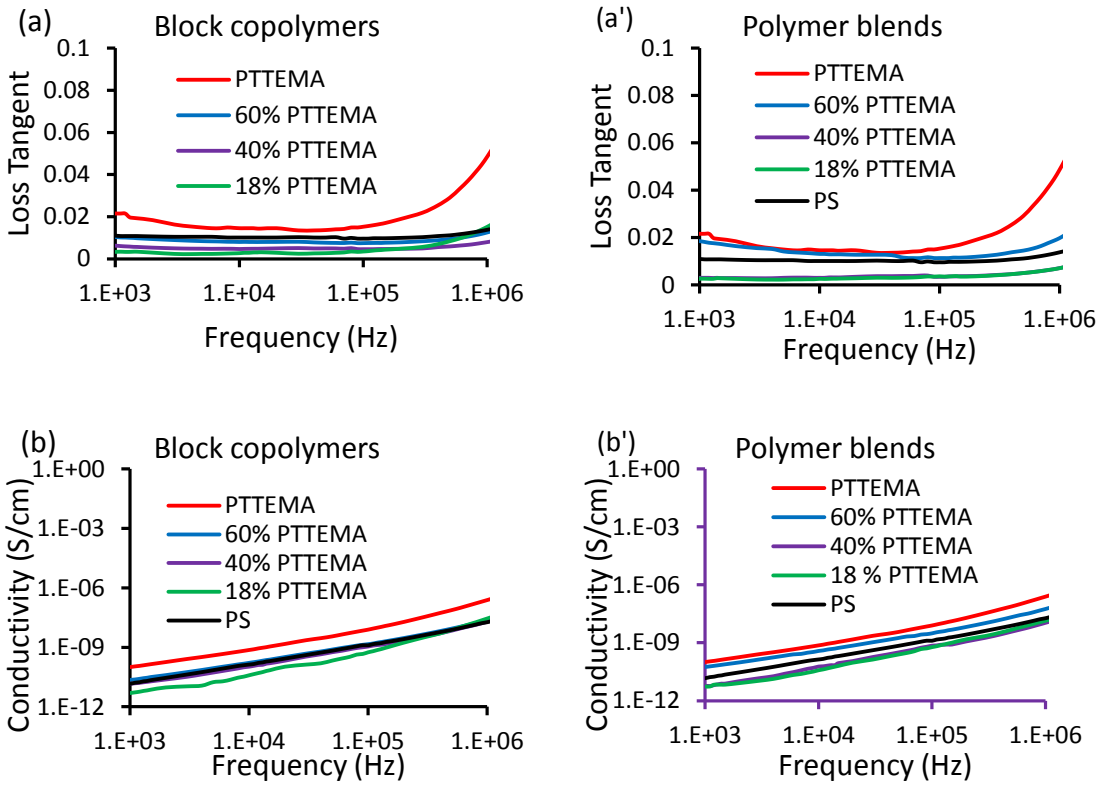

Figure 4.26. Frequency dependent loss tangent and conductivity: (a, b) PTTEMA-b-PS block copolymers, and (a' b') PTTEMA/PS polymer blends, respectively.

Polarization testing provides the dielectric behavior of materials at high applied electric field. Figure 4.27 a and a' show typical polarization (D-E) loops for the block copolymers and polymer blends. Figure 4.27a shows that block copolymers exhibit linear polarization behavior and polarization increase with increasing PTTEMA wt %. Polarization behavior for polymer blends (Figure 4.27a') show similar characteristics: polarization increases with increasing PTTEMA wt% in the blends. The linear polarization behavior in both the block copolymers and polymer blends suggest very low percentage energy dissipation.

Integration of the D-E loops using equation 1.3 gives stored energy density (Figure 4.27b, b'), and percentage energy loss (Figure 4.27 c, c'). PTTEMA homopolymer

(Figure 4.27b) cannot withstand high applied electric field; maximum attainable applied field is 11 MV/m, much lower than the values measured by our Penn State collaborators. their reported values are 150 MV/m for M_w = 22,300 and 200 MV/m for M_w = 64,900 [54]. There may be several reasons for this difference: lower PTTEMA molecular weight (M_w 20,900) difference in film quality, or electrode area. Our previous experience suggests that our lower PTTEMA molecular weight could be the dominant reason for early breakdown. Polystyrene, on the other hand , can depolarized as high as 200 MV/m, which is exactly the same as literature values [1, 5].

As expected, stored energy densities increase with increasing PTTEMA wt% in the block copolymers. Block copolymers with higher PS content show increasingly high breakdown field strength, resulting in higher stored energy density. For example, block copolymer containing 18 wt% PTTEMA shows the highest stored energy density, 0.097 J/cm^3 at 66 MV/m. Polymer blends (Figure 4.27b') show similar trends, normally that stored energy density increases with PTTEMA wt %.The inset represents stored energy density at low applied fields (<10 MV/m) providing comparison with PTTEMA homopolymer. All of the polymer blends can withstand significantly higher applied electric fields compared to the corresponding block copolymers, with the highest field value being 168 MV/m for polymer blend containing 18 wt% PTTEMA. As a consequence, stored energy densities for polymer blends are much higher than the corresponding block copolymers. Among the polymer blends, 18 wt% PTTEMA possesses the highest energy density, 0.57 J/cm^3 at 168 MV/m, which is twice as high as pure polystyrene at the same applied field.

Similar to dielectric loss, all the block copolymers show very low percentage energy loss. The polymer blends, on the other hand, manifest very irregular loss shape. The percentage energy loss varies from 2% for blend containing 18 wt% PTTEMA to 15% for the blend containing 40 wt% PTTEMA at 30MV/m applied field.

Stored energy density ratio at 10 MV/m (Figure 4.28) shows that block copolymers can store more energy than polymer blends at higher mass fraction of PTTEMA.

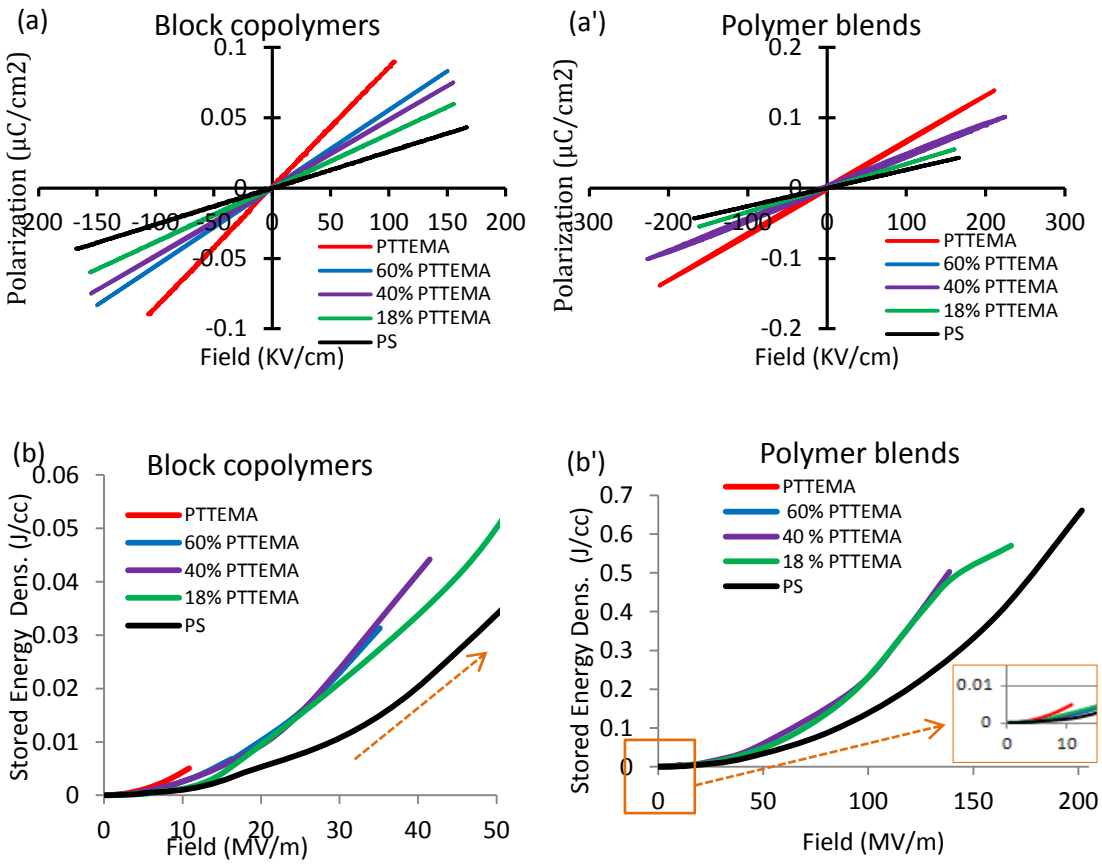

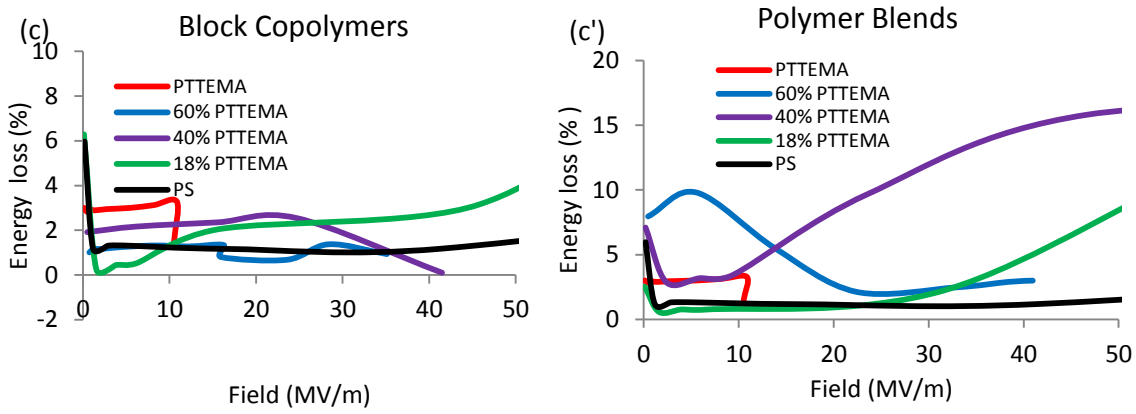

Figure 4.27. Polarization, stored energy density, and percentage energy loss as a functions of applied field for (a, b, c) PTTEMA-b-PS block copolymers and (a', b', c') PTTEMA/PS polymer blends, respectively. The arrows indicate that the data for PS extended beyond the plotted range of applied field. The inset represents the enlarged plot between 0-10 MV/m.

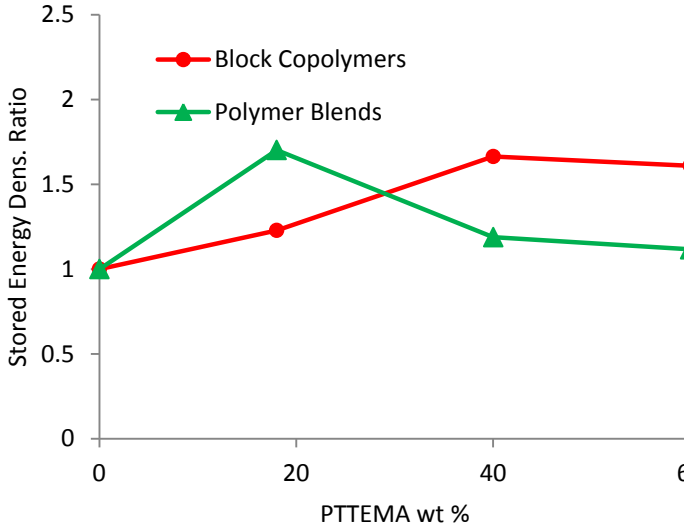

Figure 4.28. Stored energy density ratio (relative to PS homopolymer) measured at 10 MV/m and 1 kHz cycle frequency for block copolymers (red line), and for polymer blends (green line).

4.5.4. CONCLUSIONS

The promising dielectric properties of π-conjugated terthiophene-containing polymers have motivated our efforts to understand the fundamental mechanism

governing the energy storage properties. To explore this topic, we prepared series of diblock copolymers made of polystyrene and terthiophene-containing methacrylate (PPTEMA-b-PS) with varying PTTEMA content, and polymer blends of PTTEMA/PS with the same weight fractions of PTTEMA. The block copolymers were prepared by the RAFT polymerization method, polymer blends were prepared by simple solution blending of constituents. We found that at low PTTEMA wt% block copolymers provide better dielectric properties. At higher PTTEMA wt% there is no significant difference in properties between block copolymers and polymer blends. In both cases higher content of PTTEMA in the polymers results in higher dielectric properties. Polymer blends can be tuned to high breakdown strength by simply blending PTTEMA with higher molecular weight PS. Achieving this in block copolymers may not be that easy. This engineering approach could be generalized, introducing of terthiophene containing polymers in insulating polymer matrix for the development of high energy density capacitor materials.

4.6 TERTHIOPHENE-CONTAINING POLYMER/ $BaTiO_3$ NANOCOMPOSITES[7]

4.6.1. MATERIAL DESIGN

Following the discovery of Π-conjugated oligothiophene-containing polymer [54] as a high performance nanodielectric materials, other approaches are being explored to further increase energy storage properties. This section describes a nanocomposite strategy [111-113] toward high–performance nanodielectric nanocomposites.

Specifically, terthiophene-containing polymer, poly (2-(2, 2':5', 2''-terthien-5-yl) ethyl methacrylate (PTTEMA), has been covalently grafted as a polymer shell around barium titanate (BaTiO3, or BT) particle cores (Figure 4.29a). PTTEMA polymers with varying molecular weight (Table 4.8) were grafted onto the BT surface via surface initiated reverse addition fragmentation chain transfer (RAFT) polymerization (Figure 4.30) giving particles with varying PTTEMA shell thickness. These "PTTEMA@BT" core-shell nanoparticles have been dispersed in a PTTEMA homopolymers matrix. All PTTEMA polymers and PTTEMA@BT hybrid nanoparticles were synthesis by Dr. Yali Qiao, who also performed all physical characterization of these materials.

Based on our earlier results (Section 4.4), PTTEMA homopolymers as well as the grafted PTTEMA can form conjugated nanoscale domains via self-organization of terthiophene side chains. Therefore, the combined PTTEMA homo- and grafted polymers form the matrix phases with distinctive kind of nanodipolar structure. The ferroelectric ceramic BT nanoparticles also form dipolar domains with larger size (diameter ~50 nm) surrounded by PTTEMA's polymer matrix containing nanometer-scale domains (< 2 nm) resulting from self organization of terthiophene side chains (Figure 4.29b). Nanocomposites were fabricated using these PTTEMA@BT hybrid particles with different shell thickness as filler and PTTEMA as matrix (Figure 4.29c).

This system may have some distinct advantages. First, the PTTEMA grafted polymer has exactly the same chemical composition as the PTTEMA matrix, which may enhance the dispersion of BT nanoparticles and improve particles-polymer interfacial adhesion. Second, the PTTEMA shell may serve as a "dielectric buffer layer" that reduces

the permittivity difference between nanoparticles and polymers, promoting more homogenous electric field throughout the nanocomposite and leading to higher dielectric permittivity, low dielectric loss, and higher stored energy density.

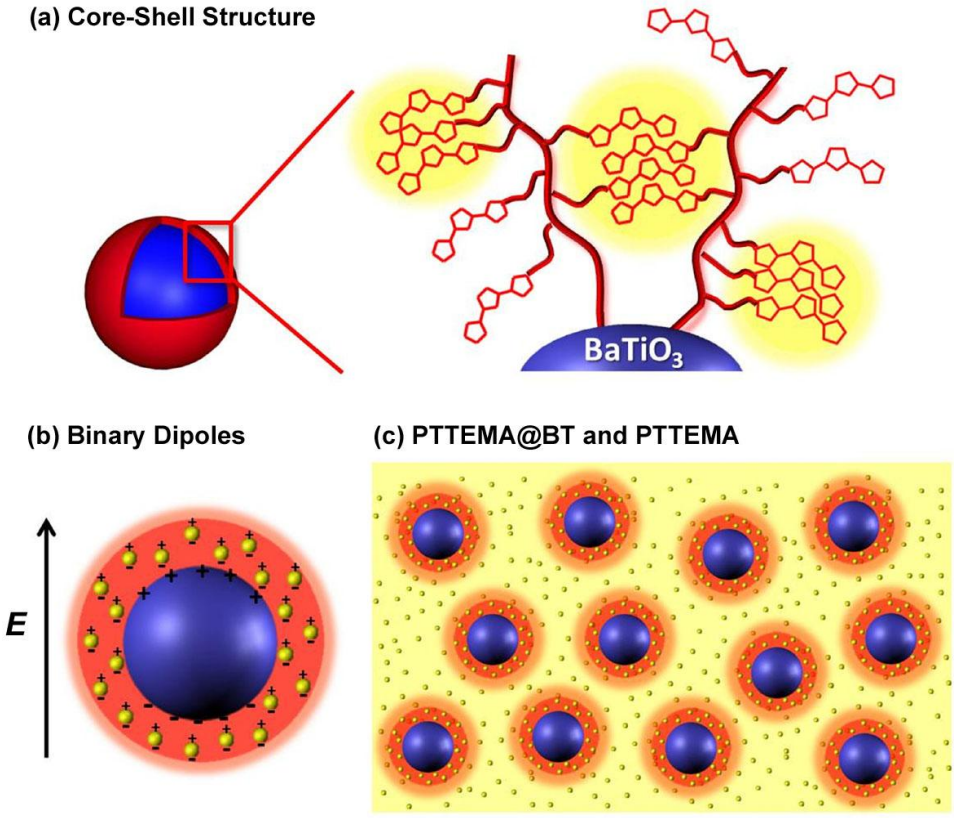

Figure 4.29. Illustration of hybrid nanodielectric materials based on terthiophene-containing polymers: (a) PTTEMA grafted onto $BaTiO_3$ nanoparticles (PTTEMA@BT); (b) dual nanodipole architecture based on PTTEMA@BT hybrid nanoparticles; (c) a novel nanocomposite system using PTTEMA@BT as fillers and PTTEMA as the matrix. Illustration prepared by Dr. Yali Qiao and used by permission.

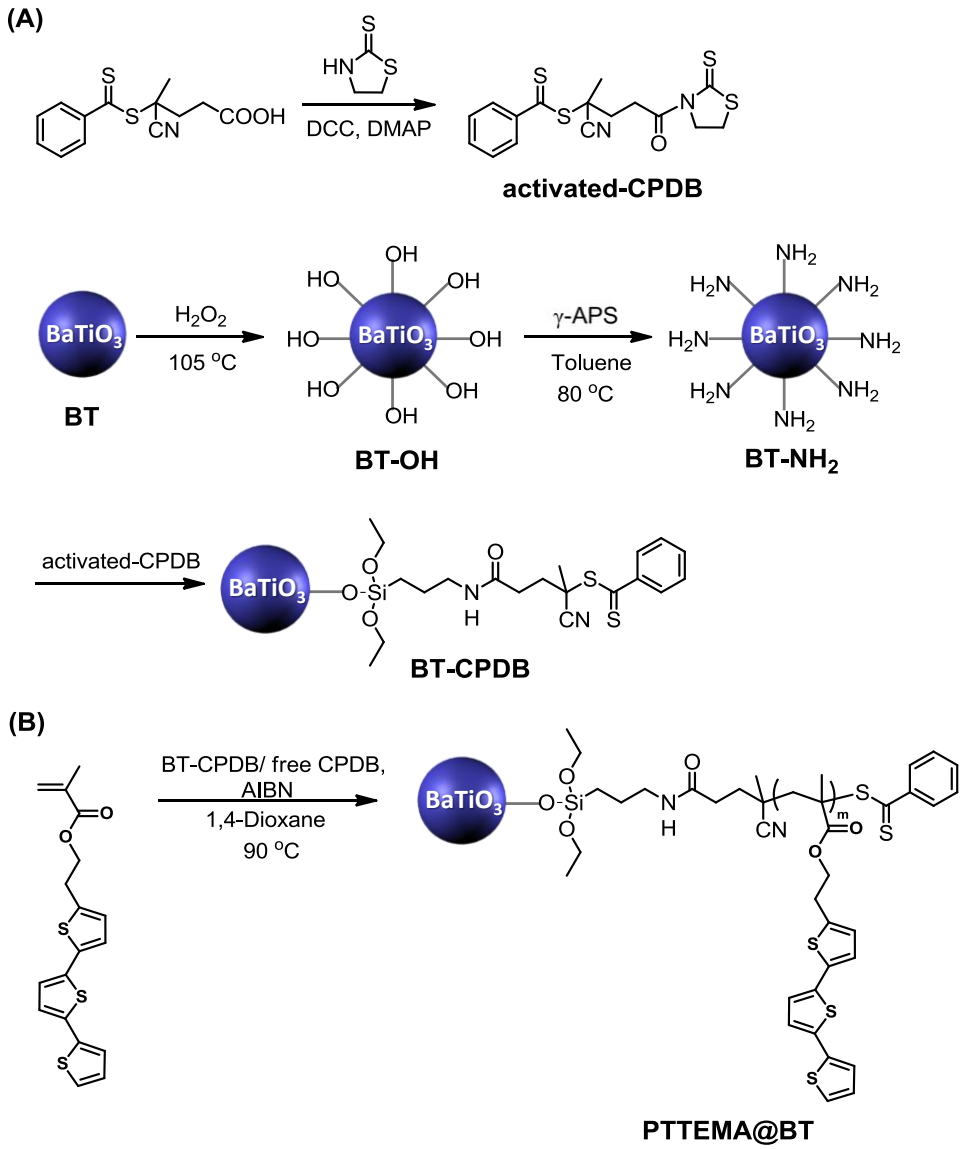

Figure 4.30. Synthesis of PTTEMA surface-modified $BaTiO_3$ nanoparticles by RAFT polymerization; illustration prepared by Dr. Yali Qiao and used by permission.

4.6.2. Physical Characterization

Following the efficient surface-initiated RAFT polymerization, two PTTEMA modified BT nanoparticles (PTTEMA1@BT and PTTEMA2@BT with different degree of polymerization) were prepared. A representative ^{1}H NMR spectrum for PTTEMA@BT (Figure 4.31) shows all of the characteristic peaks of PTTEMA homopolymer, e.g., 6.5–

7.3 (terthiophene ring) and 0.5–2.0 ppm (metharylate backbone), providing evidence of PTTEMA grafting onto BT. The GPC traces of oligothiophene-containing polymers cleaved from the two PTTEMA@BT nanoparticles with different shell thicknesses are presented in Figure 4.32. In both cases, symmetric monomodal peaks are observed. The molecular weight and molecular weight distribution of graft polymers are summarized in Table 4.8. The low PDIs of graft polymers were attributed to the controlled/"living" nature of the surface-initiated RAFT polymerization in such systems.

Figure 4.33a shows thermogravimetric analysis (TGA) results for as-received BT, CPDB-anchored BT [Note: 2-Mercaptothiazoline activation of 4-cyanopentanoic acid dithiobenzoate (CPDB)], and the two different PTTEMA@BT nanoparticles given in Table 4.8. The results showed that the graft polymers possess good thermal stability with the decomposition onset temperatures at ca. 310~320 °C of 5% weight loss. In addition, the TGA measurements exhibited that the weight loss of PTTEMA1@BT and PTTEMA2@BT was much larger compared with that of the BT-CPDB. The weight residues of the PTTEMA@BT nanoparticles are attributed to $BaTiO_3$ because the PTTEMA would be completely degraded at 700 °C.

Differential scanning calorimetry (DSC) measurements (Figure 4.33b) showed that the PTTEMA polymers on the particle surface could still maintain similar melting and recrystallization processes to those in their free homopolymers, though the former less distinct due to the presence of large fraction of BT nanoparticles. The crystallization temperature increased with the increase of molecular weight of the graft polymers, from 119.2 °C for PTTEMA1@BT to 121.6 °C for PTTEMA2@BT (data shown in Table 4.8).

Additionally, the melting points showed similar tendency with the change of molecular weight. Both tendencies of the crystallization temperature and melting point with the molecular weight were quite similar to those of the homopolymers we reported earlier [54]. These results suggested that the graft polymers could still maintain their thermal properties after incorporation onto the BT nanoparticles. Consequently, the formation of crystalline domains induced by the interaction between terthiophene side-chains is likely to occur in such hybrid systems.

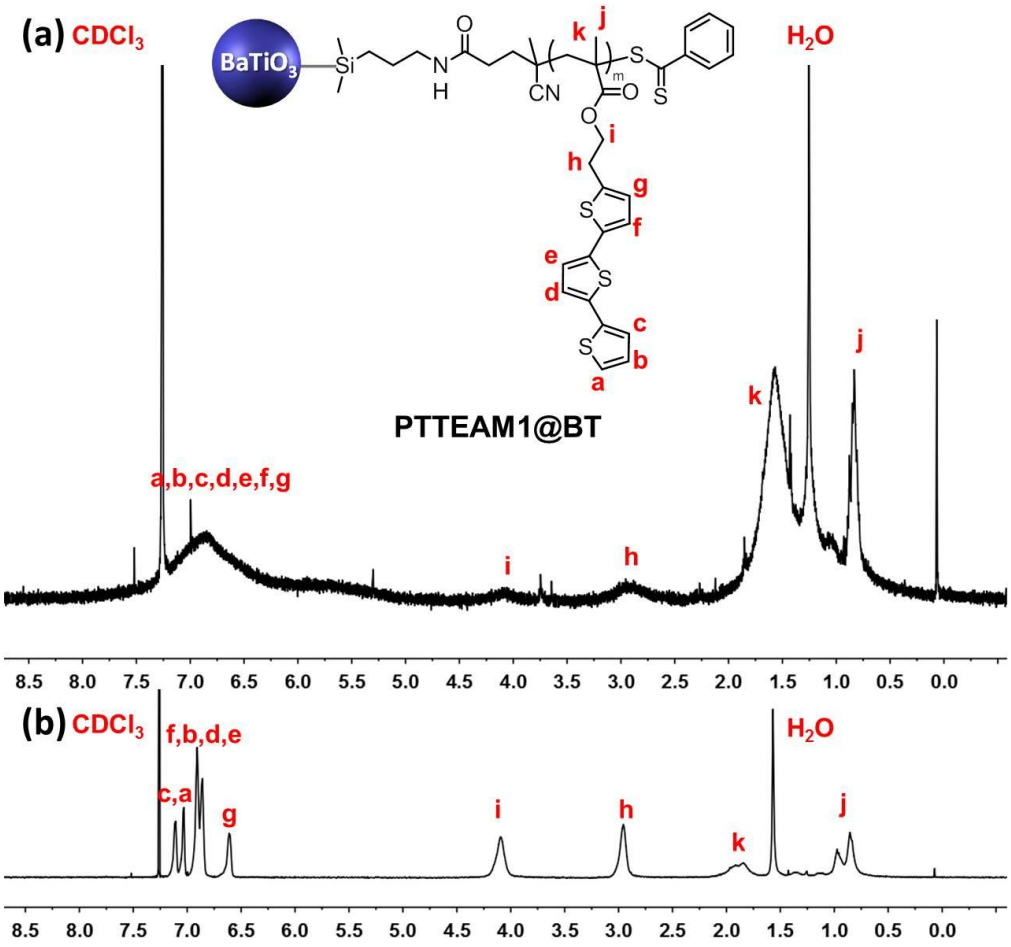

Figure 4.31. ^{1}H NMR spectra of (a) PTTEMA1@BT and (b) PTTEMA homopolymer. Measurements performed by Dr. Yali Qiao.

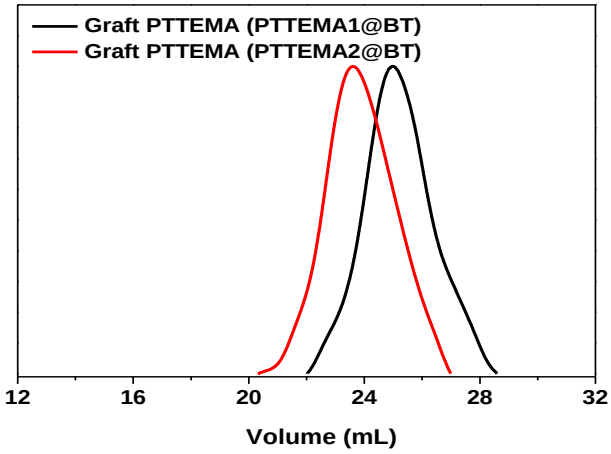

Figure 4.32. GPC traces of graft PTTEMA homopolymers that were cleaved from BT nanoparticles. Measurements performed by Dr. Yali Qiao.

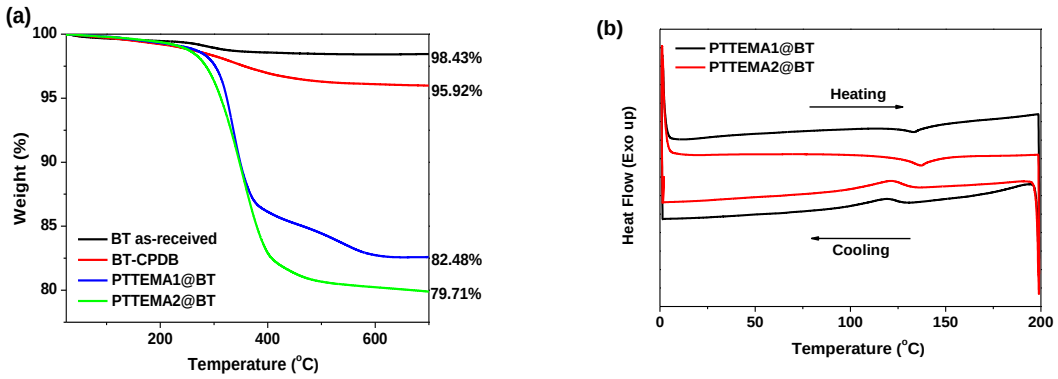

Figure 4.33. a) TGA, and b) DSC curve of surface-modified $BaTiO_3$ nanoparticles. Measurements performed by Dr. Yali Qiao.

Table 4.8. Physical characteristics of PTTEMA@BT hybrid nanoparticles. [a] Obtained from GPC results, the graft polymer was cleaved from BT nanoparticles by aminolysis. [b] Calculated from TGA results based on the weight loss of BT-CPDB at 700 °C; Considering each particle as a sphere nanoparticle with diameter d = ~50 nm and a density of 5.85 g/cm^3, the calculated graft density is 0.21 chains /nm^2. Table prepared by Dr. Yali Qiao.

Sample	M_n (g/mol)[a]	PDI[a]	Weight loss (%)[b]	$T_{recryst}$ (°C)	T_m (°C)
PTTEMA1@BT	22,000	1.12	13.44	119.2	133.2
PTTEMA2@BT	32,400	1.12	16.21	121.6	137.0

The morphologies of the core−shell nanoparticles were characterized by TEM (Figure 4.34). Compared with the as-received BT nanoparticles, a stable and dense polymer shell was clearly coated on the surface of BT nanoparticles. The thickness of oligothiophene-containing polymer shells is about 8−9 nm for PTTEMA1@BT and about 14−15 nm for PTTEMA2@BT.

WXRD patterns of PTTEMA-modified nanoparticles (Figure 4.35) were found to be very similar to those of the pristine nanoparticles. The absence of diffraction patterns from the PTTEMA polymer shell was due to the dominant diffraction peaks from the BT nanoparticles. The inset represents the enlarged pattern between 2θ = 43.5° and 46.5°. The XRD pattern of PTTEMA@BT fits well with the peak positions of the as-received cubic phase BT. Furthermore, only a single diffraction peak at 2θ = 45.2° can be observed in the inset, i.e. no split of the (200) peaks around 2θ = 45° can be seen. This demonstrates that the surface modification of BT nanoparticles has no influence on the phase transition and maintains the characteristics of the cubic phase [114].

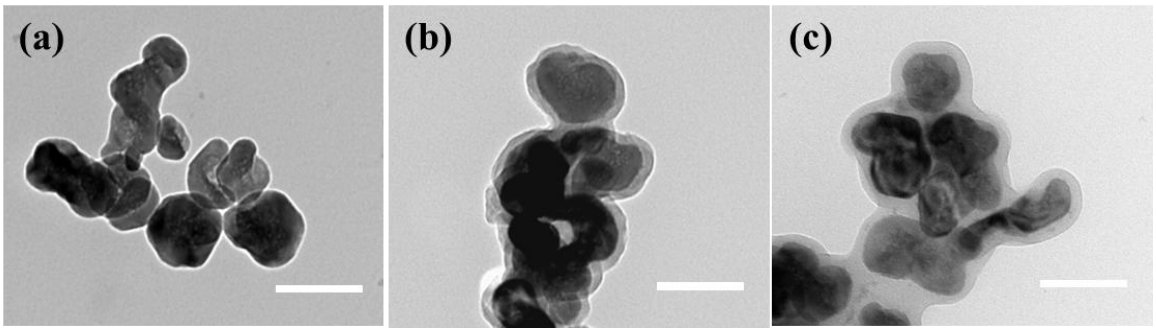

Figure 4.34. TEM images of (a) as-received $BaTiO_3$ nanoparticles; (b) PTTEMA1@BT; and (c) PTTEMA2@BT (the scale bar is 100 nm). Measurements performed by Dr. Yali Qiao.

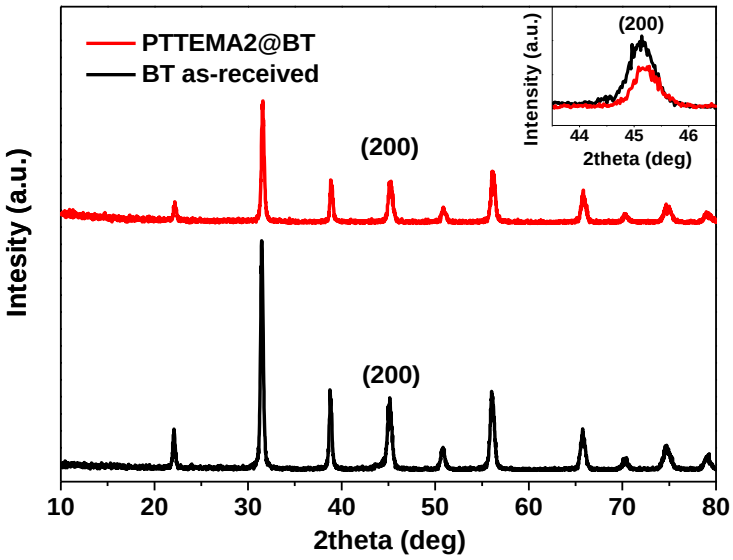

Figure 4.35. WXRD patterns of as-received $BaTiO_3$ nanoparticles and surface PTTEMA-modified $BaTiO_3$ nanoparticles (PTTEMA2@BT). Measurements performed by Dr. Yali Qiao.

DSC and WAXD measurements were performed to estimate the crystalline microstructure of the PTTEMA@BT based nanocomposites in comparison with that of the matrix, aiming at understanding the effects of the inclusion of such hybrid nanoparticles on the microstructure of the PTTEMA polymer matrix. As shown in the DSC profiles obtained in the cooling scan (Figure 4.36), the crystallization temperature (T_c) of all the nanocomposites shifts to lower values, and PTTEMA2@BT based nanocomposites with a thicker polymer shell showed a smaller decrease than those with a thinner polymer shell at various volume fractions of BT nanoparticles. For example, T_c shifted from 113.3 °C for PTTEMA matrix to 93.9 °C and 96.6 °C for PTTEMA1@BT and PTTEMA2@BT based nanocomposites with 5 vol% BT nanoparticles, respectively.

In addition, the introduction of PTTEMA@BT nanoparticles also led to a decrease of the heat of fusion, for instance, changing from 15.25 J/ g for the polymer PTTEMA matrix to 5.584 J /g and 6.284 J/ g for PTTEMA1@BT and PTTEMA2@BT based nanocomposites containing 5 vol% BT nanoparticles, respectively. The results indicated a decrease of the degree of crystallinity resulting from the inclusion of the PTTEMA@BT nanoparticles to the PTTEMA polymer matrix. Moreover, there is a successive decrease in the heat of fusion as the volume fraction of BT nanoparticles further increased from 5 vol%, to 10vol%, and further to 20vol%, regardless of the polymer shell thickness for the hybrid nanoparticles, indicating a continuous decrease of degree of crystallinity with increase of volume fraction of BT nanoparticles in the nanocomposites.

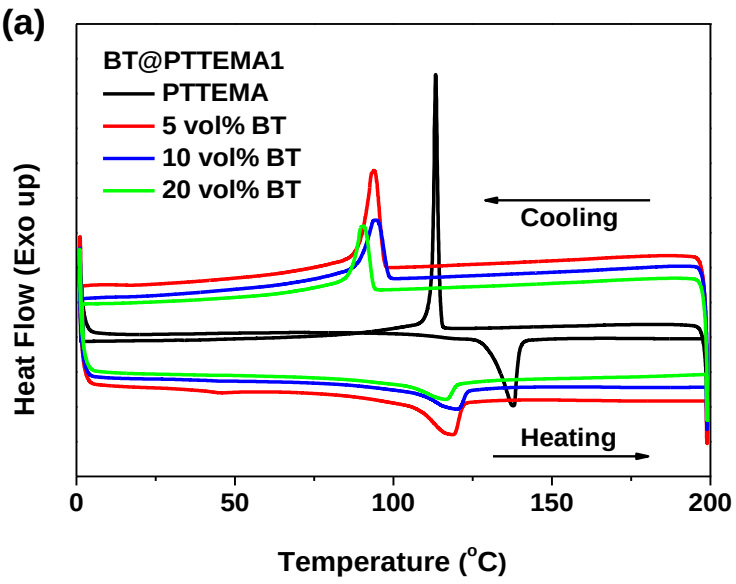

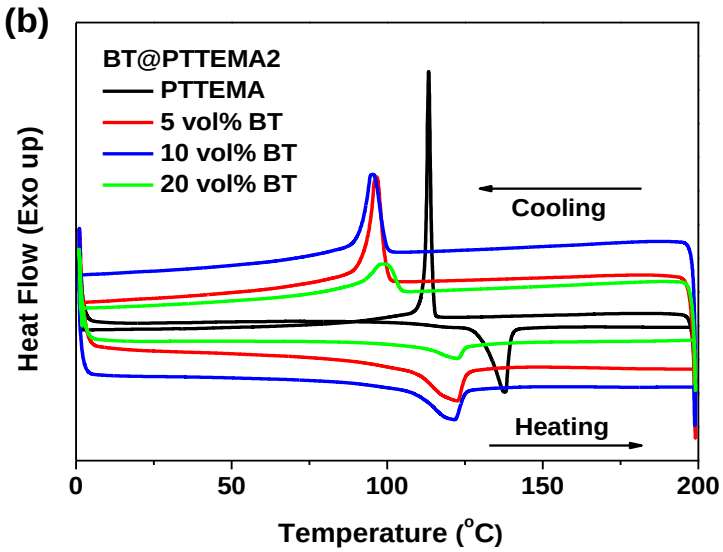

Figure 4.36. DSC curves for the surface PTTEMA-modified BT nanocomposites using (a) BT@PTTEMA1 and (b) BT@PTTEMA2, including different compositions for each kind of nanocomposites compared with pure PTTEMA homopolymer (upper is the exothermal direction). Measurements performed by Dr. Yali Qiao.

As displayed in Figure 4.37, although the WAXD patterns of the nanocomposites are dominated by the diffraction peaks at a 2θ angle of 22.3°, 31.7°, 39.0°, and 45.3° corresponding to cubic phase $BaTiO_3$, a relatively weak and broad peak at a 2θ angle of ca. 19° can still be observed, which is attributed to diffractions from PTTEMA polymer matrix.[115] After inclusion of PTTEMA@BT nanoparticles, the main diffraction peaks become sharper with a dramatically decreased intensity. Theoretically, the crystalline domain size can be estimated from Scherrer's formula,[107, 116] equation 4.1 .Since diffraction peak at a 2θ angle of 22.3° from cubic phase BaTiO3 was partially overlapped with that at a 2θ angle of 19° from the matrix, it is difficult to analyze the exact B values for calculation of the crystallite size of the polymer matrix in the nanocomposites. However, qualitatively, an obvious decrease of the B value for the nanocomposites

could be observed when compared with that of the neat polymer matrix, while maintaining 2θ angle at nearly the same level. Accordingly, the crystalline domain size from the polymer matrix in all the nanocomposites (estimated between 4 ~ 10 nm) showed an increase tendency compared with that of the neat polymer matrix (~1.6 nm) with the introduction of the PTTEMA@BT nanoparticles. Based on our previous work,[115] the formation of crystalline domains in the terthiophene-containing polymer is believed to be induced by the interaction and self-organization between terthiophene side chains, and the crystalline domain sizes has a close relationship with the probability and proportionality of contact of the side-chains. With inclusion of PTTEMA@BT nanofillers in the polymer matrix, the terthiophene side-chains in the polymer shell grafted on the surface of the nanoparticles increase the probability of accessibility of adjacent terthiophene segments either from the surface or from the polymer matrix, thus might enhance the proportionality of the interacted side chains, both of which are beneficial for formation of larger crystalline domains. However, for both kinds of PTTEMA@BT based nanocomposites, the crystallite size from the polymer matrix slightly decreased with the increasing of the volume fraction of BT nanoparticles from 5 vol% up to 20 vol%.

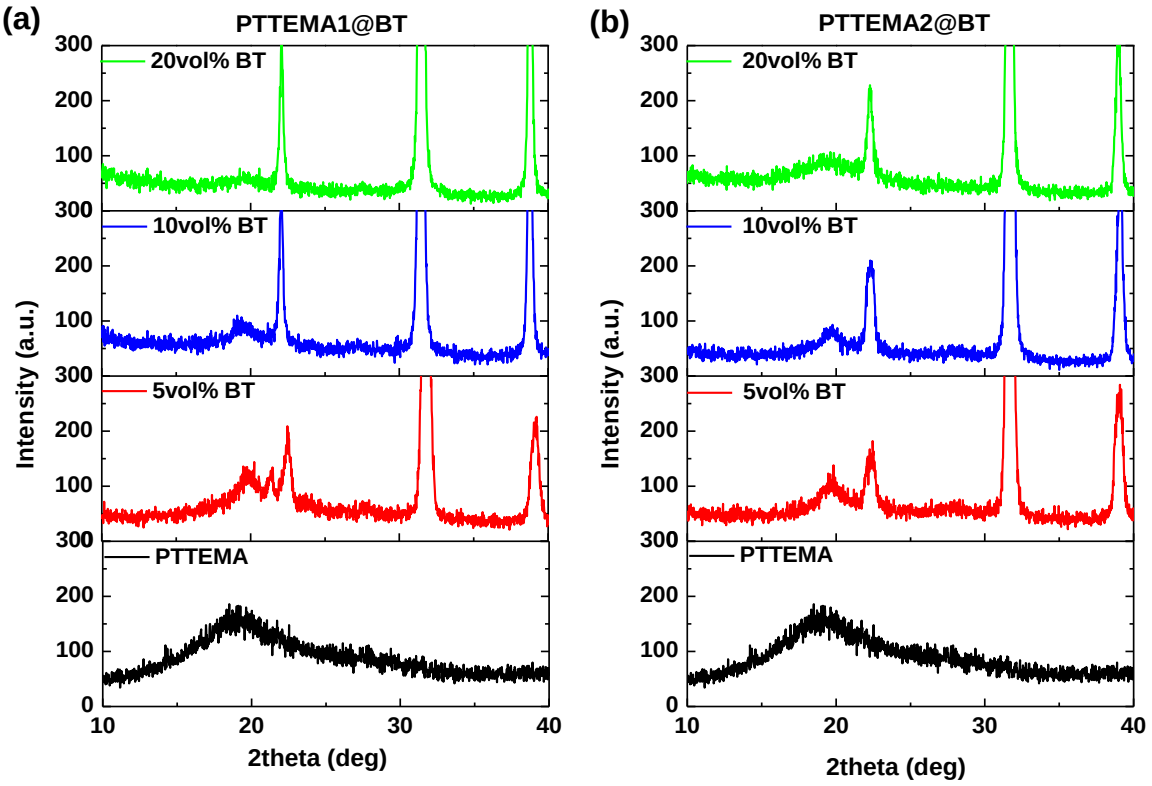

Figure 4.37. WXRD patterns of the surface PTTEMA-modified BT nanocomposites using (a) PTTEMA1@BT and (b) PTTEMA2@BT, including different compositions for each kind of nanocomposites compared with pure PTTEMA homopolymer. Measurements performed by Dr. Yali Qiao.

4.6.3. Film Preparation

Composite films for dielectric property characterization were prepared by solution blending using THF. PTTEMA was dissolved in THF (35 mg /mL), and BT or PTTEMA@BT particles were suspended in THF with 1-2 h sonication. The solutions were blended, sonicated for an additional 30 min, and then poured into heavy-gauge aluminum pans. The THF was removed by evaporation at 44°C under reduced pressure (635 mm Hg absolute) for about 2 h without any post-treatment (thermal annealing). This resulted in films with uniform thickness and free of bubbles, cracks, or other

defects. Film thicknesses were measured at multiple positions with a micrometer, with values in the range of 3-20 μm. Strips of aluminum pan bearing polymer or composite films were cut using scissors. The aluminum pan served as the bottom electrode for dielectric measurements. Gold was sputter-coated under argon atmosphere through a shadow mask to deposit circular gold electrodes (area 0.13 cm^2) on the films' top surfaces.

The complex impedance of polymer and composite film samples was measured using an impedance analyzer. Polarization measurements at higher applied voltages employed a polarization tester. Measurement and data analysis procedures are discussed in Chapter 2 (Section 2.2).

PTTEMA density is assumed to be the same as PMMA, 1.20 g/cm^3. BT density was provided by supplier (4.85 g/cm^3). TGA gave amount of PTTEMA in hybrid PTTEMA@BT particles. Using these densities and weight loss data from TGA (Table 4.8), conversion from wt% to vol% is made.

4.6.4 Dielectric Property Characterization

Figure 4.38a shows the frequency-dependent relative permittivity of PTTEMA@BT/PTTEMA nanocomposites with pristine BT, PTTEMA1@BT and PTTEMA2@BT nanoparticles dispersed in PTTEMA homopolymer matrix. In every case, upon addition of nanoparticles to the homopolymer matrix results in increase of the relative permittivity (ε_r) compared to that of the homopolymer. These relative permittivities are nearly constant over a wide frequency range (1 KHz-1 MHz).This observation is remarkable compared to the significant frequency dependence of widely

studied nanocomposites based on PVDF homopolymers and copolymer [94, 107, 117-122].

Figure 4.38b shows the variation of relative permittivity with BT vol%. As expected, ε_r values increase with BT volume loading, reaching value twice as high compared to PTTEMA matrix at 20 volume % BT loading. For all BT vol% loading, ε_r values for composites containing PTTEMA@BT particles were significantly higher than those of composites containing pristine BT. Furthermore, ε_r values for PTTEMA2@BT composites (higher MW grafted polymer) are significantly greater than those of PTTEMA1@BT composites (lower MW grafted polymer). There may be two reasons for these observations. First, the presence of the grafted PTTEMA layers probably promotes better dispersion of the BT particles, resulting in more uniform distribution of the electric field over BT and thus higher effective permittivity. Second, the grafted PTTEMA layers may influence the quantity and the size of the PTTEMA crystalline domains so as to increase the density of polarizable dipoles in the polymer domains, resulting in increased permittivity.

All the nanocomposite film exhibits dielectric loss (expressed in terms of loss tangent, tan δ, in Figure 4.39) higher than that of pure PTTEMA homopolymer. However, these tan δ values are relatively low compared to the values found for BT/PVDF composites [119, 120, 122]. The PTTEMA homopolymer has very low loss tangent, rising from 0.007 to 0.014 over the frequency range 1 KHz to 1 MHz. The tan δ values for all BT/PTTEMA nanocomposites are below 0.03; even though it is quite low,

these values are still 2-3 times higher than those for PTTEMA. This suggests that BT particles introduce additional loss mechanisms in the polymer nanocomposites. All BT@PTTEMA/PTTEMA composites show tan δ values less than 0.02. Considering only 20 vol% loading samples, composites containing PTTEMA-grafted BT particles have lower dielectric loss than composite containing pristine BT particles. However, the tan δ values for composites with PTTEMA1@BT and PTTEMA2@BT do not show any significant difference. One plausible explanation is that grafted PTTEMA impedes surface diffusion of polarized species at the PTTEMA/BT interface. In addition, improved dispersion of PTTEMA@BT (relative to pristine BT) in the PTTEMA matrix may play a role in reducing dielectric loss.

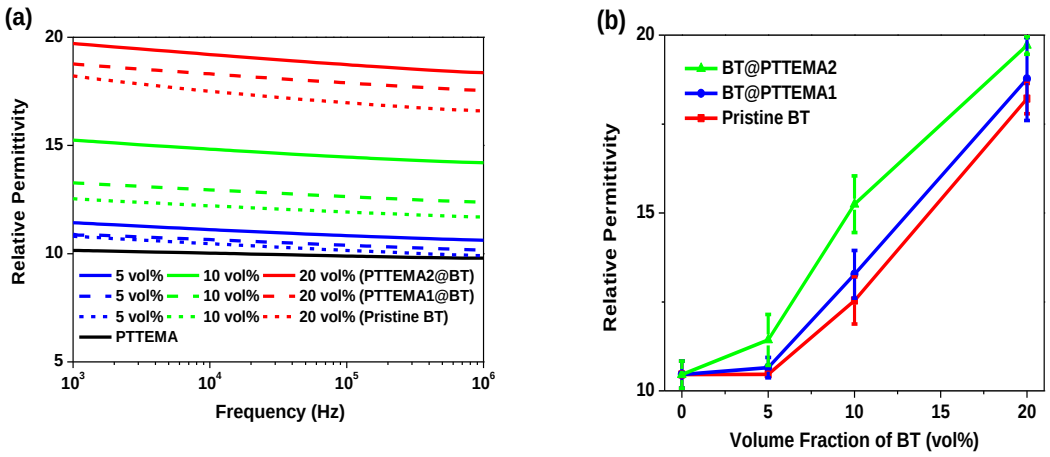

Figure 4.38. Relative permittivity of BT/PTTEMA and PTTEMA@BT/PTTEMA nanocomposites and pure PTTEMA homopolymer (a) as functions of frequency and (b) as function of vol% BT loading at fixed frequency (1 kHz).

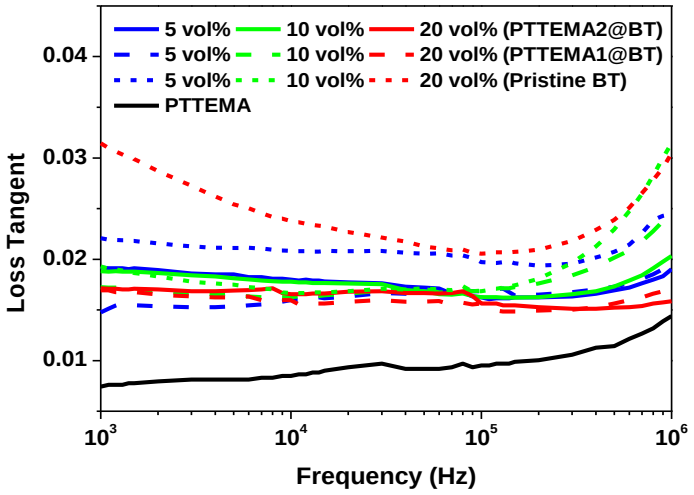

Figure 4.39. Loss tangent of BT/PTTEMA and PTTEMA@BT/PTTEMA nanocomposites and pure PTTEMA homopolymer as functions of frequency.

Polarization testing gives dielectric properties at high applied fields. Figure 4.40 shows typical electric displacement–electric field (D-E) loops. The slopes of the composite D-E loops and composite polarizability increase with nanoparticle loading (Figure 4.40a). With the increase of applied electric field, 20 vol% PTTEMA2@BT composite exhibits a significant amount of hysteresis, indicating charge migration and incipient dielectric breakdown.

Figure 4.40b compares D-E loops for the 20% vol composites prepared with different surface treatments. The composite prepared with PTTEMA@BT show higher polarization compared to composite prepared from pristine BT particles. Furthermore, polarization increases with PTTEMA shell thickness: thicker PTTEMA grafted layer gives higher polarizabilies (PTTEMA2@BT > PTTEMA1@BT). These trends become more obvious in Figure 4.41a, which shows stored energy densities for pure PTTEMA and BT/PTTEMA composites. Stored energy density increases with BT vol% loading;

PTTEMA2@BT/PTTEMA (Figure4.42), stored energy density is nearly 3.5 times that of PTTEMA homopolymer. For every vol% BT loading, stored energy density enhancement follows the order BT<PTTEMA1@BT< PTTEMA2@BT. Figure 4.41b shows percentage energy loss; clearly energy lossiness with the addition of BT. Percentage energy loss for PTTEMA is well below 3%; the highest energy loss is observed in composites 20 vol% BT loading regardless of surface modification. These percentage energy losses are unexpected, however. With PTTEMA-grafted BT particle, one might expect better dispersion of BT particles in PTTEMA polymer matrix, promoting uniform electric field distribution through the composite and lower energy loss. Film uniformity and film thickness variation might be dominating factors, which could offset the other contributions promoting high energy density. However, for most of the composites, percentage energy loss remains below 5%, which is promising for high density energy storage applications.

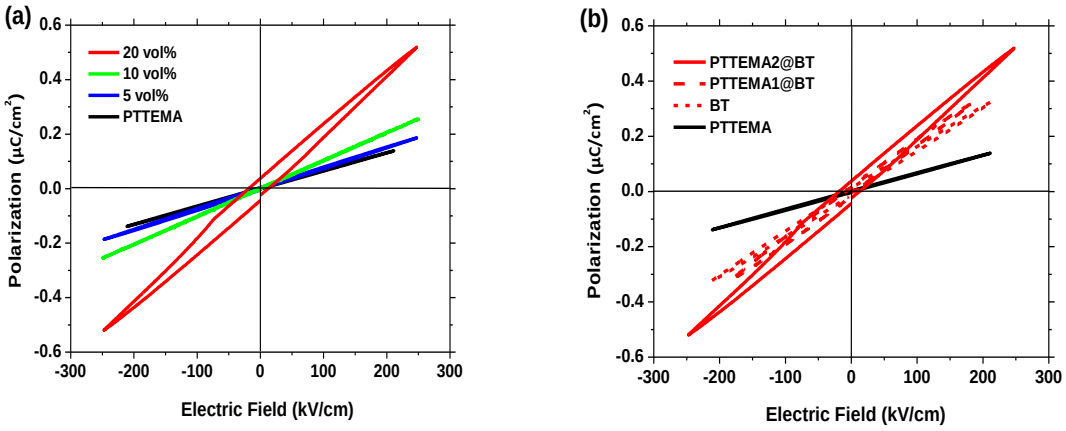

Figure 4.40. Polarization as a function of applied electric field for (a) pure PTTEMA homopolymer and PTTEMA2@BT/PTTEMA nanocomposites containing varying BT nanoparticles vol% loading; and (b) pure PTTEMA homopolymer, and BT/PTTEMA, and

PTTEMA@BT/PTTEMA nanocomposites contain 20 vol% loading of BT nanoparticles. D–E loops were measured at 1 kHz cycle frequency.

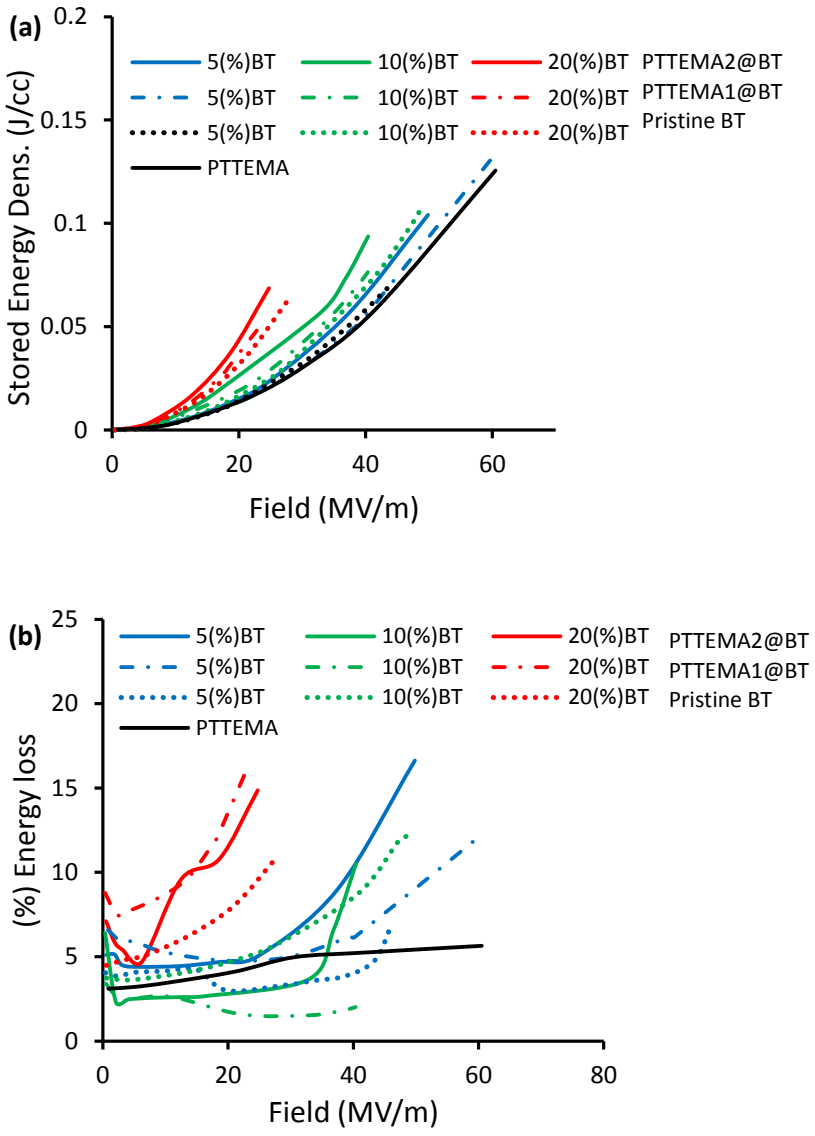

Figure 4.41. a) Stored energy density, and b) percentage energy loss for PTTEMA homopolymer, BT/PTTEMA, and PTTEMA@BT/PTTEMA nanocomposites as functions of applied electric field.

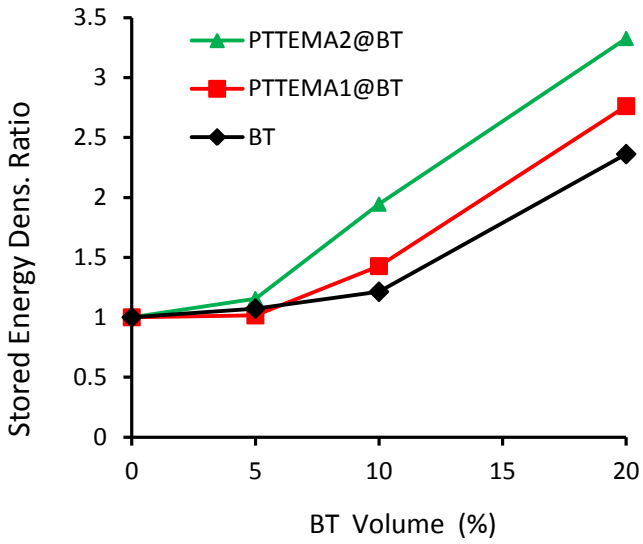

Figure 4.42. Stored energy density ratio ($\hat{W}_{PTTEMA\text{-}nanocomposite}$ /$\hat{W}_{PTTEMA)}$ measured at 21 MV/m and 1 kHz cycle frequency.

4.6.5. Conclusions

The novel "dual dipole" architecture based on PTTEMA@BT nanoparticles dispersed in PTTEMA has been developed. This approach might give increased number density of small crystalline domains compare to PTTEMA homopolymer, resulting in higher density of nanoscale polarizable domains. Composites incorporating PTTEMA@BT have higher relative permittivity and lower loss over the 1 KHz to 1 MHz frequency range compared to composites made from pristine BT. The thickness of the PTTEMA grafted layer on BT particles had a significant impact on overall composite properties: the higher MW PTTEMA gave a thicker graft layer, and the resulting composite (PTTEMA2@BT) exhibited a better dielectric properties than the composite made with BT grafted with lower molecular weight PTTEMA (PPTEMA1@BT). The relative permittivity increased with BT loading, while the dielectric loss remained low. Similar characteristics were also observed for polarization measurements; the dielectric

polarization increased with BT vol% loading. Most of the composites showed linear polarization-depolarization behavior with low energy loss, similar to that of PTTEMA homopolymers. PTTEMA@BT/PTTEMA composite exhibits more than three times higher stored energy density than pure PTTEMA at 21 MV/m. With more uniform and smooth films, we expect to reach even higher applied fields for this polymer nanocomposite. Overall, this novel nanocomposite system simultaneously fulfills the requirements for both the high permittivity and low dielectric loss over a wide frequency range (1 KHz-1MHz), and consequently has great potential for dielectric energy storage.

CHAPTER 5

MATHEMATICAL MODELING OF NANOCOMPOSITE DIELECTRIC PROPERTIES

5.1 INTRODUCTION

To cut down on manufacturing expenses, numerical approaches and computer aided simulation has become an indispensable part of science and engineering. In particular, Finite Element Method (FEM) analysis has been applied to the design process to minimize the development time and anticipate the output patterns. With advancements in computer technology, simulation of nanodielectric capacitor to predict the real-world results has become a reality. The COMSOL multiphysices empowered Finite Element Analysis can calculate the effective properties of the nanocomposites easily. Effective properties of the composite can be calculated by modeling the permittivity via the Effective Medium Theory and generalized effective medium theory (EMT) or other similar mean field theories [86, 123-127]. The EMT utilizes various properties of the resultant medium such as shape, size, fraction of inclusions, individual dielectric permittivity, conductitivty etc. to calculate the composite effective permittivity [128, 129].

Previous research [128-137] motivated us to carry out mathematical simulations to estimate the importance of the host polymer matrix and filler properties on dielectric performance of polymer nanocomposites. Insight gained from modeling studies can lead to improved design of high performance dielectric materials for energy storage applications. In particular, we would like to visualize the electric field distribution throughout the polymer composite microstructure in order to rationalize the effects of inclusions on the overall dielectric properties of the composites. COMSOL Multiphysics was used for the simulation studies.

5.2 SIMULATION DESCRIPTION

In the COMSOL Multiphysics software, Electric Currents (ec) under AC/DC module in stationary study mode was selected as the application module[8]. Circular-shaped filler particle was embedded in a square domain representing the polymer matrix to mimic the 2D geometry of a polymer composite. One of the boundaries was set to apply a fixed voltage, while the opposite boundary was set as a ground. The other two boundaries were set as electrical insulators. For a given set of constitute properties defined in sub domain “Global Definitions” a fixed applied voltage (200V in this case), COMSOL solves the governing conservation equations to determine the materials dielectric properties at the assigned frequency (1 kHz in this case). The parameters required for this simulation were the relative permittivity and conductivity of the embedded particle and matrix polymer, which were obtained from experimental measurements and literature.

❽Model progress tree: COMSOL Multiphysics >2D>AC/DC module> Electric Currents (ec) >stationary.

COMSOL solves abbreviated forms of following Maxwell equations [138] for polymer composite materials:

$$\nabla . \boldsymbol{J} = Q_j \qquad (5.1)$$

$$\boldsymbol{J} = (\sigma + j\omega\varepsilon_r\varepsilon_o)\boldsymbol{E} + \boldsymbol{J_e} \qquad (5.2)$$

$$\boldsymbol{E} = -\nabla V \qquad (5.3)$$

where J is current density , Q is charge density, σ is electric conductivity, J_e is external current density, which is zero in this case. Other symbols mean usual meaning.

Boundary conditions:

Voltage applied port: $V = V_o$

Electric insulation: $\boldsymbol{n}.\boldsymbol{J} = 0$

Ground: $V = 0$

5.3 SIMULATION RESULTS AND DISCUSSION

As shown in Figure 5.1 and Table 5.1, polymer with higher relative permittivity (ε_p) provides higher electric energy density, for same filler wt% loading and relative permittivity (ε_f). For example, insertion of 20 wt% filler with ε_f = 500 (Table 5.1) in polymer with ε_p = 10 results in electric energy density 13100 J/m^3, 5 times higher than that obtained from polymer having ε_p= 2. However, change of filler relative permittivity

(ε_f) does not seem to have a significant impact on the overall electric energy density of the composites. For order of magnitude decrease in filler relative permittivity, from 500 to 50 in 20 wt% composite, electric energy density decreases by only 11% (Table 5.1). From Figure 5.2, it is more apparent that composites can store the highest density of electric energy when both the polymer and the filler have high relative permittivity. This suggests that to achieve high performance in dielectric composites, simply inserting high dielectric constant fillers does not necessarily results in high stored energy density.

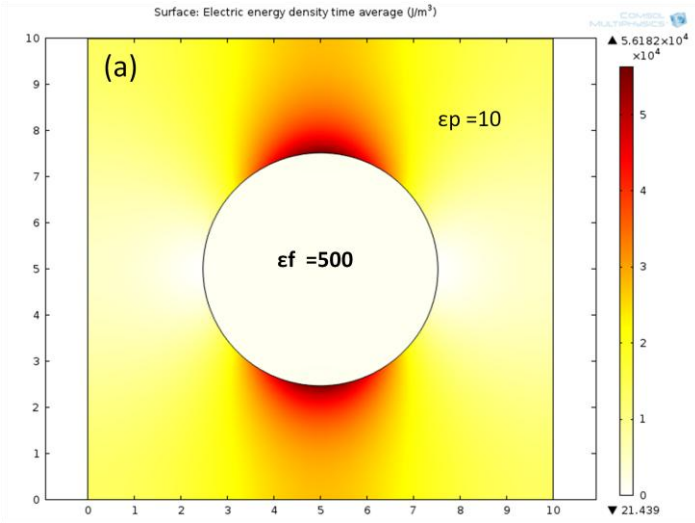

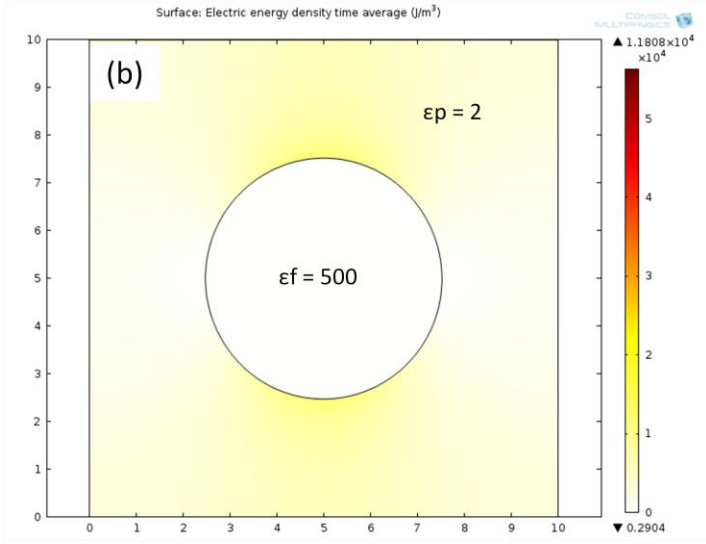

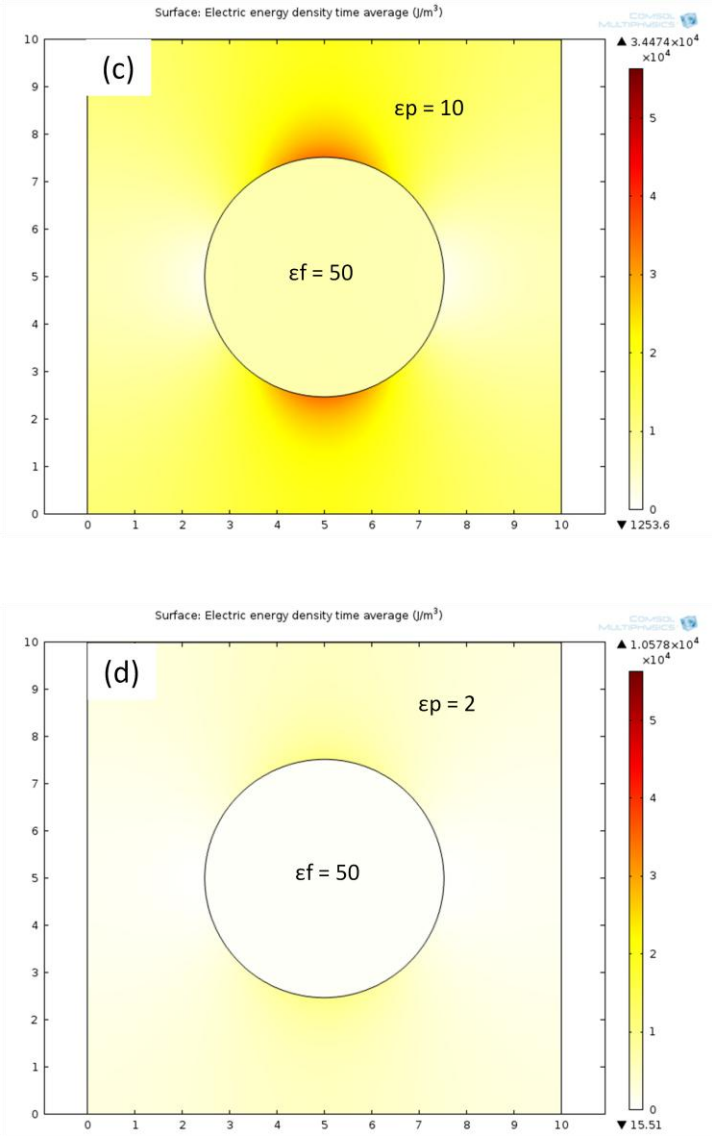

Figure 5.1. Distribution of electric energy density in polymer composites containing 20 wt % filler for different combinations of filler (ε_f) and polymer relative permittivity (ε_p) including: (a) ε_p=10, ε_f=500; (b) ε_p=2, ε_f=500; (c) ε_p=10, ε_f=50, and (d) ε_p=2, ε_f=50

Table 5.1. Simulation results for polymer composite at different combination of filler and polymer relative permittivity.

Simulation Results at 1 KHz, Polymer conductivity = 1E-8(s/m), and filler conductivity = 1E-13(s/m)

Figure	Material	Relative Permittivity	Electric Energy Density Time Avg. (J/m^3)	Overall Elect. Energy Density Time Avg.(J/m^3)	Effective Relative Permittivity
	Polymer	10	16100	13100	14.76-0.261i
	Filler	500	1100		
	Polymer	2	3300	2700	2.99-0.267i
	Filler	500	50		
	Polymer	10	13000	11600	13.0779-0.208i
	Filler	50	6600		
	Polymer	2	3200	2600	2.906-0.253i
	Filler	50	400		

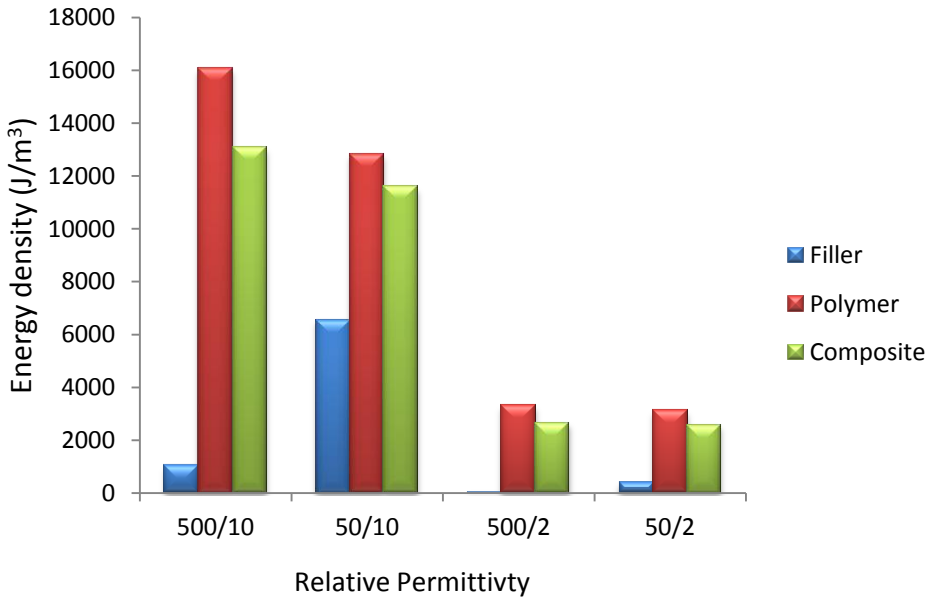

Figure 5.2. Average energy densities in filler, polymer, and overall composite for different combination of filler and polymer relative permittivity.

CHAPTER 6

FUTURE WORK TOWARD NEXT GENERATION OF DIELECTRIC MATERIALS

6.1 EXPLORE MATERIALS THAT SATISFY BOTH DIELECTRIC AND MECHANICAL PROPERTIES

Polymethacrylate with terthiophene side chains (PTTEMA) exhibit several excellent dielectric properties including high dielectric constant with very low dielectric loss, and nearly linear polarization and depolarization cycle. However, PTTEMA materials are brittle, and consequently limit their applications as potential high performance materials. Improving mechanical strength can improve flexibility and robustness, and thus breakdown strength of the material. Block copolymers and polymer blends approaches are explored. The potential gain from addition of higher mechanical strength segment in block copolymers or polymer blends are counter balanced by lower polarization from them and thus resultant polymer gives lower overall polarizability. So introducing new segment with inferior polarizability in PTTEMA polymer cannot solve this problem completely.

PTTEMA polymer has methacrylate backbone with terthiophene side chain. From our previous study [54], it is clear that terthiophene segment provides higher

polarizability and methacrylate segment provides mainly insulation and mechanical strength to overall polymer. Now, replacing the methacrylate backbone by tougher and high breakdown strength ferroelectric polymeric materials could be another approach to solve this issue (Figure 6.1). This approach has advantage over block copolymer and polymer blend approach due to the fact that it will not increase mass fraction of lower polarizable polymer. With appropriate design, smaller amount of tougher ferroelectric polymer segment can provide better mechanical property as well as higher breakdown strength. Several candidate polymers with high mechanical property and low dielectric loss such as polycarbonate, polystyrene, polyamide-imide and many others can be explored.

In addition, I will continuously search for other novel polymers, block copolymers, and tune polymer nanocomposites that satisfy both high dielectric properties and ensure good mechanical integrity. I wish to use polyether ether ketone (peek), epoxy, and odd number polyamides as polymer matrix to fabricate mechanically robust polymer nano composites.

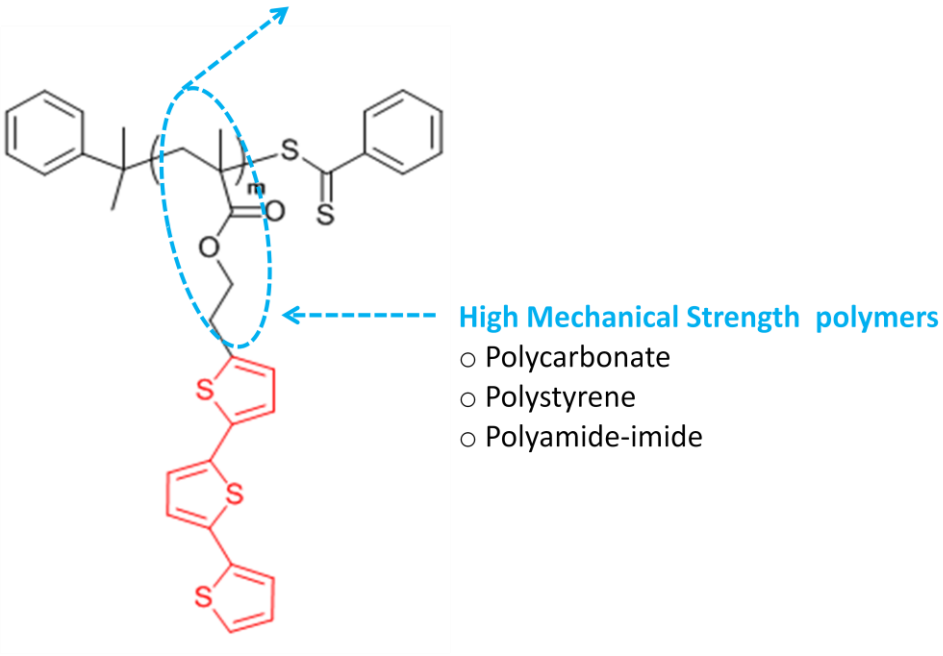

Figure 6.1. Suggested schematic diagram for terthiophene-containing (PTTEMA) polymers to achieve better mechanical property.

REFERENCES

[1] Barber P, Balasubramanian S, Anguchamy Y, Gong S, Wibowo A, Gao H, et al. Polymer composite and nanocomposite dielectric materials for pulse power energy storage. Materials. 2009;2(4):1697-733.

[2] Cao Y, Irwin PC, Younsi K. The future of nanodielectrics in the electrical power industry. Dielectrics and Electrical Insulation, IEEE Transactions on. 2004;11(5):797-807.

[3] Nalwa HS. Handbook of Low and High Dielectric Constant Materials and Their Applications, Two-Volume Set: Academic Press; 1999.

[4] Osaka T, Datta M. Energy Storage Systems in Electronics: CRC Press; 2000.

[5] Raju G. Dielectrics in Electric Fields. 2003. New York: Marcel Dekker.

[6] Barshaw E, White J, Chait M, Cornette J, Bustamante J, Folli F, et al. High energy density (HED) biaxially-oriented poly-propylene (BOPP) capacitors for pulse power applications. Magnetics, IEEE Transactions on. 2007;43(1):223-5.

[7] Chu B, Zhou X, Ren K, Neese B, Lin M, Wang Q, et al. A dielectric polymer with high electric energy density and fast discharge speed. Science. 2006;313(5785):334-6.

[8] Zhu L, Wang Q. Novel Ferroelectric Polymers for High Energy Density and Low Loss Dielectrics. Macromolecules. 2012;45(7):2937-54.

[9] Chung TM. Functionalization of Polypropylene with High Dielectric Properties: Applications in Electric Energy Storage. Green and Sustainable Chemistry. 2012;2:29.

[10] Ho J, Ramprasad R, Boggs S. Effect of Alteration of Antioxidant by UV Treatment on the Dielectric Strength of BOPP Capacitor Film. Dielectrics and Electrical Insulation, IEEE Transactions on. 2007;14(5):1295-301.

[11] Rabuffi M, Picci G. Status quo and future prospects for metallized polypropylene energy storage capacitors. Ieee Transactions on Plasma Science. 2002;30(5):1939-42.

[12] Claude J, Lu Y, Li K, Wang Q. Electrical storage in poly (vinylidene fluoride) based ferroelectric polymers: correlating polymer structure to electrical breakdown strength. Chem Mat. 2008;20(6):2078-80.

[13] Guan F, Pan J, Wang J, Wang Q, Zhu L. Crystal orientation effect on electric energy storage in poly (vinylidene fluoride-co-hexafluoropropylene) copolymers. Macromolecules. 2009;43(1):384-92.

[14] Zhang Z, Chung TM. The structure-property relationship of poly (vinylidene difluoride)-based polymers with energy storage and loss under applied electric fields. Macromolecules. 2007;40(26):9391-7.

[15] Zhang Z, Meng Q, Chung T. Energy storage study of ferroelectric poly (vinylidene fluoride-trifluoroethylene-chlorotrifluoroethylene) terpolymers. Polymer. 2009;50(2):707-15.

[16] Van Vechten JA. Quantum dielectric theory of electronegativity in covalent systems. I. Electronic dielectric constant. Physical review. 1969;182(3):891.

[17] Ziman JM. Principles of the Theory of Solids: Cambridge university press; 1972.

[18] Kittel C. Introduction to Solid State Physics. New York: Wiley, John; 2005.

[19] Chiang C, Popielarz R. Polymer composites with high dielectric constant. Ferroelectrics. 2002;275(1):1-9.

[20] Devaraju NG, Kim ES, Lee BI. The synthesis and dielectric study of BaTiO< sub> 3</sub>/polyimide nanocomposite films. Microelectronic engineering. 2005;82(1):71-83.

[21] Rao Y, Ogitani S, Kohl P, Wong C. Novel polymer–ceramic nanocomposite based on high dielectric constant epoxy formula for embedded capacitor application. Journal of Applied Polymer Science. 2002;83(5):1084-90.

[22] Xie SH, Zhu BK, Wei XZ, Xu ZK, Xu YY. Polylmide/BaTiO3 composites with controllable dielectric properties. Composites Part a-Applied Science and Manufacturing. 2005;36(8):1152-7.

[23] Yu K, Wang H, Zhou YC, Bai YY, Niu YJ. Enhanced dielectric properties of BaTiO3/poly(vinylidene fluoride) nanocomposites for energy storage applications. Journal of applied physics. 2013;113(3).

[24] Amaral F, Rubinger CPL, Henry F, Costa LC, Valente MA, Barros-Timmons A. Dielectric properties of polystyrene-CCTO composite. Journal of Non-Crystalline Solids. 2008;354(47-51):5321-2.

[25] Arbatti M, Shan X, Cheng ZY. Ceramic–polymer composites with high dielectric constant. Advanced Materials. 2007;19(10):1369-72.

[26] Dang ZM, Zhou T, Yao SH, Yuan JK, Zha JW, Song HT, et al. Advanced calcium copper titanate/polyimide functional hybrid films with high dielectric permittivity. Advanced Materials. 2009;21(20):2077-82.

[27] Ehrhardt C, Fettkenhauer C, Glenneberg J, Munchgesang W, Leipner HS, Diestelhorst M, et al. A solution-based approach to composite dielectric films of surface functionalized CaCu3Ti4O12 and P(VDF-HFP). J Mater Chem A. 2014;2(7):2266-74.

[28] Shri Prakash B, Varma K. Dielectric behavior of CCTO/epoxy and Al-CCTO/epoxy composites. composites Science and Technology. 2007;67(11):2363-8.

[29] Thomas P, Satapathy S, Dwarakanath K, Varma K. Dielectric properties of poly (vinylidene fluoride)/CaCu 3 Ti 4 O 12 nanocrystal composite thick films. eXPRESS Polymer Letters. 2010;4(10).

[30] Thomas P, Varughese KT, Dwarakanath K, Varma KBR. Dielectric properties of Poly(vinylidene fluoride)/CaCu3Ti4O12 composites. composites Science and Technology. 2010;70(3):539-45.

[31] Wang F, Zhou D, Hu Y. Preparation and dielectric properties of CaCu3Ti4O12–polyethersulfone composites. physica status solidi (a). 2009;206(11):2632-6.

[32] Yang C, Song HS, Liu DB. Effect of coupling agents on the dielectric properties of CaCu3Ti4O12/PVDF composites. Compos Pt B-Eng. 2013;50:180-6.

[33] Yang W, Yu S, Sun R, Du R. Nano-and microsize effect of CCTO fillers on the dielectric behavior of CCTO/PVDF composites. Acta Materialia. 2011;59(14):5593-602.

[34] Yang Y, Zhu BP, Lu ZH, Wang ZY, Fei CL, Yin D, et al. Polyimide/nanosized CaCu3Ti4O12 functional hybrid films with high dielectric permittivity. Applied Physics Letters. 2013;102(4).

[35] Zhang L, Shan X, Wu P, Cheng Z-Y. Dielectric characteristics of CaCu3Ti4O12/P (VDF-TrFE) nanocomposites. Applied Physics A. 2012;107(3):597-602.

[36] Dang Z-M, Yuan J-K, Zha J-W, Zhou T, Li S-T, Hu G-H. Fundamentals, processes and applications of high-permittivity polymer–matrix composites. Progress in Materials Science. 2012;57(4):660-723.

[37] Nelson JK. Dielectric polymer nanocomposites: Springer; 2010.

[38] Tanaka T. Dielectric nanocomposites with insulating properties. Dielectrics and Electrical Insulation, IEEE Transactions on. 2005;12(5):914-28.

[39] Wang Q, Zhu L. Polymer nanocomposites for electrical energy storage. Journal of Polymer Science Part B: Polymer Physics. 2011;49(20):1421-9.

[40] Bornand V, Vacher C, Collet A, Papet P. Interest of binary PMMA/P(VDF-TrFE) blend thin films. Materials Chemistry and Physics. 2009;117(1):169-72.

[41] Chu B, Neese B, Lin M, Lu S-g, Zhang Q. Enhancement of dielectric energy density in the poly (vinylidene fluoride)-based terpolymer/copolymer blends. Applied Physics Letters. 2008;93(15):152903--3.

[42] Chwang CP, Liu CD, Huang SW, Chao DY, Lee SN. Synthesis and characterization of high dielectric constant polyaniline/polyurethane blends. Synthetic Metals. 2004;142(1-3):275-81.

[43] Li R, Xiong C, Kuang D, Dong L, Lei Y, Yao J, et al. Polyamide 11/poly (vinylidene fluoride) blends as novel flexible materials for capacitors. Macromolecular rapid communications. 2008;29(17):1449-54.

[44] Meng Q, Li W, Zheng Y, Zhang Z. Effect of poly (methyl methacrylate) addition on the dielectric and energy storage properties of poly (vinylidene fluoride). Journal of Applied Polymer Science. 2010;116(5):2674-84.

[45] Rahimabady M, Yao K, Arabnejad S, Lu L, Shim VP, Chet DCW. Intermolecular interactions and high dielectric energy storage density in poly (vinylidene fluoride-hexafluoropropylene)/poly (vinylidene fluoride) blend thin films. Applied Physics Letters. 2012;100(25):252907.

[46] Wu S, Lin M, Lu S, Zhu L, Zhang Q. Polar-fluoropolymer blends with tailored nanostructures for high energy density low loss capacitor applications. Applied Physics Letters. 2011;99(13):132901.

[47] Zhang S, Neese B, Ren K, Chu B, Zhang Q. Microstructure and electromechanical responses in semicrystalline ferroelectric relaxor polymer blends. Journal of applied physics. 2006;100(4):044113.

[48] Huang C, Zhang Q. Enhanced Dielectric and Electromechanical Responses in High Dielectric Constant All-Polymer Percolative Composites. Advanced Functional Materials. 2004;14(5):501-6.

[49] Huang C, Zhang Q, Su J. High-dielectric-constant all-polymer percolative composites. Applied Physics Letters. 2003;82(20):3502-4.

[50] Hardy CG, Islam M, Gonzalez-Delozier D, Ploehn HJ, Tang C. Oligoaniline-Containing Supramolecular Block Copolymer Nanodielectric Materials. Macromolecular rapid communications. 2012;33(9):791-7.

[51] Hardy CG, Islam MS, Gonzalez-Delozier D, Morgan JE, Cash B, Benicewicz BC, et al. Converting an Electrical Insulator into a Dielectric Capacitor: End-Capping Polystyrene with Oligoaniline. Chem Mat. 2013;25(5):799-807.

[52] McCullough LA, Dufour B, Matyjaszewski K. Polyaniline and polypyrrole templated on self-assembled acidic block copolymers. Macromolecules. 2009;42(21):8129-37.

[53] McCullough LA, Dufour B, Tang C, Zhang R, Kowalewski T, Matyjaszewski K. Templating conducting polymers via self-assembly of block copolymers and supramolecular recognition. Macromolecules. 2007;40(22):7745-7.

[54] Qiao Y, Islam MS, Han K, Leonhardt E, Zhang J, Wang Q, et al. Nanomaterials: Polymers Containing Highly Polarizable Conjugated Side Chains as High-Performance All-Organic Nanodielectric Materials (Adv. Funct. Mater. 45/2013). Advanced Functional Materials. 2013;23(45):5570-.

[55] Patterson A. The Scherrer formula for X-ray particle size determination. Physical review. 1939;56(10):978.

[56] Scherrer á, Gottingen N. Elements of X-ray diffraction. Addision-Wesley; 1918.

[57] Bolotnikov AV, Muzykov PG, Grekov AE, Sudarshan TS. Improvement of 4H-SiC power p-i-n diode switching performance through local lifetime control using boron diffusion. Ieee Transactions on Electron Devices. 2007;54(6):1540-4.

[58] Bolotnikov AV, Muzykov PG, Sudarshan TS. Investigation of two-branch boron diffusion from vapor phase in n-type 4H-SiC. Applied Physics Letters. 2008;93(5).

[59] Muzykov PG, Bolotnikov AV, Sudarshan TS. Study of leakage current and breakdown issues in 4H-SiC unterminated Schottky diodes. Solid-State Electronics. 2009;53(1):14-7.

[60] Adams TB, Sinclair DC, West AR. Giant barrier layer capacitance effects in CaCu 3 Ti 4 O 12 ceramics. Advanced Materials. 2002;14(18):1321-3.

[61] Homes C, Vogt T, Shapiro S, Wakimoto S, Ramirez A. Optical response of high-dielectric-constant perovskite-related oxide. Science. 2001;293(5530):673-6.

[62] Ramirez A, Subramanian M, Gardel M, Blumberg G, Li D, Vogt T, et al. Giant dielectric constant response in a copper-titanate. Solid State Communications. 2000;115(5):217-20.

[63] Sinclair DC, Adams TB, Morrison FD, West AR. CaCu 3 Ti 4 O 12: one-step internal barrier layer capacitor. Applied Physics Letters. 2002;80(12):2153-5.

[64] Subramanian M, Li D, Duan N, Reisner B, Sleight A. High dielectric constant in ACu3Ti4O12 and ACu3Ti3FeO12 phases. Journal of Solid State Chemistry. 2000;151(2):323-5.

[65] Onodera A, Takesada M, Kawatani K, Hiramatsu S. Dielectric properties and phase transition in CaCu3Ti4O12 at high temperatures. Japanese Journal of Applied Physics. 2008;47(9S):7753.

[66] Lunkenheimer P, Krohns S, Riegg S, Ebbinghaus S, Reller A, Loidl A. Colossal dielectric constants in transition-metal oxides. The European Physical Journal Special Topics. 2009;180(1):61-89.

[67] Ramirez MA, Simões AZ, Felix AA, Tararam R, Longo E, Varela JA. Electric and dielectric behavior of CaCu3Ti4O12-based thin films obtained by soft chemical method. Journal of Alloys and Compounds. 2011;509(41):9930-3.

[68] Eršte A, Kužnik B, Malič B, Kosec M, Bobnar V. Dielectric Properties of CaCu3Ti4O12 Ceramic Thin Films. Ferroelectrics. 2011;419(1):14-9.

[69] Brize V, Gruener G, Wolfman J, Fatyeyeva K, Tabellout M, Gervais M, et al. Grain size effects on the dielectric constant of CaCu3Ti4O12 ceramics. Mater Sci Eng B-Solid State Mater Adv Technol. 2006;129(1-3):135-8.

[70] Jesurani S, Kanagesan S, Velmurugan R, Thirupathi C, Sivakumar M, Kalaivani T. Nanoparticles of the giant dielectric material, calcium copper titanate from a sol-gel technique. Mater Lett. 2011;65(21-22):3305-8.

[71] Jha P, Arora P, Ganguli AK. Polymeric citrate precursor route to the synthesis of the high dielectric constant oxide, CaCu3Ti4O12. Mater Lett. 2003;57(16-17):2443-6.

[72] Jin SH, Xia HP, Zhang YP, Guo JP, Xu J. Synthesis of CaCu3Ti4O12 ceramic via a sol-gel method. Mater Lett. 2007;61(6):1404-7.

[73] Li YY, Liang PF, Chao XL, Yang ZP. Preparation of CaCu3Ti4O12 ceramics with low dielectric loss and giant dielectric constant by the sol-gel technique. Ceram Int. 2013;39(7):7879-89.

[74] Liu J, Smith RW, Mei W-N. Synthesis of the Giant Dielectric Constant Material CaCu3Ti4O12 by Wet-Chemistry Methods†. Chem Mat. 2007;19(24):6020-4.

[75] Liu JJ, Sui YC, Duan CG, Mei WN, Smith RW, Hardy JR. CaCu3Ti4O12: Low-temperature synthesis by pyrolysis of an organic solution. Chem Mat. 2006;18(16):3878-82.

[76] Liu L, Fan H, Fang P, Chen X. Sol-gel derived CaCu3Ti4O12 ceramics: Synthesis, characterization and electrical properties. Materials Research Bulletin. 2008;43(7):1800-7.

[77] Marchin L, Guillemet-Fritsch S, Durand B, Levchenko AA, Navrotsky A, Lebey T. Grain Growth-Controlled Giant Permittivity in Soft Chemistry CaCu3Ti4O12 Ceramics. Journal of the American Ceramic Society. 2008;91(2):485-9.

[78] Masingboon C, Thongbai P, Maensiri S, Yamwong T, Seraphin S. Synthesis and giant dielectric behavior of CaCu< sub> 3</sub> Ti< sub> 4</sub> O< sub> 12</sub> ceramics prepared by polymerized complex method. Materials Chemistry and Physics. 2008;109(2):262-70.

[79] Parra R, Savu R, Ramajo LA, Ponce MA, Varela JA, Castro MS, et al. Sol-gel synthesis of mesoporous CaCu3Ti4O12 thin films and their gas sensing response. Journal of Solid State Chemistry. 2010;183(6):1209-14.

[80] Sun DL, Wu AY, Yin ST. Structure, properties, and impedance spectroscopy of CaCu3Ti4O12 ceramics prepared by sol–gel process. Journal of the American Ceramic Society. 2008;91(1):169-73.

[81] Thomas P, Dwarakanath K, Varma K, Kutty T. Synthesis of nanoparticles of the giant dielectric material, CaCu3Ti4O12 from a precursor route. Journal of Thermal Analysis and Calorimetry. 2009;95(1):267-72.

[82] Vangchangyia S, Swatsitang E, Thongbai P, Pinitsoontorn S, Yamwong T, Maensiri S, et al. Very Low Loss Tangent and High Dielectric Permittivity in Pure-CaCu3Ti4O12 Ceramics Prepared by a Modified Sol-Gel Process. Journal of the American Ceramic Society. 2012;95(5):1497-500.

[83] Yuan WX. Effect of the Addition of Polyvinyl Alcohol on Electric and Dielectric Properties of Giant Dielectric Constant Material CaCu3Ti4O12. Journal of the American Ceramic Society. 2010;93(10):3020-2.

[84] Yuan WX, Hark SK, Mei WN. Investigation of Triple Extrinsic Origins of Colossal Dielectric Constant in CaCu3Ti4O12 Ceramics. Journal of the Electrochemical Society. 2010;157(5):G117-G20.

[85] Zhu B, Wang Z, Zhang Y, Yu Z, Shi J, Xiong R. Low temperature fabrication of the giant dielectric material CaCu< sub> 3</sub> Ti< sub> 4</sub> O< sub> 12</sub> by oxalate coprecipitation m ethod. Materials Chemistry and Physics. 2009;113(2):746-8.

[86] Nan C-W, Shen Y, Ma J. Physical properties of composites near percolation. Annual Review of Materials Research. 2010;40:131-51.

[87] Calame J. Finite difference simulations of permittivity and electric field statistics in ceramic-polymer composites for capacitor applications. Journal of applied physics. 2006;99(8):084101.

[88] Guo M, Hayakawa T, Kakimoto M, Goodson T. Organic Macromolecular High Dielectric Constant Materials: Synthesis, Characterization, and Applications. J Phys Chem B. 2011;115(46):13419-32.

[89] Huang C, Zhang QM. Enhanced dielectric and electromechanical responses in high dielectric constant all-polymer percolative composites. Advanced Functional Materials. 2004;14(5):501-6.

[90] Huang C, Zhang QM. Fully functionalized high-dielectric-constant nanophase polymers with high electromechanical response. Advanced Materials. 2005;17(9):1153-+.

[91] Huang C, Zhang QM, deBotton G, Bhattacharya K. All-organic dielectric-percolative three-component composite materials with high electromechanical response. Applied Physics Letters. 2004;84(22):4391-3.

[92] Huang C, Zhang QM, Su J. High-dielectric-constant all-polymer percolative composites. Applied Physics Letters. 2003;82(20):3502-4.

[93] Molberg M, Crespy D, Rupper P, Nueesch F, Manson J-AE, Loewe C, et al. High Breakdown Field Dielectric Elastomer Actuators Using Encapsulated Polyaniline as High Dielectric Constant Filler. Advanced Functional Materials. 2010;20(19):3280-91.

[94] Zhang QM, Li HF, Poh M, Xia F, Cheng ZY, Xu HS, et al. An all-organic composite actuator material with a high dielectric constant. Nature. 2002;419(6904):284-7.

[95] Hardy CG. Functional Block Copolymers For Applications In Advanced Materials, Energy Storage, and Lithography. 2013.

[96] Chao DM, Jia XT, Liu HT, He LB, Cui LL, Wang C, et al. Novel Electroactive Poly(arylene ether sulfone) Copolymers Containing Pendant Oligoaniline Groups: Synthesis and Properties. J Polym Sci Pol Chem. 2011;49(7):1605-14.

[97] Cui LL, Chao DM, Lu XF, Zhang JF, Mao H, Li YX, et al. Synthesis and properties of an electroactive alternating multi-block copolymer of poly(ethylene oxide) and oligo-aniline with high dielectric constant. Polymer International. 2010;59(7):975-9.

[98] Liang SW, Claude J, Xu K, Wang Q. Synthesis of dumbbell-shaped triblock structures containing ferroelectric polymers and oligoanilines with high dielectric constants. Macromolecules. 2008;41(17):6265-8.

[99] Stoyanov H, Kollosche M, McCarthy DN, Kofod G. Molecular composites with enhanced energy density for electroactive polymers. Journal of Materials Chemistry. 2010;20(35):7558-64.

[100] Yang G, Hou WH, Feng XM, Jiang XF, Guo J. Electronic structure of oligoaniline doped by inorganic and organic acids. Int J Quantum Chem. 2008;108(6):1155-63.

[101] Wang J-W, Wang Y, Wang F, Li S-Q, Xiao J, Shen Q-D. A large enhancement in dielectric properties of poly (vinylidene fluoride) based all-organic nanocomposite. Polymer. 2009;50(2):679-84.

[102] Annunziata L, Monasse B, Rizzo P, Guerra G, Duc M, Carpentier JF. On the crystallization behavior of syndiotactic-b-atactic polystyrene stereodiblock copolymers, atactic/syndiotactic polystyrene blends, and aPS/sPS blends modified with sPS-b-aPS. Materials Chemistry and Physics. 2013;141(2-3):891-902.

[103] Guerra G, Vitagliano VM, De Rosa C, Petraccone V, Corradini P. Polymorphism in melt crystallized syndiotactic polystyrene samples. Macromolecules. 1990;23(5):1539-44.

[104] Hodge K, Prodpran T, Shenogina N, Nazarenko S. Solid-state structure of thermally crystallized syndiotactic polystyrene. Journal of Applied Polymer Science. 2002;83(12):2705-15.

[105] Kellar EJ, Galiotis C, Andrews EH. Raman vibrational studies of syndiotactic polystyrene. 1. Assignments in a conformational/crystallinity sensitive spectral region. Macromolecules. 1996;29(10):3515-20.

[106] Sun YS, Woo EM, Wu MC, Ho R-M. Polymorphism and phase transitions upon annealing in solvent-cast vs quenched syndiotactic polystyrene and its blends with atactic polystyrene. Macromolecules. 2003;36(22):8415-25.

[107] Li JJ, Khanchaitit P, Han K, Wang Q. New Route Toward High-Energy-Density Nanocomposites Based on Chain-End Functionalized Ferroelectric Polymers. Chem Mat. 2010;22(18):5350-7.

[108] Zhu L, Calhoun BH, Ge Q, Quirk RP, Cheng SZD, Thomas EL, et al. Initial-Stage Growth Controlled Crystal Orientations in Nanoconfined Lamellae of a Self-Assembled Crystalline−Amorphous Diblock Copolymer. Macromolecules. 2001;34(5):1244-51.

[109] Faria LO, Moreira RL. Dielectric behavior of P(VDF-TrFE)/PMMA blends. J Polym Sci Pt B-Polym Phys. 1999;37(21):2996-3002.

[110] Gregorio R, Malmonge LF, Ferreira GFL, dos Santos WN, Mattoso LHC. Dielectric behavior of PVDF/POMA blends that have a low doped POMA content. Journal of Applied Polymer Science. 2003;87(5):752-8.

[111] Paniagua SA, Kim Y, Henry K, Kumar R, Perry JW, Marder SR. Surface-Initiated Polymerization from Barium Titanate Nanoparticles for Hybrid Dielectric Capacitors. ACS applied materials & interfaces. 2014;6(5):3477-82.

[112] Yang K, Huang X, Huang Y, Xie L, Jiang P. Fluoro-Polymer@ BaTiO3 Hybrid Nanoparticles Prepared via RAFT Polymerization: Toward Ferroelectric Polymer Nanocomposites with High Dielectric Constant and Low Dielectric Loss for Energy Storage Application. Chem Mat. 2013;25(11):2327-38.

[113] Yang K, Huang X, Xie L, Wu C, Jiang P, Tanaka T. Core–Shell Structured Polystyrene/BaTiO3 Hybrid Nanodielectrics Prepared by In Situ RAFT Polymerization: A Route to High Dielectric Constant and Low Loss Materials with Weak Frequency Dependence. Macromolecular rapid communications. 2012;33(22):1921-6.

[114] Zhu XH, Zhu JM, Zhou SH, Liu ZG, Ming NB, Hesse D. BaTiO3 nanocrystals: Hydrothermal synthesis and structural characterization. J Cryst Growth. 2005;283(3-4):553-62.

[115] Qiao YL, Islam MS, Han K, Leonhardt E, Zhang JY, Wang Q, et al. Polymers Containing Highly Polarizable Conjugated Side Chains as High-Performance All-Organic Nanodielectric Materials. Adv Funct Mater. 2013;23(45):5638-46.

[116] Zhu L, Calhoun BH, Ge Q, Quirk RP, Cheng SZD, Thomas EL, et al. Initial-stage growth controlled crystal orientations in nanoconfined lamellae of a self-assembled crystalline-amorphous diblock copolymer. Macromolecules. 2001;34(5):1244-51.

[117] Dang ZM, Lin YH, Nan CW. Novel ferroelectric polymer composites with high dielectric constants. Adv Mater. 2003;15(19):1625-9.

[118] Li JJ, Seok SI, Chu BJ, Dogan F, Zhang QM, Wang Q. Nanocomposites of Ferroelectric Polymers with TiO2 Nanoparticles Exhibiting Significantly Enhanced Electrical Energy Density. Adv Mater. 2009;21(2):217-21.

[119] Kim P, Jones SC, Hotchkiss PJ, Haddock JN, Kippelen B, Marder SR, et al. Phosphonic Acid-Modified Barium Titanate Polymer Nanocomposites with High Permittivity and Dielectric Strength. Adv Mater. 2007;19(7):1001-5.

[120] Kim P, Doss NM, Tillotson JP, Hotchkiss PJ, Pan M-J, Marder SR, et al. High Energy Density Nanocomposites Based on Surface-Modified BaTiO3 and a Ferroelectric Polymer. ACS Nano. 2009;3(9):2581-92.

[121] Paniagua SA, Kim Y, Henry K, Kumar R, Perry JW, Marder SR. Surface-Initiated Polymerization from Barium Titanate Nanoparticles for Hybrid Dielectric Capacitors. ACS Appl Mater Interfaces. 2014:DOI: 10.1021/am4056276.

[122] Yang K, Huang X, Huang Y, Xie L, Jiang P. Fluoro-Polymer@BaTiO3 Hybrid Nanoparticles Prepared via RAFT Polymerization: Toward Ferroelectric Polymer Nanocomposites with High Dielectric Constant and Low Dielectric Loss for Energy Storage Application. Chem Mater. 2013;25(11):2327-38.

[123] Li JY, Zhang L, Ducharme S. Electric energy density of dielectric nanocomposites. Applied Physics Letters. 2007;90(13).

[124] Looyenga H. Dielectric constants of heterogeneous mixtures. Physica. 1965;31(3):401-6.

[125] Sihvola A. Mixing rules with complex dielectric coefficients. Subsurface Sensing Technologies and Applications. 2000;1(4):393-415.

[126] Vo HT, Shi FG. Towards model-based engineering of optoelectronic packaging materials: Dielectric constant modeling. Microelectronics journal. 2002;33(5):409-15.

[127] Wang ZP, Nelson JK, Miao JJ, Linhardt RJ, Schadler LS, Hillborg H, et al. Effect of High Aspect Ratio Filler on Dielectric Properties of Polymer Composites: A Study on Barium Titanate Fibers and Graphene Platelets. IEEE Trns Dielectr Electr Insul. 2012;19(3):960-7.

[128] Bikky R, Badi N, Bensaoula A. Effective Medium Theory of Nanodielectrics for Embedded Energy Storage Capacitors.

[129] Ekanath DM, Badi N, Bensaoula A. Modeling and Simulation of Artificial Core-Shell Based Nanodielectrics for Electrostatic Capacitors Applications.

[130] Brosseau C, Beroual A. Computational electromagnetics and the rational design of new dielectric heterostructures. Progress in Materials Science. 2003;48(5):373-456.

[131] Dinulović M, Rašuo B. Dielectric modeling of multiphase composites. Composite Structures. 2011;93(12):3209-15.

[132] Jacobsen KW, Stoltze P, Norskov JK. A semi-empirical effective medium theory for metals and alloys. Surf Sci. 1996;366(2):394-402.

[133] Krakovský I, Myroshnychenko V. Modeling dielectric properties of composites by finite-element method. Journal of applied physics. 2002;92(11):6743-8.

[134] Rao Y, Qu J, Marinis T, Wong C. A precise numerical prediction of effective dielectric constant for polymer-ceramic composite based on effective-medium theory. Components and Packaging Technologies, IEEE Transactions on. 2000;23(4):680-3.

[135] Stafford O, Hinderliter B, Croll S. Electrochemical impedance spectroscopy response of water uptake in organic coatings by finite element methods. Electrochimica Acta. 2006;52(3):1339-48.

[136] Tuncer E, Serdyuk YV, Gubanski SM. Dielectric mixtures--electrical properties and modeling. arXiv preprint cond-mat/0111254. 2001.

[137] Wang Z, Keith Nelson J, Hillborg H, Zhao S, Schadler LS. Dielectric constant and breakdown strength of polymer composites with high aspect ratio fillers studied by finite element models. composites Science and Technology. 2013;76:29-36.

[138] Huray PG. Maxwell's equations: John Wiley & Sons; 2011.

APPENDIX A

COPYRIGHT RELEASES

JOHN WILEY AND SONS LICENSE TERMS AND CONDITIONS

Jul 01, 2014

This is a License Agreement between Md S Islam ("You") and John Wiley and Sons ("John Wiley and Sons") provided by Copyright Clearance Center ("CCC"). The license consists of your order details, the terms and conditions provided by John Wiley and Sons, and the payment terms and conditions.

All payments must be made in full to CCC. For payment instructions, please see information listed at the bottom of this form.

License Number	3420011504980
License date	Jul 01, 2014
Licensed content publisher	John Wiley and Sons
Licensed content Publication	Macromolecular Rapid Communications
Licensed content title	Oligoaniline-Containing Supramolecular Block Copolymer Nanodielectric Materials
Licensed copyright line	Copyright © 2012 WILEY-VCH Verlag GmbH & Co. KGaA, Weinheim
Licensed content author	Christopher G. Hardy,Md. Sayful Islam,Dioni Gonzalez- Delozier,Harry J. Ploehn,Chuanbing Tang
Licensed content date	Feb 14, 2012
Start page	791
End page	797
Type of use	Dissertation/Thesis
Requestor type	Author of this Wiley article
Format	Print and electronic
Portion	Figure/table
Number of figures/tables	2
Original Wiley figure/table number(s)	Table 1, Scheme 1
Will you be translating?	No
Title of your thesis/ dissertation	POLYMER NANO-DIELECTRICS FOR HIGH DENSITY ENERGY STORAGE
Expected completion date	Aug 2014
Expected size (number of pages)	162
Total	0.00 USD
Terms and Conditions	

Figure A.1. Copyright release for Chapter 4, Section 4.2

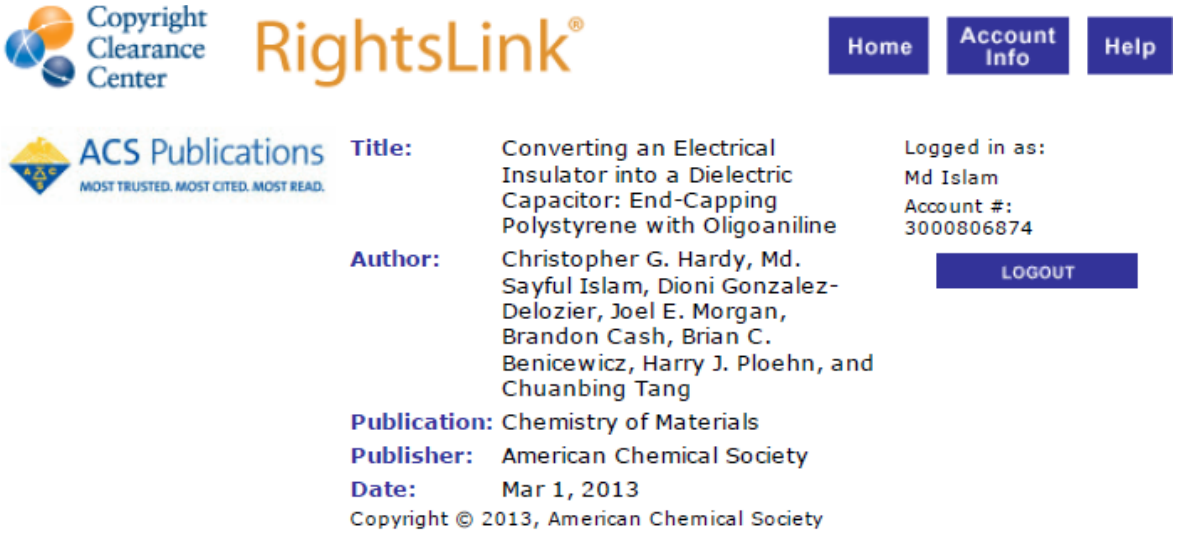

Copyright Clearance Center RightsLink®

Home | Account Info | Help

ACS Publications
MOST TRUSTED. MOST CITED. MOST READ.

Title: Converting an Electrical Insulator into a Dielectric Capacitor: End-Capping Polystyrene with Oligoaniline

Author: Christopher G. Hardy, Md. Sayful Islam, Dioni Gonzalez-Delozier, Joel E. Morgan, Brandon Cash, Brian C. Benicewicz, Harry J. Ploehn, and Chuanbing Tang

Publication: Chemistry of Materials

Publisher: American Chemical Society

Date: Mar 1, 2013

Copyright © 2013, American Chemical Society

Logged in as:
Md Islam
Account #:
3000806874

LOGOUT

PERMISSION/LICENSE IS GRANTED FOR YOUR ORDER AT NO CHARGE

This type of permission/license, instead of the standard Terms & Conditions, is sent to you because no fee is being charged for your order. Please note the following:

- Permission is granted for your request in both print and electronic formats, and translations.
- If figures and/or tables were requested, they may be adapted or used in part.
- Please print this page for your records and send a copy of it to your publisher/graduate school.
- Appropriate credit for the requested material should be given as follows: "Reprinted (adapted) with permission from (COMPLETE REFERENCE CITATION). Copyright (YEAR) American Chemical Society." Insert appropriate information in place of the capitalized words.
- One-time permission is granted only for the use specified in your request. No additional uses are granted (such as derivative works or other editions). For any other uses, please submit a new request.

Figure A.2. Copyright release for Chapter 4, Section 4.3

JOHN WILEY AND SONS LICENSE TERMS AND CONDITIONS

Jul 01, 2014

This is a License Agreement between Md S Islam ("You") and John Wiley and Sons ("John Wiley and Sons") provided by Copyright Clearance Center ("CCC"). The license consists of your order details, the terms and conditions provided by John Wiley and Sons, and the payment terms and conditions.

All payments must be made in full to CCC. For payment instructions, please see information listed at the bottom of this form.

License Number	3420020896611
License date	Jul 01, 2014
Licensed content publisher	John Wiley and Sons
Licensed content Publication	Advanced Functional Materials
Licensed content title	Polymers Containing Highly Polarizable Conjugated Side Chains as High-Performance All-Organic Nanodielectric Materials
Licensed copyright line	Copyright © 2013 WILEY-VCH Verlag GmbH & Co. KGaA, Weinheim
Licensed content author	Yali Qiao,Mohammed Sayful Islam,Kuo Han,Eric Leonhardt,Jiuyang Zhang,Qing Wang,Harry J. Ploehn,Chuanbing Tang
Licensed content date	Jun 13, 2013
Start page	5638
End page	5646
Type of use	Dissertation/Thesis
Requestor type	Author of this Wiley article
Format	Print and electronic
Portion	Figure/table
Number of figures/tables	9
Original Wiley figure/table number(s)	Scheme 1-2, Table 1, Figure 3,Figure 7
Will you be translating?	No
Title of your thesis / dissertation	POLYMER NANO-DIELECTRICS FOR HIGH DENSITY ENERGY STORAGE
Expected completion date	Aug 2014
Expected size (number of pages)	162
Total	0.00 USD
Terms and Conditions	

Figure A.3. Copyright release for Chapter 4, Section 4.4